# URJ-IIT

ILLINOIS INSTITUTE OF TECHNOLOGY
UNDERGRADUATE RESEARCH JOURNAL

SPRING 2021 | VOLUME I

## Featuring PROJECT 1890

# MASTHEAD

VOL. 1 | 2021

# FOREWORD

Welcome to the 2020-2021 issue of the Undergraduate Research Journal at Illinois Tech. In this issue, our students give us a glimpse of the undergraduate-driven research done at our university, covering diverse disciplines including Biology, Computer Science, Engineering, Mathematics, Psychology, and Physics. The topics published here are very important and innovative, from Cancer and Diabetes detection and their causes to the development of a Mathematical method, Office Space building, and how luck and knowledge determine the outcome of scientific endeavor. Our students' research also touches on the issue of our time: COVID-19, its treatment, testing, and causes of the disease. This issue shows the intellect, passion, and grit of the authors, and shows what you, as an undergraduate student, can accomplish.

I am the faculty advisor of the Undergraduate Research Journal and I am amazed about the quality of the works found in this first issue. As an educator, I find inspiration in students' passion and their pursuit of knowledge. As a scientific researcher, I share with the authors of these manuscripts both a humble sense of wonder and pride in what they can accomplish through their dedication and hard work, the two key ingredients for success in any field. I am also impressed by the diligent work of the Editorial Board of the Undergraduate Research Journal. The Editorial Board is formed by some of the very best students in the university, who are not only academically skilled but have a deep sense of commitment to Science and to the service to their classmates.

This issue is dedicated to Project 1890, an initiative to rediscover the rich black history that has preceded our university and helped it advance through the years. The Undergraduate Research Journal hopes to honor the very grounds upon which the Mies campus was built, by learning and sharing the rich history of those who lived and studied here before us. The cover of the journal portrays Illinois Tech Alumni Gloria Karlmark, a member of the Little Rock Nine, who were involved in the first efforts to desegregate schools in the US among other notable alumni. The colors of the cover: reds and browns, are inspired by the Rainbow PUSH coalition logo, an organization involved in civil rights and in the leveling of the Economic and Educational playing fields in the country. I am glad to see that the Editorial Board and the student authors made a conscious effort to acknowledge the hard realities and history of our country. Our students show us that they can do transformative science, and at the same time look bravely at the challenges and problems of the present and the past, to give us a future.

**DR. OSCAR JUAREZ**

# IN THIS ISSUE


Feature

1 **PROJECT 1890**
Enya Mulroy, Alisha Khan, Lisa Montgomery

PSYCHOLOGY

18 **REPLICATION: KNOWLEDGE AND LUCK**
Aminah Ahmed

BIOLOGY

24 **DETECTION OF BAXΔ2 POSITIVE MACROPHAGE IN BREAST TISSUES**
Anam Adil

BIOLOGY

27 **APPLICATION OF MOLECULAR IMPRINTED POLYMER TECHNOLOGY TO DETECT THE SARS-COV-2 VIRUS THROUGH THE DEVELOPMENT OF A NOVEL BREATHALYZER-LIKE DEVICE**
Laasya Annepureddy

CHEMICAL ENGINEERING

34 **PREDICTIVE MODELING FOR EARLY HYPERGLYCEMIA DETECTION IN TYPE 2 DIABETES**
Pulkita Jain

CIVIL, ARCHITECTURAL, AND ENVIRONMENTAL ENGINEERING

40 **ASSESSING THE PERFORMANCE OF BUILDING MECHANICAL SYSTEMS IN AN OFFICE BUILDING**
Irfan Urwa

BIOMEDICAL ENGINEERING

42 **INTRAOPERATIVE ASSESSMENT OF SURGICAL MARGINS IN CANCER RESECTION SURGERY VIA THE SUB-DIFFUSE OPTICAL TOMOGRAPHY (S-DOT)**
Sophia Nelson

# IN THIS ISSUE


BIOMEDICAL ENGINEERING

47 **AN AGENT-DEPENDENT ENHANCED OPTICAL PROJECTION TOMOGRAPHY-GUIDED SYSTEM FOR LYMPH-NODE IMAGES RECONSTRUCTION TO OPTIMIZE CANCER DETECTION**

Hang Nguyen

APPLIED MATHEMATICS

49 **(QUASI-)MONTE CARLO IMPORTANCE SAMPLING WITH QMCPY**

Aleksei Sorokin

APPLIED MATHEMATICS

55 **DNPC: A DYNAMIC NODE-LEVEL POWER CAPPING LIBRARY FOR SCIENTIFIC APPLICATIONS**

Sahil Sharma

APPLIED MATHEMATICS

59 **SIMULATIONS OF EXTERNAL MULTI-PARTICLE DLA ON THE PLANE AND CONNECTIONS TO THE SUPER-COOLED STEFAN PROBLEM**

Alex Negron

APPLIED MATHEMATICS

65 **A GROBNER BASIS DATABASE**

Jelena Mojsilovic

BIOLOGY

68 **THE IMMUNE SYSTEM'S BATTLE AGAINST SARS-COV-2**

Caroline Mazur-Sarocka

Armour Mission and Main Building, Armour Institute of Technology, Chicago, Illinois, ca. 1900. Photographer unknown. Source: C.V. Smith photographs, Illinois Institute of Technology.

# Project 1890

When we go to class in different buildings on campus every day, we don't always think about what buildings were originally there, despite decades of history sitting right under the buildings we occupy every day. At URJ-IIT, we feel that is our responsibility to recognize the history of the land that our University currently sits on. That is why we started Project 1890: a collection of writing, images, and stories about the history of IIT. IIT undoubtedly occupies a unique part of history on the South Side—the South Side is the oldest part of the city, and in 1889 the southernmost limit of the city was 39th street.

The land that became our campus was a backdrop to many historical events in the late 19th and 20th centuries. It is first important to recognize the events that led to a high African-American population on the south side. The Chicago economy had been relying on European immigrants as a source of labor, however, after 1914 young men were not allowed to leave their European home countries because of the war. African Americans then filled that labor need in Chicago, largely because of advertising in the Southern United States that led them to migrate to the North: this was the First Great Migration (1910-1930). The Second World War created a Second Great Migration (1940-1970) that more people are familiar with.

Many groups of people have come in and out of Chicago as “temporary” laborers. So when Black Americans did not return to the South after the First World War, many Whites in Chicago were displeased, and blamed economic downturn on Black Americans which triggered the 1919 Race Riots.

## The Stroll and The Classic Era of Bronzeville

The Stroll was a jazz district right next to IIT that spanned from 31st to 35th street. Of particular note for IIT students is the Grand Theatre on 3110 South State Street. It opened in 1911 and became a home for Jazz and eventually motion pictures in the 1920s and 30s as those became more popular forms of entertainment. What is important for us now is that the Grand Theatre is on the exact spot where the Robert A. Pritzker Science Center is today. The Grand Theatre was bought by IIT and demolished to make room for the building.

During its peak, The Stroll was visited by several famous musicians including Jelly Roll Morton, Tony Jackson, Louis Armstrong, Joe “King” Oliver, Lillian Hardin, Bessie Smith, Ethel Waters, and Duke Ellington. In 1962, Duke Ellington returned to Chicago to perform at IIT in Hermann Hall.

The Vendome, The Mecca Flats, and The Grand Theatre were all torn down to make space for IIT to expand.


The Vendome Theatre at 3145 South State Street. Left image date unknown, Right image circa 1948-9. Images: cinematreasures.org

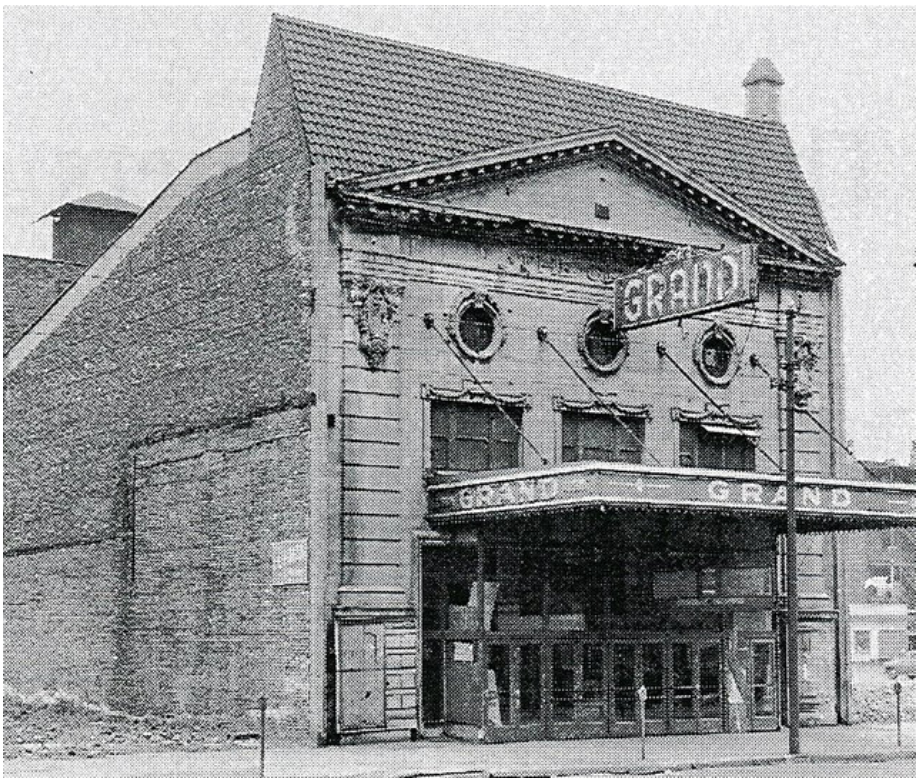


The Grand Theatre at 3110 South State Street. Image credit goes to cinema treasures.org.

IIT Buildings and Grounds. Photographed by Mildred Mead in 1962. University of Chicago Photographic Archive, [apf2-10020], Hanna Holborn Gray Special Collections Research Center, University of Chicago Library.


From 32nd and Wabash to Michigan Avenue, Illinois Institute of Technology dormitory. Photographed by Mildred Mead, 09/26/1951. University of Chicago Photographic Archive, [apf2-01576], Hanna Holborn Gray Special Collections Research Center, University of Chicago Library.

# Influential Alumni

**IIT is lucky enough to have so many influential alumni in the areas of science, technology, engineering, journalism, architecture, and even politics. However, we would like to highlight noteworthy African American alumni.**

## Gloria Ray Karlmark

Gloria Ray Karlmark received a Bachelor's degree in Chemistry and Mathematics from IIT in 1965. When she was 15 she was part of the "Little Rock 9", a group of students who were the first to integrate the all-white Central High School in Little Rock, Arkansas in 1959. She proceeded to have a very successful career as a patent attorney for technology companies in Sweden and The Netherlands, while also being the founder and editor-in-chief of the journal *Computers in Industry*.

Image Credit: Zbigniew Bzdak/Chicago Tribune

## Charles Warner Pierce

Born in 1876, Charles W. Pierce was the first African American to receive a degree in chemical engineering in the United States. He received his degree in 1901 and went on to teach at Tuskegee Normal College (Tuskegee University) and The State Agricultural and Mechanical College (North Carolina A&T State University), before returning to Chicago to teach physics at Wendell Phillips High School in 1921. In 1935 he moved to DuSable High School where he taught physics and science until he retired in 1941 before passing away in 1947.

Image credit: Illinois Institute of Technology

## Otis Frank Boykin

Image Credit: Unknown

Otis F. Boykin was a native of Dallas, Texas where he was born in 1920. Boykin went on to attend Fisk University to earn his Bachelor's degree in 1941. He then took a job at Majestic Radio & TV in Chicago, only to leave that job in 1944 to become a researcher engineer at PJ Nilsen Research Labs. He attended IIT from 1946-7 while working for Nilsen, but did not receive a formal degree here. Boykin had over 20 patents including electronic control devices that were used for the first pacemakers, guided missiles, as well as small component thick film resistors that were used for IBM computers. Boykin had offices for his own independent research company in the US and France, and worked there until his death in 1982.

## Neal Ferdinand Simeon

Born in Chicago on May 30, 1916, Neal F. Simeon was a prolific educator, athlete, and Navy veteran. He attended IIT where he competed in track and boxing, and graduated with his Bachelor's degree in Mechanical Engineering in 1938. He briefly worked in aviation and taught aviation mechanics at the Tuskegee Institute in Alabama. He joined the Navy in 1945 and was a seaman for two years, while also being a Golden Gloves boxer. In 1950, he received a Masters in Education from Northwestern University. He began teaching at Wendell Phillips Evening High School, and later became the Director of Vocational Education at Dunbar Vocational High School. He was asked by President John F. Kennedy in 1962 to represent the Unites States at the International Trade Fair in Lagos Nigeria. Simeon was dedicated to vocational training for young people in Chicago, and The Simeon Career Academy now bears his name. Unfortunately Mr. Simeon passed away at the age of 46 in 1963.

Image Credit: Simeon Career Academy

## Ida Platt

Image Credit: Unknown

Ida Platt, born in 1863, was the first African American woman to be licensed to practice law in Illinois, and only the third in the entire country. She graduated from the Chicago-Kent College of Law in 1894, where she was the first African American woman to graduate. She started her career working for Joseph Washington Errant, where she focused on probate and real estate law, where she was popular with foreign clients because she was fluent in English, German, and French. She eventually opened her own law office on Van Buren Street, and continued to practice law until marrying and moving to England in 1928. She passed away in 1939 at the age of 76.

# Robert Sengstacke Abbott

Robert S. Abbott was born on December 24, 1868 on St. Simons island in Georgia. The child of freed slaves, Abbott went on to study printmaking at the Hampton Institute (now Hampton University) in Virginia, and received a law degree from the Kent College of Law in 1898. Due to prejudice and harassment, he was unable not set up a law office, despite trying in Gary, Indiana, Topeka, Kansas, and Chicago. He then moved into the newspaper business and founded *The Chicago Defender* in 1905. It became the most widely circulated Black newspaper in the country and its popularity made Abbott one of the first African American self-made millionaires. Abbott also started the Bud Billiken Parade and Picnic in 1929 as  a way to celebrate African-American life and culture. It is now one of the largest parades in the country and occurs annually  on the second Saturday of August.

Image Credit: Unknown

# The Black Student Movement in the United States

The following is an essay written by Alisha Khan regarding the Black Student movement in America, and how that movement manifested at IIT.

The Black student movement took place in America during the 1960s and early 1970s. I will begin by discussing the causes which were a catalyst for this movement. The article “Black Students and the ‘Impossible Revolution’” was written by Dr. Vincent Harding and was published by Ebony Magazine in August 1969. Dr. Harding goes into detail about the mindsets in society. Before increased demands from Black students and the sense of Blackness were very visible in society, White people expected Black people who had the opportunity for education to see education as an escape from Blackness. They thought that being accepted and molded into white society was “freedom”. “As northern schools... opened their doors to more than the traditional token numbers of Black students... They expected from Black students hymns of praise and songs of hosanna for the opportunity to enter the ‘mainstream’ of American society” . Instead, the unexpected happened: Black students did not fulfill the expectations for white people. They did not mold into white society. “They were wrong, very wrong-partly because they did not understand the significance of our newest urge toward Blackness” . This shows the effect of Blackness on the mindset of people. There was an increased sense of pride of being Black and I believe that this powered the activist movement of Black Students and in extension, Black nationalism.

In this next section, I will discuss the essence of this movement and how this movement was implemented by students. The article “Black Students and their Changing Perspective” was written by James Turner and was published in Ebony Magazine in August 1969. Turner writes about how the “political socialization of Black students is undergoing a dramatic transformation” 3 Black students are determined to change the system. They plan on focusing on issues “including questions of campus and social inequities, relevant education for service to the Black community, and university expansion which takes the adjacent land and homes of neighboring Black families. For example, the University of Chicago... and the Illinois Institute of Technology has similar expansion plans into the surrounding Black community on the South Side of Chicago[4]”.

The article “Black Students and the ‘Impossible Revolution’” written by Dr. Vincent Harding talks about the demands made by Black students. One of the demands was that “the years of wasted Black talent, be overcome with a speed and a disrespect for ‘traditional [5]procedures’” . Another demand is for “a total

reassessment of the curriculum, especially those[6] studies dealing with man and society and the nature of the culture" . The article then talks about the foundations of America, "The 'Founding Fathers' must then be viewed also as the masters of our Black forefathers; the Constitution must be understood as condoning our slavery when it was[7] written" . The following section of the article named "The Black and Bright Star" discusses the sense of Blackness. An excerpt that I found very insightful and moving states, "Black students have learned that the eyes of Blackness are the eyes of the majority of the peoples of the earth. They are the eyes of the colonized, the eyes of the oppressed and the humiliated, the eyes of [8]those who search for a new coming of their deepest powers" . In the following section of the article titled "Black, N****, or Almost White?" pointed out an interesting contradiction: Even in Black schools, there were demands for Black studies and more Black faculty. The reason why demands were being made even at Black schools is because " the majority of Black schools had become frightening carbon copies of some of the worse curriculum practices of the 'great[9] universities' of the North" . This shows that there is a problem in education that must be fixed, and Black students plan to solve this through their revolution. This article ends with a quite impelling statement: "Perhaps there are no dreams yet dreamed, no plans yet planned, no possibilities yet defined which will bring us through the racial hell created by white America and its forebears. So Black students on the campuses take the only realistic step: they demand the[10] impossible" .

In September 1969, Part II of this article was released. It is titled "Black Students and the 'Impossible Revolution' Part II". Dr. Harding states the main components of the movement by Black students, "That movement of Black students has been a series of calls, cries and demands and actions. The call has been for the right to organize unashamedly as Blacks; the demand has been for the transformation of normal admissions procedures to allow the 'impossible' numbers of Black young people to enter the campus...At its heart, the challenge of Black students on campus is a challenge not only to the educational structures, but to the core of American society"[11].To make these changes students believe that whites are unable to make these "after so many years of discriminatory decision-making concerning Blacks"[12] this implies that Black people should be involved in decision making so these demands are enacted. This is a big change in society, "For white America-and, sadly, for most Blacks-this is surely the impossible thought, to believe that radical, life-affirming change in America may have to follow Black leadership, Black directions"[13]. I interpret this as a satirical statement as it shows that the old structures of whites ruling everything will end. In the following section, the article discusses the dangers that arise as a result of this movement. One danger is the contradictory feelings Black people may have towards America. Another is viewing education as "the true

pathway to liberation, to assume that its institutions, if radically transformed, will bring justice"[14]. Dr. Harding then states that integration may be the most immediate danger, "They will come from America's sudden love affair with 'integration'—defined nowadays as anything which prevents the building of Black solidarity and a new Black sense of direction"[15]. The article with a motivational statement supporting the movement by Black students "The only time we have is now. So now we must demand the impossible….Only then will our children-and our fathers-be free. Right on brothers. Right on"[16]. These sources from the Ebony magazine give a clear insight into what the Black student movement consists of. In the next section, I will discuss this movement concerning the Illinois Institute of Technology with sources from Tech News.

The earliest articles I found about the Black student association at Illinois Tech were published on May 10, 1968. One of them is titled "Black Student Group Expresses Grievances to IIT Administration". This article states that the list of grievances must be satisfied if "this university is not only to become a genuinely free intellectual community, but also to survive"[17]. The article goes on to talk about how "IIT cannot exist indefinitely as a white island surrounded by a hostile Black sea"[18]. Following this, there is a list of grievances made. I will put them in brief terms: Police harassment must end. There should be strict rules governing IIT police action and where the police can act. The disciplinary board meetings must be open hearings and transcripts should be available to the parties involved. Students have to be included on this board. All barricades and fences must be removed between IIT and the surrounding community. Distinctions regarding the use of campus facilities that are open to non-IIT students must end.

There should be a first come first serve basis of the facilities regardless of the socio-economic origins of the individuals and groups.

Rooms must be opened every day to cultural and civic groups in the surrounding neighborhood. There should be an accelerated recruitment program for high schools located in the neighborhood. This must begin immediately.

25% Black students.

In September 1968, a Black Studies Department will be established.

There will be a policy to recruit Black faculty members throughout the institution.

There will be a jazz concert on campus and it will be open to all students, faculty, and the surrounding neighborhood. It will also be free[19].

In the next column of the same issue of Tech News, the administration reaction is provided. It states that Dr. Rettaliata, the president of IIT, appointed a

community from the IIT administration to meet with the students that presented this petition. There is also a statement from Dr. Rettaliata: “IIT has never practiced racism and allows no racial restrictions in its employment, admissions, or housing policies...The university is willing to engage in constructive discussions but will not be responsive to ultimatums, threats, or intimidations”[20].

On the next page of the same issue, there is an article called “What Goal Does Black Student Action Seek”. It says that in the last few days, the student body has seen many efforts by Black students to improve their situation on campuses and in communities. These actions have been taking place all around the US as well as IIT. These efforts have shown. Non-Black students have participated in these events as well. The article then goes on to ask specific questions such as the following: “What will be the effect that some of these demands... have upon integration?”[21] “Will not some of these points and proposals produce a more segregated society? Or will they, in attempting to promote a segregated situation, really show the failing of such a social system and in turn produce a society which feels individually compelled to living inter-racially related lives”[22], “Specifically, will the demand for separate, all-Black housing actually help foster integration? Or will it propagate the already hates ‘equal but separate’ approach to equality?”[23], will the desire to teach Black culture as opposed to Black history, life, socio-economic situation promote understanding between the races or will it serve to build pride and will this pride separate the races? “If these actions turn to separating the races, will this separation solve the social problems that are challenging us today?”[24]. The author answers the last question by stating they disagree and believe that “it might guide all Americans into the path that has faced other racially-oriented societies, that is, the path of decline”[25]. The article is concluded by stating that the ideas the author has listed benefits all and does not serve to harm others. These ideas should be important to someone who wants to “better the lives of all persons who have suffered, in the pasts and present, under prejudice”[26].

Right below the previous article, there is another article titled, “ITSA President Comments on Black Student Petition”. It is stated in the article that there are serious questions concerning the University’s responsibility to the surrounding community”[27] and that the answers need to be found in discussions with all parties involved. These discussions haven’t taken place yet but it is hoped that they will soon. The article goes on to say that “any attempt to interfere with the operations of the university, therefore, cannot be tolerated”[28]. The article concludes by saying that everyone should work together to solve mutual problems and “not respond to divisive forces, whatever their source”[29].

On May 17, 1968, an article titled “Black Students, Concerned Whites, and Administrative Committee Begin Discussions of List of Grievances” was published. The IIT administration replies to the demands in the hope to start a discussion. Dr. Brophy states that “IIT is not a racist institution”[30]. This is about possible accusations regarding discrimination in “admissions, housing, or employment”[31]. However, members of the alliance countered by citing numerous instances of racist practices which have gone unnoticed and unpunished. Included wer instances such as police bullying, asking Black students for identification, and not white students, promoting a white employee rather than a Black employee who deserved the promotion due to qualifications. In response to this, the administration said that such practices are “absolutely contrary”[32] to IIT administrative policy. Dean Barnett promised the alliance that a statement regarding such practices being not allowed will be issued. He also asked that all racist activities be reported to him. Regarding the removal of physical barriers between IIT and the surrounding community, “administration officials refuse to ‘take the risk’ of removing the fences”[33]. The alliance replied to this by saying that “the fences is a powerful symbol indicating to community residents that they are not watned at IIT”[34]. There was no progressive discussion after this point. The groups met again that morning.

In the same issue of Tech News, the reaction of racist white students to the demands of Black students can be seen. This is in the Letters to the Editor-in-Chief section. A student named Andrew Gale wrote the following:

BLACK STUDIES DEPARTMENT

| Department | Course Number | Course Title |
|---|---|---|
| Language | 101 | Tarzan Talk |
| | 102 | Jane Talk |
| | 201 | Advanced Boy Talk |
| | 202 | Cheetah Talk |
| | 301 | Advanced Kreegah' Bundolo! |
| Afro-Culture | 101 | Basic Cannibalism |
| | 103 | Intermediate Cannibalism |
| | 313 | (Upon Request) Missionary Dissecting |
| | 401 | Elephant Ivory Stripping |
| Afro-History | 101 | The Modern Funky: As Performed In Ancient Watusi Culture |
| | 102 | Early Lip Plate Making |
| | 103 | Pre-Koogamoogah |
| | 104-B | (Special Students Only!) Koogamoogah |
| | 104-C | Return Of Koogamoogah |
| | 105 | Growth Of Reefers In Black Society |
| | 201 | Impact Of Black Cowboy On The Birth-Control Program Of The American Indian |
| Economics | 101 | Cadillac Buying |
| | 102 | Avoidance Of Cadillac Repossession |
| Looting Science | 101 | Principles Of Rapid Sniper Fire |
| | 102 | Black Sniperism In A White Society |
| | 201 | Advanced Fifth Floor Sniping |
| | 202-A | (Special) The Natural Look |
| | 203 | Basic Brick Throwing |
| | 204 | Store Entry |
| | 301 | Roach Breeding In Upper Class Ghettoes |
| | 302 | Depreciating A White Neighborhood |

There has been nothing written on this topic for 6 months until October 25, 1968. An article called “List of Resolutions Presents Demands of Black Students”. There was a second attempt of the Black Student Organization to submit a list of resolutions to IIT. It was submitted on October 14, 1968. The new list of resolutions was very similar to the list from May 1968. The article states that “Dr. James Brophy, academic vice president of IIT, to whom the list was presented, declined to comment on the matter until he could meet with the organization’s co-presidents”[35]. A meeting was held but “no significant agreement was reached between the two groups”[36]. The organization leaders wanted to evaluate “IIT’s past efforts to communicated with people of the Near South Side”[37]. There has been an agreement to “allow the use of IT facilities for the educational program proposed by the Black students”[38]. Later in the article, the Black student organization “accused IIT of trying to create its private white suburb within the middle of the urban Black community”’[39]. In the end, Brophy hoped to have more meetings with the organization. On the other hand, Thomas didn’t see many of these meetings happening in the future.

The history of the Black student movement at the Illinois Institute of Technology shows the specific demands made and the responses to those demands. It can be seen that the responses were not satisfactory and very little change was made. The following section gives an international viewpoint on the movement and shows how the movement has spread internationally.

The article “Black Man in Search of Power”[6] was published in the Times of London in March 1968. The article begins with a quote from “Racial Discrimination in England”, “Coloured people will, themselves, increasingly come to accept the inferior role that is allotted to them in society, until the gap between Black and white, the disparity between national social equality and hard reality, becomes so great that the main outlet for the talents of able colored people is the leadership of revolt”[40]. The author states that this is already happening in England. “Coloured people are becoming the new working class, but unlike the white poor of Disraeli’s[41] nineteenth century they are hindered by the colour of their skin and from scrambling from their position at the bottom of the pile. Not only do they find difficulty in obtaining housing and jobs, but the difficulties of communication and poor contact with white authority are turning them towards bitter introspection and throwing them upon their own resources”[42]. This is a mirror image of the beginning quote as the Black civilians in England are relying on themselves to create a revolution. The article then discusses the difference between the situation in Britian and the situation in America: British police are not armed; colored people in Britain make up 2% of the population compared to 11% in America. The author believes that “the danger is, however, that the pattern forming in America will, like so much else in the way of the fashion exported here,

encourage imitation"[43]. The essay then talks about the movements which politically aware Black militants in Britain are part of. These movements involve student power with Black nationalism. "They are protesting against big, distant, centralized, anonymous authority, whether nationalized, private enterprise, trade union, Government, or educationak"[44]. The next section is called "Parties split"[45]. It states that American society has already been divided into Black and white, and Britain is in danger of doing the same. "The simple truth is that in Africa, America, and Britain, Black people are protesting against entrenched white privileges. Their voices are beginning to sound similar…The American Black Power creed is being exported to Britain"[46]. This shows how the Black movement of America is starting in Britain as well. It shows the influence that big movements have even internationally.

In February 1969 an article title "What British Universities Can Learn From America" by Brian MacArthur was published. The article starts out by stating what student issues are going on in American universities. Student issues in the US are concentrated "in the demand for Black and Brown power on the campus"[47]. The author suggests that the issues that are happening in the US will also occur in Britain. MacArthur then discusses that a serious problem in Britain "has been the lack of educated Blacks to offer not only university teaching but also leadership in the community"[48]. The author hopes that "if and when a Black student union is set up in Britain, universities will not be disfigured by the violence that is now erupting on and outside American campuses"[49]. The author then states certain acts of violence that have taken place at American universities: two students in Los Angeles were shot dead. A building was gutted in Berkeley. In San Francisco, students were striking and 500 got arrested. The author wishes that Britain learns from what is happening in America so that this violence does not repeat itself in Britain. The article goes on to discuss the educational differences in British and American universities such as food on campus, disciplinary practices, and how hard the work is (apparently in American universities students are worked harder). The author talked to Dr. Byron Atkinson, the Dean of Students at UCLA. Dr. Atkinson felt that a system of "rigidity and traditionalism…has now been replaced by an utter willingness to listen to students and to attempt to meet them half-way instead of head-on"[50]. This change in the system can be seen by encouraging student evaluations of courses and the "validity of student complaints about undergraduate teaching"[51]. The article ends with a touching statement from a dean's decalogue such as "a student is not dependent on me I am dependent on him…A student Is not an interruption of my work he is the purpose of it…A student is the life blood of my campus"[52]. This article shows what issues are arising in American universities, the effect of the student movements, and how Britain should learn from what is happening in America at the time.

This history is important because it shows the impacts of systemic racism on the education of Black students. Black students rose up to fight against this and it became a national movement which even spread globally. This knowledge is useful because it shows the impact that students can have if they are organized and persistent.

**Works Cited**

(1,2,5-10)Harding, Vincent. “Black Students and the 'Impossible' Revolution.” Ebony, Aug. 1969, pp. 141–148, “Black Students and the 'Impossible' Revolution Part II.” Sept. 1969, pp. 97–104.

(3,4,11-16)Turner, James. “Black Students and Their Changing Perspective.” Ebony, Aug. 1969, pp. 135–140.

(17-20)“Black Student Group Expresses Grievances To IIT Administration; Administration Reaction.” 10 May 1968, p. 1.

(21-26)“AsIseeIT; What Goal Does Black Student Action Seek.” 10 May 1968, http://216.47.157.203/technews/volume84/tnvol84no11.pdf#page=2.

(27-29)“ITSA President Comments on Black Student Petition.” 17 May 1968.

(30-34)“Black Students, Concerned Whites, and Administrative Committee Begin Discussions of List of Grievances.” 17 May 1968,

(35-39) “List of Resolutions Presents Demands of Black Students.” 25 Oct. 1968.

(40-46“Black Man in Search of Power: 6.” The Times,16 Mar. 1968, p. 8, “List of Resolutions Presents Demands of Black Students.” 25 Oct. 1968.

(47-52) MacArthur, Brian. “What British Universities Can Learn from America.” The Times, 8 Feb. 1969, p. 8

## Conclusion and Acknowledgments

Our goal of creating Project 1890 is to help change the narrative of Black history and IIT. It is important to acknowledge a painful past in order to move forward, and we hope that others reading this will reflect on our University's role in the surrounding community.

We would like to acknowledge Dr. Mindy Pugh for the wealth of information we gained from her History of Bronzeville talk. Much of that information formed the basis of this project and we are very grateful for her willingness to share her knowledge with the campus community.

We would also like to acknowledge members of IIT's 4A, the African American Alumni Association for their support in this project, namely Zanette Sanders, Calvin Young, Bern Key, Sherri Littlejohn, April Welch, Tanya Powell, Ken Burns Raymond Nelson, Lisa Montgomery, and Celeste Redmond-Smith for their guidance and support.

# Replication: Knowledge and Luck

Aminah Ahmed [*,1]

**I. ABSTRACT**

Is a belief true when it is due to a lucky guess? This study replicated Turri and colleagues' (2014) study investigating how we make judgments of others' knowledge (i.e., what they know). In this replication, 97 participants completed a short survey that compared three different conditions–one in which the character made the right decision due to their knowledge ("Knowledge"), one in which the character made the right decision due to a lucky guess ("Gettier"), and one in which the character was wrong ("Ignorance"). It was found that subjects attributed knowledge and reasonableness to the characters depending on the condition they were in. Subjects attributed higher knowledge ratings to the characters in the Gettier condition than in the Knowledge and Ignorance conditions. However, ratings for reasonableness, the soundness of the characters' conclusions, were higher in the Knowledge condition than the Gettier and Ignorance conditions. Overall, findings were in line with the Turri et. al (2014) study, demonstrating that these effects can replicate. We also found support for an additional hypothesis for the gender differences in knowledge ratings: the female character ("Emma") was rated lower in knowledge than the male characters ("Darrel" and "Gerald") regardless of the condition.

*Keywords:* Luck; Knowledge; Gettier

**II. INTRODUCTION**

In 2014, Turri and colleagues conducted a study to understand how people perceive knowledge and make judgments about what others know and what is due to luck. Following this study, Advances in Methods and Practices in Psychological Science (AMPPS) (2015) conducted a worldwide replication to confirm his results and the conclusions that were made about the interaction between knowledge and luck-related factors [1]. In the original study, participants were required to read one of seven stories which represented three luck-related factors that influence people's judgments about knowledge (threat, disruption, and replacement) and answer questions about the character (Emma) in the story. This allowed researchers to measure the rate at which they attributed knowledge to the character [2]. By doing so, researchers discerned whether or not a participant attributed Emma's conclusion to her knowledge or a lucky guess, alluding to how people make judgments about those around them.

In the replication study conducted by AMPPS (2015), researchers reduced the number of conditions to three to represent each of the general luck-related factors (threat, disruption, and replacement) [1]. Threat refers to a factor that inhibits one's perception of a situation. Disruption refers to a factor that can remove one's attention. Replacement refers to the subject of the character's attention being replaced by another subject. During the course of this study, participants were required to read all three stories, but they were presented in different orders to reduce any effects that may have resulted from the previous story [2]. This was done through an online survey [1], which consisted of the three short stories, comprehension questions, and demographic questions.

The results of both studies found that participants assigned knowledge to the character at a significant rate depending on the situation the character was in. This allowed researchers to conclude that knowledge attributions do not take into account the luck of a threat that fails to prevent a person from finding the truth. However, they were able to conclude that knowledge attributions take into account the luck that is involved with an unnoticed disruption and a change in the explanation for why a belief is true [2]. Turri and colleagues (2014) also found that when the explanation changes for why a belief is true, knowledge attributions are susceptible to changes in the truth, meaning that one is more inclined to declare that knowledge was involved when the new truth is similar to the original truth [2].

Replicating the Turri et al. (2014) study proved to be important in proving the reliability and validity of their findings. The replication was also useful for understanding how people make judgments about those around them. These judgments often play a key role in the manner in which people interact with one another and the extent to which they give credit or assign blame for a certain outcome. This study allowed for an increased understanding of the relationship between knowledge and luck-related factors, and how people make decisions about the relationship between luck and success. As described by

Loveday (2018), people often attribute success to luck and failure to ability [3]. Combining the findings from this study and the Loveday (2014) study could be used for future social psychology studies that seek to understand interpersonal relationships, jealousy, and the phenomenon of social desirability [3].

**Literature Review**

The Turri et al. (2014) study has been frequently cited and prior research examining judgements about these Gettier Type Cases or lucky guesses have been mixed in the past [2]. Some studies supported the theory of Gettier Type Cases, while others disproved it. Further, according to Blouw et al. (2014), Gettier Cases are often used in experiments, in which the protagonist has a Justified True Belief (JTB) that is not considered to be knowledge [4]. A JTB is an idea that is supported by related information that allows it to be seen as a valid belief, which was traditionally perceived as knowledge [3]. However, subsequent studies on Gettier Cases found that lay people were able to make a clear distinction between the two concepts. This alludes to how people make judgments about the presence of knowledge and luck when interacting with those around them. A conflicting study done by Starmans and Friedman (2012) found that people typically attribute knowledge when a belief is both justified and true, which is in line with the traditional perception of JTBs [5]. This is similar to the findings of Turri et al. (2014), in that when beliefs were perceived to be the same as the truth, knowledge was assigned [2].

**III. METHODS**

**Participants:**

97 participants took part in this study, ranging from the ages of 18-33, with 40 being females and 39 being males after exclusions. All of the subjects resided in the United States, however, 26.9% were born abroad, such as in China, India, and Bulgaria. When asked their race/ethnicity, 34.2% of participants identified as White, 5.1% as Black, 20.3% as Latino/a, 0% as Australian Descent, 36.7% as Asian, 2.5% as Southeast Asian Descent, 1.3% as Native American, 0% as Hawaiian Descent/Pacific Island, and 6.3% as Other. In order to demonstrate how college students view the interaction between knowledge and luck, only those over the age of 18 were recruited to participate in the study. Thus, participants under the age of 18 were excluded from the data. Furthermore, to ensure that all of the results are representative of the data, responses that were due to a computer malfunction were omitted. Responses that were incoherent or alluded to a prior understanding of the study's purpose were also omitted to ensure that there were no outliers in the data.

**Procedure:**

Before participants were run and data was collected, the study was registered on the Open Science Framework (OSF) (https://osf.io/zje64/) in order to make available all of the resources, data, etc. that were used. Subjects from the Illinois Institute of Technology were recruited in person via a booth in the McCormick Tribune Campus Center and online through SONA, a subject pool software. Participants who completed the study in person were given candy as an incentive and compensation for their time, while those who took part through SONA were awarded 0.5 SONA credits that could be used as credit for their psychology classes.

We followed the same procedure as the Turri et al. (2014) study [2]. Participants were exposed to three different conditions: Knowledge, Gettier, and Ignorance. Within each condition, different scenarios were presented involving a character (Emma, Darrel, or Gerald) making a decision. These conditions were presented in a random order to have a within-subject design. In the Knowledge condition, the character was required to make a decision that could be attributed to their knowledge. In the Gettier condition, the character's decision could be attributed to a lucky guess, and in the Ignorance condition, the character's decision was incorrect due to a lack of knowledge and luck. The nature of these conditions was not made clear to the participants in order to prevent biased decisions about the characters' knowledge and the role of luck in their decisions. Character names and the scenarios (e.g., identifying between a fake diamond and a real diamond in a jewelry store) were randomly presented across all three conditions.

This study was conducted via an online survey. Upon opening the link to access the study, the consent form was presented to thoroughly inform subjects about the study. The next page began with the first of three scenarios that the participants saw. Following each scenario, participants were prompted to answer a few short questions about their perceptions of how knowledgeable the participant was in that scenario, and how reasonable the conclusions they drew were. These questions will be explained in the Measures section.

The last few pages of the study prompted subjects to answer demographic questions (age, gender, country of residence, country of birth, race/ethnicity, number of years in school, and proficiency in English). Participants were also asked if their participation qualified them for the

lottery and if they were being compensated. In the case of this study, participants were asked to include that they were compensated with SONA credit and/or candy.

**Measures:**

After each scenario, participants were asked questions about the character to test their comprehension of the story. These questions asked the reader to attribute the character's answer to ability/inability or good luck/bad luck, as well as if the character's conclusion was reasonable or unreasonable among others that assessed whether or not they attributed the character's understanding of their circumstances to knowledge or luck. The comprehension questions that were used were the same as those used by Nagel et al. (2013), and two answer choices were presented in a multiple-choice format as well as a sliding scale [6]. Answer options for the multiple-choice questions varied depending on the question. For the sliding scale, subjects were asked to slide the bar in the direction of their answer. Answer options were dependent on the question. For example, for the question asking if the character's answer was due to knowledge or luck, subjects slid the bar in the direction of ability/inability or good luck/bad luck.

The feedback questions at the end of the study were the same as those used by AMPPS (2015) [1]. These questions asked participants about their experiences and thoughts while taking the survey. Answer options were on a scale similar to a Likert scale with nine points in which participants had to select the answer that they agreed with most. For example, when asked how much they enjoyed the study, answer choices ranged from "I enjoyed the study a lot" to "I did not enjoy the study at all". At the end of this section, subjects were provided with spaces to leave comments, indicate what they thought the aim of the study was, etc. Answers to these questions were used to assess a person's understanding of the study, and whether or not they had prior knowledge that may have impacted their responses.

## IV: RESULTS

Descriptive analyses of the data found that participants ranged from 18 years old to 33 years old ($M$ = 20.3, $SD$ = 2.39). 40 subjects identified themselves as female and 39 as male. Lastly, 34.2% of the subjects were White, 5.1% were Black, 20.3% were Latino/a, 36.7% were Asian, 2.5% were of Southeast Asian Descent, 1.3% were Native American, and 6.3% were of another race. None of the subjects identified as being of Hawaiian Descent/Pacific Island or Australian Descent.

A repeated-measures ANOVA was performed in order to evaluate participants' ratings for knowledge in terms of the three conditions. The ANOVA showed a significant difference in ratings across the scenarios $F(2, 158) = 8.30$, $p < 0.001$, $\eta_p^2 = 0.095$. A Tukey's Post Hoc Test evaluated the differences in subjects' ratings of the characters knowledge across the conditions. The comparison found that there were significant ($p < 0.001$) differences between the Ignorance ($M = 28.9$, $SD = 38.1$) and Gettier ($M = 55.8$, $SD = 40.2$) conditions. Subjects tended to assign a lower knowledge rating for the Ignorance condition and a higher rating for the Gettier condition (See Figure 1). The comparison also showed that there were no significant differences ($p$'s $> 0.05$) in knowledge ratings between the Ignorance and Knowledge conditions, as well as between the Knowledge and Gettier conditions.

Another repeated-measures ANOVA was created to examine subjects' ratings for reasonableness across the three scenarios. The ANOVA depicted a significant difference in ratings for reasonableness across all of the conditions $F(2, 158) = 3.45$, $p < 0.05$, $\eta_p^2 = 0.042$. A Tukey's Post Hoc Test was run to examine the differences in how subjects rated the reasonableness of the character's conclusion between the conditions. It was found that there

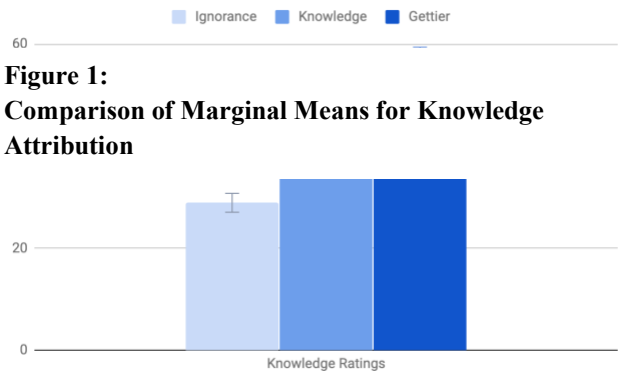


**Figure 1:**
**Comparison of Marginal Means for Knowledge Attribution**

*Note.* Based on the results of the ANOVA, it was found that there were significant differences in knowledge attribution between the Ignorance and Gettier conditions.

were no significant differences ($p$'s $> 0.05$) in ratings for reasonableness between the Ignorance and Knowledge conditions, as well as between the Ignorance and Gettier conditions. This means that ratings for reasonableness for the Ignorance condition were similar to those of the Knowledge ($M = 88.1$, $SD = 19.7$) and Gettier ($M = 78.6$, $SD = 30.4$) conditions. However, the Post Hoc Test

indicated that there was a significant difference ($p < 0.05$) in the reasonableness ratings between the Knowledge and Gettier conditions. Subjects' ratings for reasonableness in the Knowledge condition were higher than those in the Gettier condition (See Figure 2).

Moreover, a repeated-measures ANOVA was run to compare knowledge ratings based on the gender of the character. The ANOVA found that there was a significant difference in how the characters were rated for knowledge,

**Figure 2:**
**Comparison of Marginal Means for Attribution of Reasonableness**


*Note.* The results of the ANOVA showed that there were significant differences in ratings for reasonableness between the Knowledge and Gettier conditions.

$F(2, 158) = 15.4$, $p < 0.001$, $\eta_p^2 = 0.163$. A Tuckey's Post Hoc Test indicated that there were significant differences

**Figure 3:**
**Comparison of Marginal Means for Knowledge Attribution Based on Character**

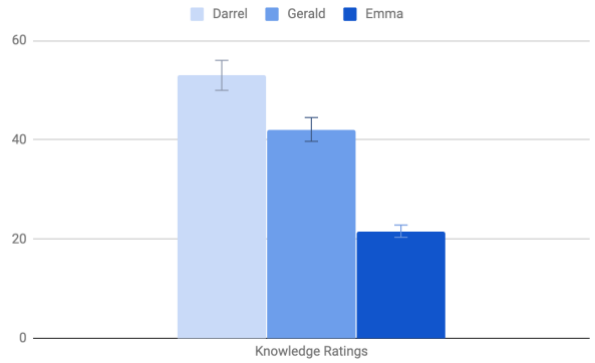


*Note.* The ANOVA sought to understand how participants assigned knowledge to the different characters. As seen in the graph, Emma was often rated as having less knowledge than Darrel and Gerald.

($p$'s $< 0.001$) in how participants rated the characters' knowledge between Darrel ($M = 53.0$, $SD = 42.7$) and Emma ($M = 21.6$, $SD = 29.5$), as well as between Gerald ($M = 42.1$, $SD = 40.5$) and Emma. As seen in Figure 5, subjects often rated Emma as having less knowledge than Gerald and Darrel.

Turri et. al (2014) found that gender did not influence how participants attributed knowledge and reasonableness to the characters, however, the t-tests demonstrated that this was not the case for the replication. Furthermore, the first ANOVA proved Turri and colleague's (2014) findings that knowledge attribution was not significantly different between the Knowledge and Gettier conditions, but that ratings did, in fact, differ between the Ignorance and Gettier conditions.

## V. DISCUSSION

It was found that, in general, participants often provided higher knowledge ratings in the Gettier condition as opposed to the Knowledge and Ignorance conditions. This difference was especially apparent between the Ignorance and Gettier condition, which may hint at the influence of luck. Subjects may have rated characters as having greater knowledge if the threat or disturbance in the story closely resembled the truth. Interestingly, participants tended to rate reasonableness in the Gettier condition lower than in the other two conditions. This contrasting finding (i.e. the higher ratings in knowledge and lower ratings in reasonableness) for the Gettier condition may be due to a number of other variables, such as a lack of understanding of the question or the wording used in the stories as ratings for reasonableness were highest in the Knowledge condition.

An additional test was run on the gender of the characters to see if gender biases and stereotypes were involved in knowledge attribution. The ANOVA comparing knowledge ratings based on the gender of the characters found that there was a significant difference in how Emma was rated compared to the two male characters, Darrel and Gerald. Emma was often rated as having less knowledge than the other characters. This may be due to possible gender biases relating to the knowledge and competence of men versus women, as seen in Fennema et al. (1990) and Dow (2009) [7,8].

In the original study, Turri et al. (2014) ran tests comparing the impact when the threat or disruption was successful (i.e. resembled the truth) to when the threat failed (i.e. failed to distract the character). The replication

did not call for these specific tests to be run, however, similar results were found. Turri et al. (2014) found that when the threat resembled the truth, knowledge ratings were high in the Gettier condition, which was the same finding for the replication.

The final sample size for this study was relatively small ($N = 79$), which poses a limitation for the results of this study, as a smaller sample size reduces the generalizability of results. Had there been more time to advertise the study and recruit participants, the sample size may have been larger and different results may have been found. Furthermore, the sample primarily consisted of college students who generally had the same level of education and proficiency in English which would have impacted their comprehension of the stories and their respective questions. If the sample had included people of different education levels and language proficiency, understanding of the scenarios would have varied and responses would have been more distributed, leading to different findings in terms of knowledge ratings. These findings could have been more suggestive of the influence of luck on knowledge and how we make judgments about those around us. Furthermore, while many studies have shown that gender biases can play a role in knowledge attribution as well as other areas, it cannot be said certainly that this is the reason why Emma received lower knowledge ratings than Darrel and Gerald. The wording of the stories may have resulted in the difference as well. If the names of the characters had been omitted or the wording was the same for all of the stories, it may have been easier to point out the reason behind the different ratings since gender of the characters and differences in the wording of the stories would have been controlled for.

Future research could include running the replication with a more diverse sample in terms of the level of education. As previously mentioned, this could lead to more varying ratings of knowledge and may indicate the influence of luck on knowledge. A study using the same stories without the names of the characters would allow for a closer analysis of how gender impacted knowledge ratings. While this would not lend much to the question about the relationship between knowledge and luck, it would provide useful information on how gender plays a role when making judgments about those around us. This would also help in developing methods to address gender biases and stereotypes and create a broader understanding between people to prevent these factors from playing a role in employment, voting, gender gaps [9], etc.

The results of this study prove that the findings from the Turri et al. (2014) study are reliable and that they can be reproduced. They also show that luck has an effect on knowledge and how we perceive the level of knowledge of others. The findings from the ANOVA on knowledge ratings based on the character lend support to previous studies that have found that women are rated differently in terms of knowledge and competence. These results raise new questions that can be implemented in future gender studies. Moreover, knowing how people make judgments about the knowledge of others could aid teachers and administrators in creating different types of testing environments, such as individual stations, so that students do not feel pressured to perform in a particular manner by the presence of others who may be perceived to have greater knowledge. Using written comprehension tests would help divide students based on reading level rather than how they respond to verbal questions, thus allowing those who need extra help and attention to obtain the resources they need.

## VI. REFERENCES


[1] Turri, J., Blouw, P., & Buckwalter, W. Registered Replication Report. *Advances in Methods and Practices in Psychological Science,* 1-75, (2015)

[2] Turri, J., Blouw, P., & Buckwalter, W. Knowledge and Luck. *Proceedings of the Annual Meeting of the Cognitive Science Society*, *36*(36), (2014)

[3] Loveday, V. 'Luck, chance, and happenstance? Perceptions of success and failure amongst fixed-term academic staff in UK higher education.' *British Journal of Sociology*, *69*(3), 758–775, (2018)

[4] Blouw, P., Buckwalter, W., & Turri, J (forthcoming). Gettier Cases: A Taxonomy. In R. Borges, C. de Almeida, & P. Klein (Eds.), *Explaining Knowledge: New Essays on the Gettier Problem*. Oxford University Press. (2014)

[5] Starmans, C., & Friedman, O. The folk conception of knowledge. *Cognition*, *124*(3), 272–283, (2012)

[6] Nagel, J., Juan, V. S., & Mar, R. A. Lay denial of knowledge for justified true beliefs. *Cognition*, *129*(3), 652–661, (2013)

[7] Fennema, E., Peterson, P.L., Carpenter, T.P. *et al.* Teachers' attributions and beliefs about girls, boys, and mathematics. *Educ Stud Math* 21, 55–69 (1990)

[8] Dow, J. K. Gender differences in political knowledge: Distinguishing characteristics-based and returns-

based differences. *Political Behavior*, *31*(1), 117–136, (2009)

[9] Moss-Racusin, C. A., Sanzari, C., Caluori, N., & Rabasco, H. Gender bias produces gender gaps in STEM engagement. *Sex Roles: A Journal of Research*, *79*(11–12), 651–670, (2018)

# Detection of BaxΔ2 Positive Macrophage in Breast Tissues

Anam Adil[*,1], Sana Basheer, Dr. Jialing Xiang [*]

[*]Department of Biological Sciences, Illinois Institute of Technology, Chicago, IL 60616, USA

## I. ABSTRACT

BaxΔ2 is an isoform of the Bax gene and functions as a tumor suppressor. Its gene products can cause programmed cell death. In previous studies, the lab found that BaxΔ2 is found in cells throughout various human organs [2]. Based on the morphological structure of these cells, it is hypothesized that some of these cells may be macrophages. This project focuses on identifying whether BaxΔ2 positive macrophages are found in breast tissue. Six different patient cases with varying grades of cancer were looked at and their cancerous tissue was compared to their normal tissue. A process known as Immunofluorescence Staining uses certain antibodies to test for certain antigens (markers) in a sample of tissue. Co Immunostaining was used to stain for two different markers. In this case, each tissue slide is stained with antibodies against macrophages and BaxΔ2. We found that normal breast tissue had a greater amount of BaxΔ2 in comparison to cancer adjacent tissue, stage 1, 2, and 3 malignant tumors. From the data, it was also analyzed that almost all macrophages were BaxΔ2 positive, however not all BaxΔ2 positive cells were macrophages. This suggests that in addition to its apoptotic function, BaxΔ2 positive macrophage may play a role in immune response. Analyzing the amount of BaxΔ2 present in different types of tissue could also serve as a prognosis marker for cancer patients. In addition, it can be explored if cancer cells expressing BaxΔ2 are more sensitive to chemotherapy treatments.

## II. INTRODUCTION

In 2019, the estimated leading site of new cancer diagnoses in females will be breast cancer. The death rate due to this carcinoma declined by 40% from 1989 to 2016 [1]. This progress reflects improvements in new therapies and treatments that are being made continuously. The investigation of BaxΔ2 in breast tissue can hopefully contribute to this trend. The female breast is primarily composed of fat cells known as adipose tissue. Breast cancer generally arises in the terminal lobule ducts. This is the gland that produces milk in nursing women. It begins when cells in the breast begin to grow out of control, spread when they get into the blood or lymph system and then are carried to other parts of the body. The stage of the breast cancer is determined by its characteristics: the size of the tumor, whether it has spread, and the number of lymph nodes affected. Based on the tissue, one can identify the stage depending on the quantity of cells and the amount of collagen. Based on morphological structure, one can speculate what type of cell it is. Previously in the lab, colon tissue was stained for BaxΔ2 [4]. Macrophage-like cells were evident in the images. One of the ongoing projects in the lab is to confirm whether some macrophage-like cells are in fact macrophage. This project aims to study this in healthy and cancerous breast tissue.

## II. METHODS

Female Invasive breast ductal carcinoma tissue microarray containing six cases and quadruple cores per case was obtained from Biomax as shown in Figure 1. Patient information is specified in Table 1. Tissue slides were baked prior to starting.

**Figure 1. BR251c - Female invasive breast ductal carcinoma tissue microarray**

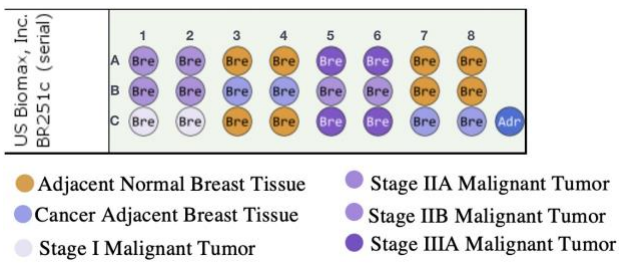

**Table 1. Patient Samples**

| Case | Age (Years) | Grade | Tissue Pathology |
|---|---|---|---|
| 1 | 40 | 2 | Stage IIB Malignant Tumor |
| 2 | 54 | 2 | Stage IIIA Malignant Tumor |
| 3 | 54 | 2 | Stage IIB Malignant Tumor |
| 4 | 29 | 2 | Stage IIA Malignant Tumor |
| 5 | 38 | 3 | Stage 1 Malignant Tumor |
| 6 | 38 | 3 | Stage IIIA Malignant Tumor |

**Immunohistochemistry, Paraffin-Fixed Tissue: Fluorescence.**

The tissue slide was deparaffinized using xylene, ethanol, and PBS buffer solution. The antigen was retrieved by heating the slide in a sodium citrate buffer. The slide was washed again with a PBS buffer. It was then treated with the BaxΔ2 (2D4) mouse monoclonal primary antibody. The slide was incubated in 3% BSA in PBST blocking buffer for 2 hours at room temperature in an incubation chamber. The primary antibody was prepared in a 1:100 dilution. 200 uL of the antibody dilution was placed into each chamber and gently pressed on the tissue slide, top side down. The slide was then incubated overnight in a damp chamber in a 4°C refrigerator. The slide was then washed 4 times with alternating 1X PBS and TBST for 10 minutes each. The slide was then treated with CD68 rabbit monoclonal primary antibody. The antibody was prepared in a 1:100 dilution. The slide was incubated for 1 hour at room temperature. The slide was then washed 4 times with alternation 1X PBS and TBST for 10 minutes each. The following steps were done under foil, protected from light. The secondary antibodies, an anti-mouse fluorescent marker at 488 nm and an anti-rabbit fluorescent marker at 647, were prepared in a 1:200 dilution in PBS. The slides were incubated in 200uL of the antibody and buffer solution. The slide was incubated for 1 hour in a damp chamber at room temperature. It was washed 4 times with alternation 1X PBS and TBST for 10 minutes each. The nuclei were stained by incubating the slide in 200 ul DAPI prepared in a 1:1000 dilution in PBS for 5 minutes. It was rinsed with 1X PBS once. The slide was then mounted using Fluoromount. The tissue slide was visualized using a Keyence BZ-X710 fluorescence microscope.

## III. RESULTS AND DISCUSSIONS

**Figure 2. BaxΔ2 and Macrophage Fluorescence in Varying Tissue Types**

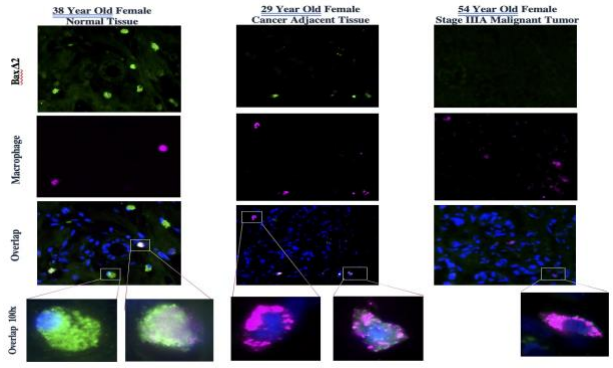


The images shown in Figure 2 were captured on a Keyence BZ-X710 fluorescence microscope. The green channel was used to visualize BaxΔ2, while the far-red channel was used to identify macrophages. An overlap between the two markers was indicated by a white signal. The nuclei were seen using the blue channel.

**Figure 3. Quantification of BaxΔ2 positive cells and macrophages in varying tissue types**

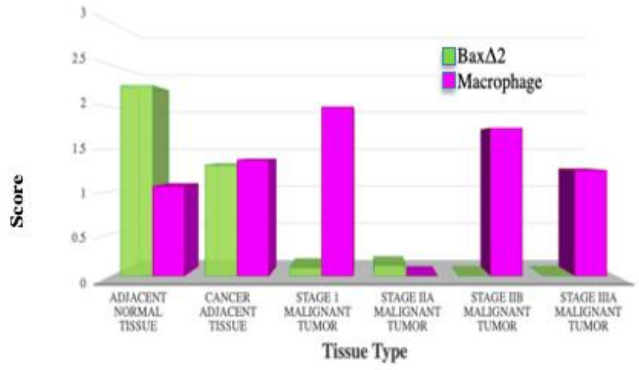


The findings in Figure 3 display the quantification of BaxΔ2 positive cells and macrophages present in a tissue. A scoring system based on a scale from 0-3 was used. This scale has been established by previous researchers in this lab [3]. A score of 0 is representative of 0-1% cells being positive. A score of 1 is 1-3%, 2 is 4-6%, and 3 for >10%.

Majority of BaxΔ2 was detected in normal tissue, but not in cancerous tissue. Some of the cells found in the breast were macrophage marker positive. Since CD68 can also be positive for other types of cells, future work in the lab must

be done to confirm whether these cells are in fact macrophage. Also, if they are macrophages, then we need to study the function of BaxΔ2 in macrophage.

## IV. REFERENCES


[1] Cancer Statistics, 2019. Published early online January 8, 2019 in *CA Cancer Journal for Clinicians*. First author Rebecca L. Siegel, MPH, American Cancer Society, Atlanta, Ga

[2]Haferkamp, B., Zhang, H., Lin, Y., Yeap. X, Bounce, A., Sharpe, J., Xiang, J. (2012). BaxΔ2 is a novel Bax isoform unique to microsatellite unstable tumors. *J. Biol. Chem. 287*(41), 347229.

[3] Mañas A, Davis A, Lamerand S, Xiang J (2018). Detection of pro-apoptotic BaxΔ2 proteins in the human cerebellum. Histochem Cell Biol. 2018 Jul;150(1):77-82. doi: 10.1007/s00418-0181669-6

[4] Zhang H, Lin Y, Manas A, Zhao Y, Denning MF, Ma L, Xiang, J. (2014) BaxΔ2 promotes apoptosis through caspase-8 activation in microsatellite unstable colon cancer. *Mol. Cancer Res.*
*12*(9), 1225-23.

# Application of Molecular Imprinted Polymer Technology to detect the SARS-CoV-2 Virus through the Development of a Novel Breathalyzer-like Device

Laasya Devi Annepureddy [a], Crystal Keigher [a], Samantha Warpecha [a], Amna Haneef [a]

[a] Biomedical Engineering, Illinois Institute of Technology, Chicago, IL, 60616, USA

## I. ABSTRACT

The COVID-19 pandemic has resulted in over 2 million deaths and affected around 100 million people worldwide (CDC). Across the globe, a pandemic warning system had failed when the SARS-CoV-2 virus hit. The key reason behind the ineffective response or unpreparedness is the lack of rapid diagnostic testing at the onset of the pandemic that could have been used to widely detect the presence of the virus. The lack of a highly sensitive rapid test, forces laboratories and hospitals to use conventional nucleic acid testing methods which are time consuming, labor intensive and expensive [4]. To solve this problem, we propose a 'breathalyzer-like 'device that will be able to detect the SARS-CoV-2 virus in seconds while being extremely user friendly, highly sensitive and cost effective. This breathalyzer-like device will detect SARS-CoV-2 by the binding of molecularly imprinted polymers (MIPs) to the virus's spike protein. MIPs are synthetic receptor molecules that can mimic ACE-2 receptors and offer an inexpensive, rapid, sensitive, easy-to-use, and highly selective receptor for electrochemical biosensors [8]. MIP based detection has been widely used in literature in the detection of human viral or bacterial pathogens which has shown >90% accuracy.

## II. INTRODUCTION

The Covid-19 pandemic is an ongoing global health crisis, with a staggering death toll that continues to increase. The severe acute respiratory syndrome coronavirus 2 (SARS-CoV-2), was identified in Wuhan, China in December 2019. The viral outbreak was categorized as a pandemic in March, 2020 by the World Health Organization (WHO). As of now, according to the numbers reported by every country to the WHO, the total number of cases has surpassed 122 million and over 2.7 million deaths have been attributed to it. The pandemic has had an adverse impact on the international community, not only affecting the global economy, but also, mental health, employment, work, education, and political aspects as well. In order to counter the spread of the disease many forms of restrictions were implemented globally, including regional and country wide lockdowns, quarantines, travel bans, and evacuation of foreign citizens.

***Figure 1***: [14] Schematic representation of the SARS-CoV-2 virus. An enveloped positive-sense RNA strand with spike (S) and membrane (M) glycoproteins, as well as envelope (E) and nucleocapsid (N) proteins.

All coronaviruses have an animal origin, either from bats or rodents. The SARS-CoV-2 virus either originated through natural selection in an animal host before zoonotic transfer to humans or natural selection in humans after zoonotic transfer [15]. The pangolin is believed to be the intermediate host of SARS-CoV-2 originating from bats and finally transferring to humans as it was illegally sold in the Chinese wet markets. The SARS-CoV-2 virus, based on sequence alignment and

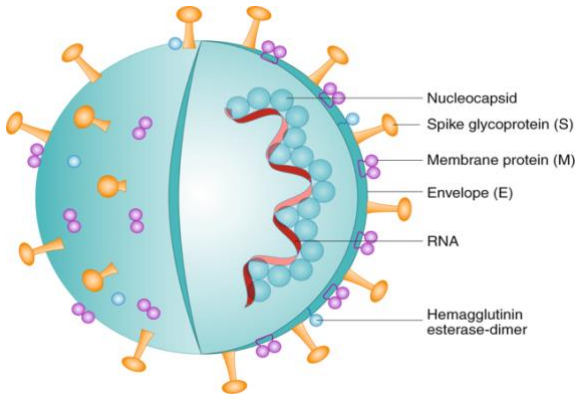


evolutionary tree analysis, has been deduced to be a member of the group B viruses, of genus Betacoronavirus in the family of Coronaviridae, of the order Nidovirales [16]. It is an enveloped, single-stranded RNA virus. The genomic sequence of this newly

emerged virus is similar to that of SARS-CoV with a 79.6 percent sequence identity [20] It consists of four structural proteins, spike, envelope, membrane and nucleocapsid proteins [15]

The spread of the virus occurs via droplet transmission that is produced when coughing or sneezing, through personal contact, or by coming in contact with contaminated surfaces [12]. It may also be transmitted in the form of aerosol particles, by liquid droplets that convert into numerous smaller particles [20]. The virus binds to epithelial cells in the respiratory tract, replicates and begins to migrate down to the airways, entering alveolar cells. This rapid replication may trigger a strong immune response [23]. The incubation period of the onset of symptoms ranges from 1 to 14 days. It has a broad effect on people, ranging from an asymptomatic infection or a mild illness of the respiratory tract, and may go up to severe pneumonia, respiratory failure, and eventually death [15]. Patients with a median age of 59 and above, with people with pre-existing disease are at a greater risk [23]. According to a study, there was a high viral load in the upper respiratory tract, during the first week of symptoms, thus the transmissibility was high due to virus shedding, and it was also recorded to be high during mild infections or asymptomatic stages [23]. The mortality of the virus depends on factors such as sex, ethnicity, and outdoor environment, such as the level of air pollution [25].

Across the globe, a pandemic warning system had failed when the SARS-CoV-2 virus hit. The key reason behind the ineffective response or unpreparedness is the lack of rapid diagnostic testing at the onset of the pandemic that could have been used to widely detect the presence of the virus. The lack of a highly sensitive rapid test, forces laboratories and hospitals to use conventional nucleic acid testing methods, which are time consuming, labor intensive and expensive. Hence our team proposes a simple handheld breathalyzer-like device that allows for a rapid detection of COVID-19 by the binding of molecularly imprinted polymers to the spike protein on the surface of the virus. The device will act as a rapid point of care or at home diagnostic test that is highly sensitive and specific while being cost effective. The proposed device will be easy to use, where the user will only need to exhale particles in a tube. The device comprises a MIP modified graphene electrode system that will detect the resistance change and a transducer will convert the physical signal to an electrical signal. This electrical signal can then be detected and the device will be able to output the results into the user's smartphone via bluetooth, resulting in a positive or negative result for the virus being detected.

### *1. Rapid Testing for COVID-19*

Rapid COVID-19 tests are a type of COVID diagnostic that yield quick results (usually less than 15 minutes) and are most accurate in patients who have symptoms and are most contagious [25]. Rapid tests are extremely important at this stage of the COVID-19 pandemic because they are able to identify the virus when you are most likely to transmit it [21]. This is critical because people are starting to travel and spend more time with their friends and family as the pandemic progresses and the COVID-19 vaccines are being distributed. So, having a quick, accurate, affordable, and easy to perform test will help to prevent the unknowing spread of the virus to loved ones. Some of the currently available and soon to be available rapid COVID-19 tests are compared in Table 1. All of these tests have been granted Emergency Use Authorization (EUA) by the U.S. Food and Drug Administration (FDA).

Table 1: Comparison of Different Rapid COVID-19 Tests

| Name of Test | Type of Test | Cost (USD) | Sensitivity | Time to Results (mins) | Specificity |
|---|---|---|---|---|---|
| Ellume COVID-19 Home Test [10][11][13] | Antigen- Nasal Swab | 30 | 91-96% | 15-20 | 97% |
| BinaxNOW COVID-19 Ag Card [6] | Antigen- Nasal Swab | 5 | 71.1%* | 15 | 96.9% |
| Lucira COVID-19 All-in-One Test Kit [12] | Molecular-Nasal Swab | 50 | 94.1%* | 30 | 98% |
| Cue COVID-19 Test [7] | Molecular- Nasal Swab | Not Set | 95.7% | 20 | 97.6% |
| ID NOW COVID-19 [9] | Molecular- Nasal or Oral Swab | Varies | 93.3% | 13 | 98.4% |

*Sensitivity was calculated for symptomatic individuals.

The tests displayed in Table 1 are able to be used as point-of-care or at-home tests and all of them require a swab sample from the respiratory tract. The device that we have proposed is also a point-of-care test, but it uses samples from the breath rather than a more invasive method. This is advantageous because many people experience discomfort with tests that require nasal swabs and thus may view a breath test as more desirable. Our device also can obtain results within 30-35 second, which is much quicker than currently available rapid tests that typically require 15 minutes for the results [3]. Furthermore, the sensitivity and specificity of our device is expected to be 90% or greater, which is comparable to the other rapid testing methods being produced (see section 3 for specifics on the proposed device).

There are also new tests being developed that use breathalyzer-like technology similar to our proposed

device. One such test being developed by Texas A&M University and Worlds Inc detects the volatile organic compounds within a patient's breath that are present when the body is fighting infection to determine whether or not they should be tested further for COVID-19. After further development of the device it also may be used as an alternative for the PCR test (which is currently the gold standard for COVID-19 testing) [28] Another

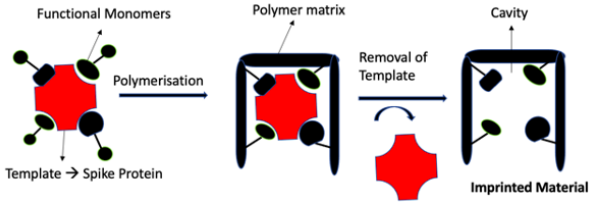


breathalyzer-like device being developed is from Scentech Medical, which is also able to detect the volatile organic compounds in an individual's breath. This device is said to have over 90% accuracy in detecting COVID-19 and is also able to differentiate between samples that are positive, negative, and those that have COVID-19 antibodies. [32] This device uses gas chromatography, mass spectrometry, and a ReCIVA collecting device to detect the presence of volatile organic compounds specific to those infected with COVID-19 [33] these tests both use volatile organic compounds to detect the presence of COVID-19 infection, while our device uses MIP technology. The use of MIPs allows our device to be highly specific to the COVID-19 virus and be very inexpensive relative to these devices. The application of this MIP technology is explained further in the next section.

***Figure 2:*** *[1]* Formation of an MIP binding cavity. Immobilization of a template protein on a surface, formation of MIP around the template, elution of template protein to reveal empty binding cavity.

### *2.Application of MIPs*

The proposed breathalyzer-like device is a rapid diagnostic test for COVID-19 that is primarily based on molecularly imprinted polymer technology. MIPs are functional synthetic receptor molecules with specialized molecular target selectivity. MIPs offer an inexpensive, rapid, sensitive, easy-to-use, and highly selective receptor for electrochemical biosensors.[8] MIPs have high selectivity and specific recognition capabilities for a target molecule called a template. The molecular imprinting process essentially involves three main steps: (i) self-assembly of template and functional monomer molecules through covalent or non-covalent bonds, (ii) polymerization of template-monomer complex with cross-linking monomers and (iii) template removal to unveil a binding cavity that is specific to the imprint molecule [1]. This study will implement self assembly, a non-covalent method for polymerisation of the MIP layer. An immunosensor may seem like an attractive alternative to an MIP-based sensor but, biomolecules used in immunosensors are highly unstable (chemically and physically) which prevents their use in harsh environments. There are several advantages of MIPs: they are physically and chemically stable, hence, can be stored for a long period of time in dry state at room temperature. They are low cost, easily reproducible and require simple preparation compared to their biological counterparts.

MIPs have been widely researched and well established in detection of human viral pathogens. MIPs are also known to detect Hepatitis A virus using resonance light scattering (RLS) as a sensing platform [3]. Electrochemiluminescence in combination with functional nanoparticles provide binding sites located on imprinted surfaces for fast recognition of the HIV virus [1]. Molecularly imprinted polymers have been used for molecular binding and screening of the influenza virus H5N1 [31]. Influenza, commonly known as the seasonal flu, is a viral infection that attacks the respiratory system. Wangchareansak et al, combined MIPs with quartz crystal microbalance (QCM) to screen the various influenza virus subtypes H5N1, H5N3, H1N1, H1N3 and H6N1 [1]. QCM transducer allows for fast signal recognition and increased sensitivity of detection. MIP layers were created for each virus subtype which reportedly showed great recognition properties to the original virus template and were offered as molecular fingerprints. Not only does the study provide a way to identify inhibitors, antibodies and substrates that reduce the functionality of the virus through a conformational change, it also allows for an alternative rapid diagnostic for influenza virus A subtypes in unknown samples with detection limits as low as 105 particles/mL [31].

Furthermore, MIPs are a popular way to detect the dengue virus. Dengue virus is a single stranded positive RNA based virus that is about 100nm in size. Recently, Arshad et al. have developed an impedimetric sensor for the early detection of dengue virus. The sensor composed of screen-printed carbon electrodes (SPCE) modified with electrospun nanofibers of polysulfone and coated with dopamine while using NS1 (non-structural protein 1—a specific and sensitive biomarker for dengue virus infection) as template during polymerization [2]. Cyclic voltammetry (CV) measurements were taken to measure the electrochemical properties of MIP modified

electrodes. The impedimetric sensor showed selective detection of NS1 concentrations with a detection limit as low as 0.3ng/mL [2]. MIP based detection has been widely used in literature in the detection of human viral and has shown 90% accuracy. Not only are MIPs a promising technology in the aqueous environment, they also show potential for detection of substances in the gas phase (exhaled breath). Emam et al, conducted a study which detects butylated hydroxytoluene (BTH) (volatile organic compound in the breath) within 60s in gas using a molecularly imprinted graphene based electrochemical sensor [27]. The binding of BTH to the MIP layer displays an increase in resistance change caused by an electron transfer to the graphene layer which can be measured within 30-35 seconds. MIPs are valuable technology that can also detect molecules in the air. The critical literature review forms the basis of the technology used in the breathalyzer-like device that will allow for viral detection in the breath.

The breathalyzer-like device that is proposed in this paper will be consist of an MIP layer on a graphene sheet which in turn will be immobilized onto a carbon electrode. (See figures 3 and 4) The electrode will be attached to an electronic sensor that will detect a

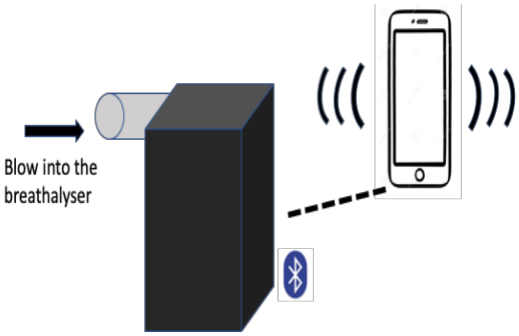


resistance change upon binding of the spike protein, this resistance change will be measured through an electrochemical detection method. The composition of the device and its working principle are described in more detail in the next section.

## III. METHODS

The breathalyzer-like device will detect SARS-CoV-2 by the binding of molecularly imprinted polymers (MIPs) to the virus's spike protein. The MIPs will be synthesized through polymerisation of functional monomers around a template of the spike protein via noncovalent interactions [19]. The spike protein will then be extracted, resulting in a porous polymeric network with binding cavities fitting the size, shape and functionalities of the spike protein. [22] The nature of MIPs allows the cavities to be changed based on what is needed to be detected, therefore allowing future changes to the MIPs depending on what the user wants to test for.

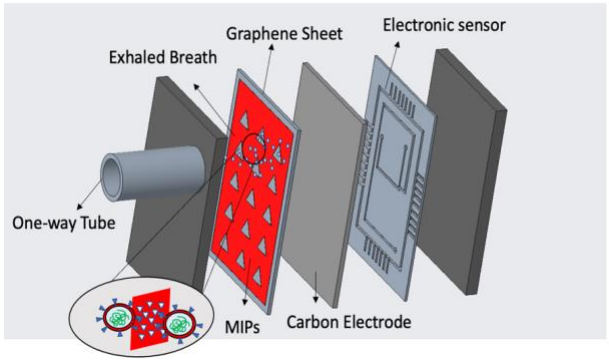


***Figure 3:*** *Device Composition*

To use this device, a person would blow into a tube that collects their exhaled particles. Within the device, there would be a graphene sheet connected to a MIP layer. Graphene has a high electronic conductivity and high carrier mobility, which increases the sensitivity of the device. The graphene sheet will be immobilized on a glassy carbon electrode which will connect to an electronic sensor to detect resistance change. When the target molecule (viral S protein) is trapped in the MIP layer, an extra electron is transferred to the graphene layer, which causes a measurable resistance increase within 30-35 seconds, bringing an extremely fast result rate. This increase in resistance will show a positive result for SARS-CoV-2. The electronic sensor will consist of a transducer which will change the physical resistance change to a detectable electrical signal, similar to an ohmmeter. The electrical signal will be detected using an electrochemical detection method and the results will be directly linked to the smartphone of the user via bluetooth.

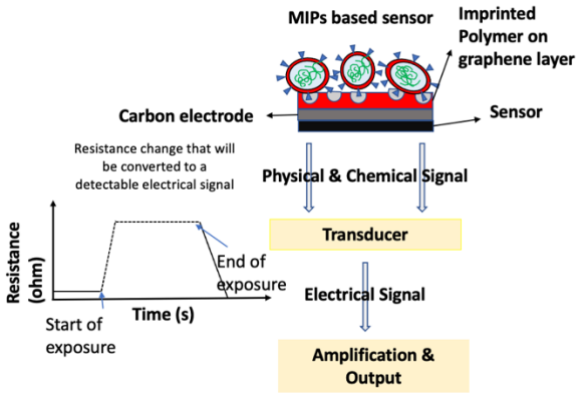


***Figure 4:*** *The working principle behind the breathalyzer-device for COVID-19*

A breathalyzer-like test provides an extremely easy and user-friendly method of monitoring the COVID-19 virus. This device can be accessible to the public through various ways, some of the sectors which will result in in airports for instant detection of a COVID patient, it can be used by college students as a method to check Since the MIPs are similar to molds, after being removed of prior particle bounds, the breathalyzer can be reused for regular testing of individuals. The device does not require any training or a testing facility to obtain results, allowing for the general public to test themselves without prior research knowledge. In order to test the device, green fluorescent protein is going to be used to test the affinity of the MIPs to detect the protein. With this data, we can conclude whether or not the spike protein will be able to be detected through the use of MIPs in the same fashion.

***Conclusion***

This paper clearly identifies the urgency of a rapid test with a high level of sensitivity and accuracy. There are already a vast number of rapid tests that exist which are efficient and cost effective but the breathalyzer device will be much more desirable as it will be patient friendly in terms of price, comfort and the accuracy of results in just a few seconds. The tests can be widely accessible and can help potential consumers in the transport sector, such as airports, bus stops and even students in school or university campuses. There will be no prior experience needed to use this device and it will be reusable. It will allow for rapid detection and close monitoring of the virus in areas of high transmissibility. With new coronavirus variants increasing day by day, it has become important for any test to be highly sensitive and adaptable. One of the advantages of using MIPs is that they can be easily molded according to the template of the molecule we want to detect. If new variants of the coronavirus require us to detect any molecule other than the spike protein, we will be able to create an MIP layer for that particular molecule in a similar fashion outlined in this paper. Future research studies can pave way for detection of the different variants of the virus through a single device with the incorporation of different MIP layers. MIPs are diverse molecules that present a promising technology. Their application to the coronavirus can help in the development of cutting-edge medical devices or tests that allow for rapid detection of virus.

***Acknowledgements***

We would like to thank Dr. Oscar Juarez, and members of the Juarez lab, Dr. Karina Tuz, Ming Yuan, Ana Redondo for help in experimentation. In addition, we would also like to acknowledge the support from Shahila Mehboob Christie, Maryam Saleh and the members of the Kaplan Institute.

**References**

1. A. Malik et al., Molecularly imprinted polymer for human viral pathogen detection, Materials Science and Engineering C (2017), http://dx.doi.org/10.1016/j.msec.2017.03.209
2. Arshad, R., Rhouati, A., Hayat, A. et al. MIP-Based Impedimetric Sensor for Detecting Dengue Fever Biomarker. Appl Biochem Biotechnol 191, 1384–1394 (2020). https://doi.org/10.1007/s12010-020-03285-y
3. Abbott, on defense, details embattled rapid COVID-19 test results. MedTech Dive. Accessed March 20, 2021. https://www.medtechdive.com/news/abbott-on-defense-id-now-coronavirus-test-postmarket-study/586579/
4. Birnbaumer, Gerald & Lieberzeit, Peter & Schirhagl, R. & Milnera, Marcus & Dickert, Franz & Bailey, Andrew & Peter, Ertl. (2009). Detection of viruses with molecularly imprinted polymers integrated on a microfluidic biochip using contact-less dielectric microsensors. Lab on a chip. 9. 3549-56. 10.1039/b914738a.
5. Caishuang Liang, Huan Wang, Kui He, Chunyan Chen, Xiaoming Chen, Hang Gong, Changqun Cai, A virus-MIPs fluorescent sensor based on FRET for highly sensitive detection of JEV,Talanta, Volume 160, 2016, Pages 360-366, ISSN 0039-9140, https://doi.org/10.1016/j.talanta.2016.06.010.
6. CDC study says Abbott's rapid COVID-19 antigen test may miss two-thirds of asymptomatic cases. FierceBiotech. Accessed March 20, 2021. https://www.fiercebiotech.com/medtech/cdc-study-says-abbott-s-rapid-covid-19-antigen-test-may-miss-two-thirds-asymptomatic-cases
7. Cue COVID-19 Test - Instructions for Use.pdf. Accessed March 20, 2021. https://www.fda.gov/media/138826/download
8. Cui, Feiyun et al. "Molecularly Imprinted Polymers and Surface Imprinted Polymers Based Electrochemical Biosensor for Infectious Diseases." *Sensors (Basel, Switzerland)* vol. 20,4 996. 13 Feb. 2020, doi:10.3390/s20040996
9. Donato LJ, Trivedi VA, Stransky AM, et al. Evaluation of the Cue Health point-of-care COVID-19 (SARS-CoV-2 nucleic acid amplification) test at a community drive through collection center. Diagn Microbiol Infect Dis.

2021;100(1):115307doi:10.1016/j.diagmicrobio.2020.115307
10. download.pdf. Accessed March 20, 2021. https://www.fda.gov/media/143808/download
11. download.pdf. Accessed March 20, 2021. https://www.fda.gov/media/144747/download
12. download.pdf. Accessed March 20, 2021. https://www.fda.gov/media/141570/download
13. Ellume's COVID-19 Home Test shows 96% accuracy in multi-site US clinical study. Ellume. Published December 9, 2020. Accessed March 20, 2021. https://www.ellumehealth.com/2020/12/10/ellumes-covid-19-home-test-shows-96-accuracy-in-multi-site-us-clinical-study/
14. Florindo, H.F., Kleiner, R., Vaskovich-Koubi, D. *et al.* Immune-mediated approaches against COVID-19. *Nat. Nanotechnol.* **15,** 630–645 (2020). https://doi.org/10.1038/s41565-020-0732-3
15. Hu, B., Guo, H., Zhou, P., & Shi, Z. (2020, October 06). Characteristics of sars-cov-2 and covid-19. Retrieved March 21, 2021, from https://www.nature.com/articles/s41579-020-00459-7
16. Lu, R., Zhao, X., Li, J., Niu, P., Yang, B., Wu, H., . . . Tan, W. (2020, January 30). Genomic characterisation and epidemiology of 2019 Novel CORONAVIRUS: Implications for VIRUS origins and receptor binding. Retrieved March 21, 2021, from https://www.sciencedirect.com/science/article/abs/pii/S0140673620302518
17. Lucira™ is developing a single use, disposable COVID-19 test that provides results in just 30 minutes. In: Lucira Health. https://www.lucirahealth.com/. Accessed 21 Mar 2021
18. McBride, R., van Zyl, M., & Fielding, B. C. (2014). The coronavirus nucleocapsid is a multifunctional protein. *Viruses*, *6*(8), 2991–3018. https://doi.org/10.3390/v6082991
19. Ortensia Ilaria Parisi, Marco Dattilo, Francesco Patitucci, Rocco Malivindi, Vincenzo Pezzi, Ida Perrotts, Mariarosa Ruffo, Fabio Amone, Francesco Puoci "Monoclonal-type" plastic antibody for SARS-CoV-2 based on Molecularly Imprinted Polymers bioRxiv 2020.05.28.120709; doi: https://doi.org/10.1101/2020.05.28.120709
20. Plapp, F. (2020, September 28). The covid-19 pandemic: A summary. Retrieved March 21, 2021, from https://thepathologist.com/subspecialties/the-covid-19-pandemic-a-summary
21. Prince-Guerra JL (2021) Evaluation of Abbott BinaxNOW Rapid Antigen Test for SARS-CoV-2 Infection at Two Community-Based Testing Sites — Pima County, Arizona, November 3–17, 2020. MMWR Morb Mortal Wkly Rep 70:. https://doi.org/10.15585/mmwr.mm7003e3
22. Puoci , Francesco. *"Monoclonal-Type" Plastic Antibodies for COVID-19 treatment: What is the idea?"* www.mdpi.com/2079-4983/11/2/43/pdf.
23. Rahimi, A., Mirzazadeh, A., & Tavakolpour, S. (2020, September 30). Genetics and genomics of sars-cov-2: A review of the literature with the special focus on genetic diversity and sars-cov-2 genome detection. Retrieved March 21, 2021, from https://www.sciencedirect.com/science/article/abs/pii/S0888754320308764
24. Rapid COVID Tests: More Important Than Ever. Abbott. Accessed March 20, 2021. https://www.abbott.com/corpnewsroom/strategy-and-strength/rapid-COVID-tests-important-tool-for-recovery.html
25. SA. Lauer, K., JL. Hadler, K., GA. Noppert, Z., HE. Maier, R., K. Lin, D., E. Conticini, B., . . . AS. Abdulamir, R. (1970, January 01). Risk factors associated with mortality of COVID-19 IN 3125 counties of the United States. Retrieved March 21, 2021, from https://idpjournal.biomedcentral.com/articles/10.1186/s40249-020-00786-0
26. Schoeman, D., Fielding, B.C. Coronavirus envelope protein: current knowledge. *Virol J* 16, 69 (2019). https://doi.org/10.1186/s12985-019-1182-0
27. Shadi Emam, Adedokun Adedoyin, Xiaohua Geng, Mohsen Zaeimbashi, Jason Adams, Adam Ekenseair, Elizabeth Podlaha-Murphy, Nian Xiang Sun, "A Molecularly Imprinted Electrochemical Gas Sensor to Sense Butylated Hydroxytoluene in Air", *Journal of Sensors*, vol. 2018, Article ID 3437149, 9 pages, 2018. https://doi.org/10.1155/2018/3437149
28. Texas A&M System, Worlds Inc. Collaborate On COVID-19 Breathalyzer https://today.tamu.edu/2020/11/19/texas-am-system-worlds-inc-collaborate-on-covid-19-breathalyzer/ (accessed Apr 11, 2021)
29. What's The Difference Between COVID-19 Rapid and PCR Tests? Memorial Healthcare. Published November 9, 2020. Accessed March 20, 2021. https://www.memorialhealthcare.org/whats-the-difference-between-covid-19-rapid-and-c-tests/
30. Wangchareansak, Thipvaree & Thitithanyanont, Arunee & Chuakheaw, Daungmanee & Gleeson, M. & Lieberzeit, Peter & Sangma, Chak. (2014). A novel approach to identify molecular binding to the influenza virus H5N1: Screening using molecularly imprinted polymers (MIPs). MedChemComm. 5. 617. 10.1039/c3md00272a.

31. Yang B, Gong H, Chen C, Chen X, Cai C. A virus resonance light scattering sensor based on mussel-inspired molecularly imprinted polymers for high sensitive and high selective detection of Hepatitis A Virus. Biosens Bioelectron. 2017 Jan 15;87:679-685. doi: 10.1016/j.bios.2016.08.087. Epub 2016 Aug 27. PMID: 27631682.
32. Covid 19 https://www.scentech-medical.com/covid-19 (accessed Apr 11, 2021)
33. T.O.I. staff. Instant COVID-19 breath test as precise as swab test, Israeli company says https://www.timesofisrael.com/instant-covid-19-breath-test-as-precise-as-swab-test-israeli-company-says/ (accessed Apr 11, 2021)

# Predictive Modeling for Early Hyperglycemia Detection in Type 2 Diabetes

Pulkita Jain [*,1], Dr. Mudassir Rashid [*,2]

[*]Department of Chemical and Biological Engineering, Illinois Institute of Technology, Chicago, IL 60616, USA

## I.ABSTRACT

Type 2 Diabetes (T2D) is characterized by a combination of defects in insulin action and impairment in insulin secretion. Deficient insulin action causes people with Type 2 Diabetes to have difficulty controlling their blood glucose concentration (BGC) and experience periods of high (hyperglycemia) and low (hypoglycemia) BGC. Continuous glucose monitoring (CGM) sensors and machine learning algorithms can automate the process of meal size estimation, improve the accuracy of the carbohydrate estimations, and reduce the involvement of the subject. The aim of this project was to use dynamic Partial Least Squares (PLS) regression to model blood glucose data from CGM devices and optimize the model parameters for best generalized performance across all subjects. The mean square error for the modelled data was obtained to determine the accuracy of the predictive modelling. The parameters were optimized by explicit enumeration and grid search approach to minimize the mean square error (MSE), and the lowest MSE was obtained with the number of latent variables as 5 and past horizon as 5 (25 minutes). Future research will develop the logic inference using the first- and second-order derivatives of the prediction curve that will sound the alarms based on the predictions made in the current work.

## II.INTRODUCTION

### 2.1 Diabetes

Type 2 diabetes (T2D) is a heterogeneous disease with a significant degree of interpersonal variability that affects an estimated 34 million Americans [4]. T2D is characterized by an increase in resistance to insulin, a decrease in insulin production and secretion, or some combination of these factors. This causes individuals with T2D to have difficulty controlling their blood glucose concentration (BGC) and experience periods of high (hyperglycemia) and low (hypoglycemia) BGC[4]. Ingesting food leads to an increase in blood glucose levels which the body processes signaling the pancreas to release insulin which simulates the adipose and muscle cells to absorb the glucose from the bloodstream. Essentially this is how the body regulates the glucose levels. There are other hormones like glucagon involved too, however, this paper will focus on the levels of insulin as the main factor. In T2D, as the body produces less insulin, less glucose is absorbed from the bloodstream leading to an overall increase in glucose levels which is termed as hyperglycemia [8]. Hyperglycemia can also occur when the body starts to resist the insulin produced which leads to high glucose levels. T2D is a chronic condition with no cure which demonstrates the responsibility of the patient to manage their own blood glucose levels. This can be done using continuous glucose monitoring sensors (CGM). Prolonged hyperglycemia can lead to chronic and severe health conditions over time such as heart and blood diseases, kidney failures, nerve damage in limbs and so on [9].

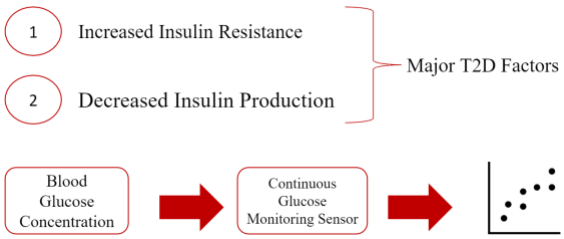


Figure 1: flowchart shows that the CGM sensor detects the blood glucose concentration and produces data points.

### 2.2 CGM Sensors (what are they?)

Blood Glucose monitoring has been revolutionized by the development of Continuous Glucose Monitoring (CGM) sensors [2]. These are wearable minimally-invasive devices that measure glucose concentration almost continuously (1–5 min sampling period) for several consecutive days/weeks. The first wearable CGM sensor prototype was introduced in 1999 and, since then, devices have evolved rapidly [2]. CGM readings may be sent to a phone with a sampling time

of 5 minutes and accessed through phone applications. While more popular for individuals with T1D, CGM sensors provide valuable, real-time insight into T2D blood glucose dynamics. CGM sensors have greatly improved and are now able to incorporate filtering to provide a more accurate measurement [10]. These devices now incorporate several features such as the ability to make decisions regarding the amount of food eaten to balance hypoglycemia or the physical exercise done to balance hyperglycemia. CGM sensors can monitor the blood glucose data in the real time and general alerts for hypo/hyperglycemia, however they do not have the ability to make or analyze the future predictions for BGC.

2.3 Predictive Modeling in Diabetes (several citations)

Early hyperglycemia warning systems based on continuous glucose monitoring (CGM) sensors may provide a convenient solution for monitoring and reducing the severity of hyperglycemia episodes. Hyperglycemia prediction is an estimation of when a person's blood glucose concentration (BGC) will rise above a certain threshold soon. Typically, the threshold for hyperglycemia is considered 180 mg/dL and this value was initially used in this study. However, many people with Type 2 diabetes (T2D) may have a higher fasting BGC which would cause small amounts of carbohydrate consumption to push the person into hyperglycemia. Continuous glucose monitoring sensors and machine learning algorithms can automate the process of meal size estimation, improve the accuracy of the carbohydrate estimations, and reduce the involvement of the patient.

In figure 2, real time glucose data obtained from CGM sensors was graphed along with the threshold limit of hyperglycemia. The patients experience varied highs and lows during the 1500 minute sampling time. This depicts the need of predictive modelling in diabetes. Predictive modelling will be able to make accurate predictions about someone's glucose level which can then be utilized by the patient to control their glucose levels more effectively before they ever reach the threshold.

System identification refers to the process of finding a mathematical model that describes a set of input-output data [7]. In this paper, the input data are past and current BGC measurements and the output data are the future BGC measurements. Identifying a model from this data therefore produces a predictive model that can be used to forecast future blood glucose values. The mathematical model of PLS Regression was utilized for this purpose [6]. Other mathematical models such as autoregressive-moving-average (ARMA) or Logistic Multiple Regression can also be used however, PLS was found to be the most effective and hence chosen as the predictive model.

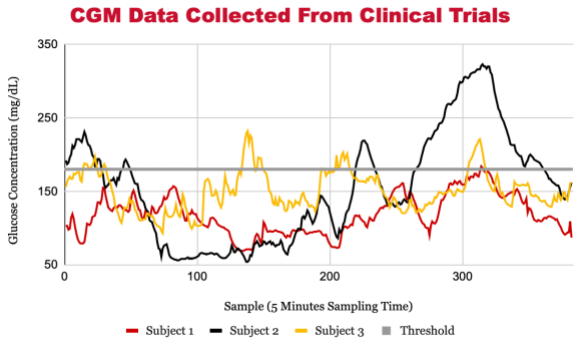


Figure 2: Real time data from 3 patients and the threshold limit of hyperglycemia at 180 mg/dL

## III.METHODS

### 3.1 Data Used

The data set for this project was the real-time data obtained from 135 patients. It was cleaned and filtered to reduce noise and rectify missing measurements. The data was then modelled using PLS Regression technique. The MATLAB Statistics and Machine Learning toolbox software was used for this research project.

### 3.2 PLS Regression

3.2.1 What is PLS?

Partial least squares (PLS) regression allows for the coefficients for all outputs to be estimated simultaneously by projecting the input regressor data, X, and the output response or predictions, Y, onto orthogonal subspaces of A-pairs of latent variables[1]. Each pair of latent variables accounts for a certain percentage of the variance in the input regressor data and output response matrices. Mathematically, PLS regression consists of decomposing X and Y as the sum of the outer products of a score and loading vector as follows:

$$X = \sum_{a=1}^{A} t_a p_a^T + E = TP^T + E$$

$$Y = \sum_{a=1}^{A} u_a q_a^T + F = UQ^T + F$$

where $t_a$ and $u_a$ are the input and output scores representing the projections of the variables in $X$ and $Y$ on their subspaces, $t_a$ and $u_a$ define the orientation of the corresponding subspaces, the matrices,$T$, $P$, $U$, and $Q$ contain their corresponding vectors, and $E$ and $F$ denotes residual matrices for the input regressor and

output response data matrices. The noise reduction property of PLS regression stems from the idea that the fewer latent variables are typically a consequence of measurement noise and system irregularities and therefore can be discarded during the PLS regression algorithm.

Since the PLS algorithm is used to obtain a mathematical relationship between the original data matrices, the input regressor and output response matrices are related through an inner relation between the corresponding scores as follows:

$$u_a = b_a t_a + e_a \, , for \; a \in [1, A]$$

where $b_a$ are the coefficients and $e_a$ are the residuals of the inner relationship between the scores of X and Y [5]. In this work, the PLS regression parameters are computed using the nonlinear iterative partial least squares (NIPALS) algorithm where the subspace orientation and scores for both the regressor input and output response matrices are determined simultaneously to maximize the covariance between X and Y and obtain the optimal fit for the inner relationship.

In this work, dynamic PLS is used to model the time-varying correlations and lags between the past CGM data and the future CGM data to be predicted. Dynamic PLS is a powerful multivariate algorithm that builds efficient models for predicting the future values by maximizing the covariance between the past and future data.

PLS relates regressor and regressed variables by maximizing the covariances between them [3]. PLS builds linear relations between input data and output data and uses these relations to predict future values. PLS has latent variables that describe the important underlying features of the data.

3.2.2 Glucose Modelling Methodology

A hyperglycemia prediction algorithm based on PLS regression and qualitative trend analysis has been developed. A matrix of past CGM data is used to handle the CGM time series, and the data are split into training and testing data. The training set is used to identify the model parameters and algorithm hyperparameters before evaluating the prediction algorithm on the independent testing set. Usually, 80% of the dataset is designated for training and 20% is designated for testing so this allocation was used. The training set was normalized by calculating the Zscores for the data and then fitting the PLS model to it. Once the model was fit, mean square error was calculated to determine the prediction accuracy. Next, the testing data set was used with the now fit PLS model and the mean square error was calculated. The three important variables used in this project were that of past horizon, latent variables and future horizons. Latent variables are crucial to the PLS model and help find better relations to perform a better regression. Past horizons are the set of previous data points that are needed by the program to determine accurate predictions values. Future horizon is defined as how far ahead into the future are the predictions being made. A sample time of 5 minutes was set so the past horizon of 1 implied 5 minutes in real time. The program was developed to run with a range of past horizon and latent variables values so these two important parameters could be optimized. The PLS model was then run for 135 patients using the optimized parameters and for different future horizons and the results were tabulated.

## IV.RESULTS

The following results were obtained when the PLS model was fit to the training and the testing data. The mean square error obtained for the training set and the testing set is in the table below. As it can be seen, the model (red) in the graph fits the actual glucose data really well. It shows that PLS is a great mathematical model to use for this type of predictive modelling. The testing data also worked really well with a very low mean square error for 15 minute ahead predictions.

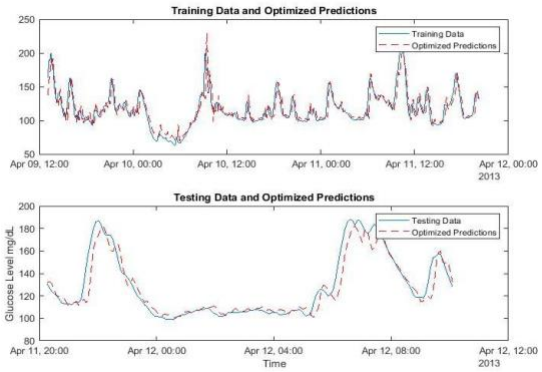


Figure 4: The top graph shows the training data in blue with its predictions in red. The bottom graph shows the testing data in blue with its predictions in red.

Table 1: The parameters for figure 3 and figure 4

| Figure | Past Horizon | Latent Variable | Future Horizon | Mean square error |
|---|---|---|---|---|
| 3 (Training) | 25 mins | 5 | 15 minutes | 4.5698 |
| 4 (Testing) | 25 mins | 5 | 15 minutes | 6.9832 |

The next logical step was to verify the accuracy of the model for different future horizons. Three different future horizons of 15 minutes, 30 minutes and 45 minutes were picked for this case and the results were plotted for such. The figure below shows these graphs, and it can be seen from the figure that the mathematical model works really well for 15 minute ahead

predictions. The predictions are fairly accurate for 30 minute ahead predictions, however the mean square error increases when moved on to the 45 minute ahead prediction horizon. This shows that the further into the future, the model tries to predict, the less accurate it becomes.

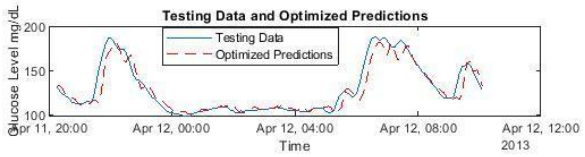


Figure 5: The graph shows optimized predictions for 15 minutes ahead into the future.

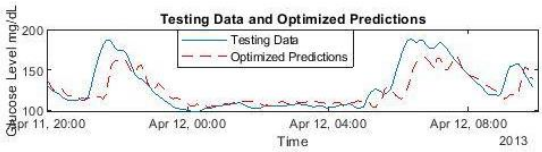


Figure 6: The graph shows optimized predictions for 30 minutes ahead into the future.

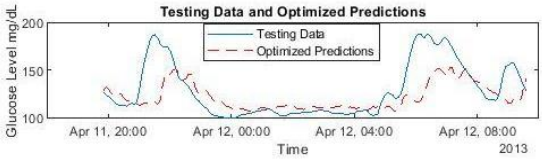


Figure 7: The graph shows optimized predictions for 45 minutes ahead into the future.

Table 2: Parameters for figure 5,6,7 and the associated mean square errors

| Figure | Past Horizon | Future Horizon | MSE obtained |
|---|---|---|---|
| 5 | 25 mins | 15 mins | 9.3946 |
| 6 | | 30 mins | 18.0048 |
| 7 | 25 mins | 45 mins | 23.6090 |

Once the training and the testing data were modelled accurately and the results were satisfying, the next step was to optimize the user defined parameters of latent variable and past horizon. It is necessary to obtain these parameters since there is no set number available for this in the literature and it is crucial that the number of past data points being used is the same for each subject. Moreover, the lowest MSE obtained due to these optimized parameters makes the PLS model fit the data better. These parameters were optimized by explicit enumeration and grid search approach to minimize the mean square error (MSE).

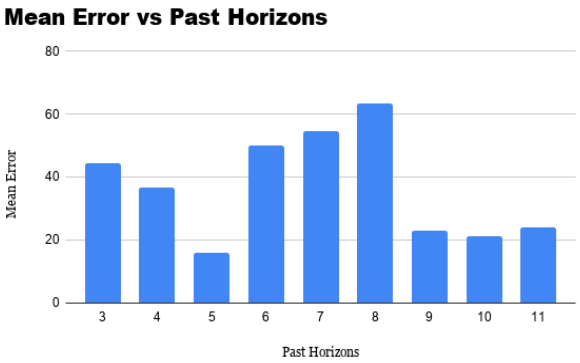


Figure 8: Mean Population Prediction Error vs Past Horizons.

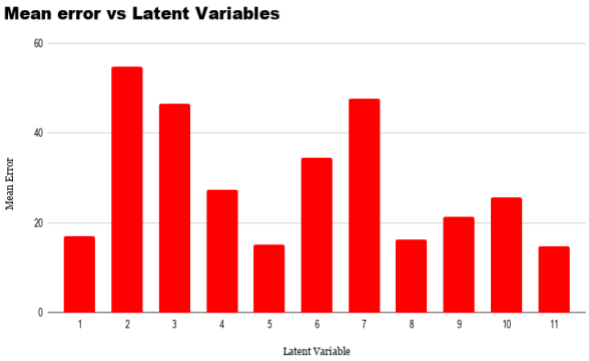


Figure 9: Mean Population Prediction Error vs Number of PLS Latent Variables.

The number of variables used was selected based on the number of prior data points used and the lowest error value. From the figures above, it can be seen that latent variables of 5 and past horizon of 5 (25 minutes ahead) give the lowest MSE for 135 subjects. Hence, these optimized parameters were selected and every figure in this paper has been created using these optimized parameters.

## V.DISCUSSION

These findings suggest that the PLS model fits the real-time data well and demonstrates the associated errors with optimized parameters of past horizon and number of latent variables that will be used in the future research to develop this model further. Being able to make accurate predictions of blood glucose concentration enables the patient to further be able to manage their blood glucose levels well. The major significance of these findings can be utilized for future research work in developing an alarm system where the

sensor can accurately predict the glucose levels and based on that sound an alarm if the patient will cross the hyperglycemia threshold limit in the future. By predicting accurately further into the future, proactive early warnings will be provided to the user on impending hyperglycemia events. Using the optimized parameters was successful since it helped eliminate large sources of error.

The data was obtained from 135 T2D patients, however, the demographics were not factored in, into this study. A good idea would be to include different types of parameters such as age, sex and other demographic information about the pateint to better see where the model can perhaps breakdown.

Future research will focus on developing the logic inference that will sound the alarms based on the predictions made in the current work. The logic inference will be developed using the first- and the second-order derivatives of the prediction curve. Qualitative trend analysis will also be utilized to help with the development of this alarm system. *Qualitative trend analysis* is used to extract information from time series data based on the overall behavior of the data. A polynomial is fit to a section of the data to provide a differentiable function. The first and second derivatives of this function are then found and evaluated. The sign of the derivatives after having been evaluated at a specific point then provides information about the data. The first derivative (dx) describes the direction and magnitude of the change in the data (i.e. the velocity) and can quantify whether it is increasing or decreasing in value. The second derivative (ddx) describes the rate of change of the velocity (i.e. the acceleration) and whether the data is heading towards a maximum or minimum, and change is decelerating or accelerating in either direction. Qualitative trend analysis is useful for hyperglycemia detection because the overall trend of blood glucose concentration is relatively well known. Postprandial hyperglycemia follows a roughly parabolic arc based on the carbohydrate content of the meal and physical characteristics of the person. The trends outlined by qualitative trend analysis can then be used to provide insight above the future trajectory of the BGC in real time. Using this, CGM sensors and machine learning algorithms will be able to automate the process of meal size estimation, improve the accuracy of the carbohydrate estimations, and help regulate hyperglycemia in people with T2D.

## VI. CONCLUSION

Patients dealing with T2D regularly measure their blood glucose concentrations to live a healthy life. They do so by using the Continuous glucose monitoring sensor which records the BGC every 5 minutes and gives an estimate to the patient via digital applications. Current CGM sensors sound alarms when the hyperglycemia level has been crossed, however they cannot make predictions about such hyperglycemia events.

This research paper takes the data obtained from CGM sensors and fits a mathematical predictive model to it. Thus, the mathematical model of Partial Least Squares Regression was used to model the continuous blood glucose concentration data obtained from the CGM sensors. After fitting the model, the prediction values of the BGC were calculated. The mean square error for all the future predictions was also calculated as well as the optimal parameters of past horizon and the number of latent variables were determined. Using the optimized parameters, predictions of BGC were also calculated for different future horizons. The error associated with these predictions also gave an estimate on how well the model works for different past and future horizons. This research will certainly enable patients suffering from T2D to better manage their BGC since they will have longer periods of time of knowing whether or not they will suffer a hyperglycemia event.

## VII. ACKNOWLEDGEMENTS

Financial support for Pulkita Jain from the Program for Undergraduate Research Education (PURE) initiative of the Armour College of Engineering is gratefully acknowledged.

Contributions by Dr. Rashid and PhD candidate Andrew Shahidehpour are also gratefully acknowledged.

## VIII. REFERENCES

1. Abdi, Hervé. "Partial least square regression (PLS regression)." *Encyclopedia for research methods for the social sciences* 6.4 (2003): 792-795.

2. Cappon, G.; Acciaroli, G.; Vettoretti, M.; Facchinetti, A.; Sparacino, G. Wearable Continuous Glucose Monitoring Sensors: A Revolution in Diabetes Treatment. Electronics 2017, 6, 65. https://doi.org/10.3390/electronics6030065

3. Chai, T. and Draxler, R. R.: Root mean square error (RMSE) or mean absolute error (MAE)? – Arguments against avoiding RMSE in the literature, Geosci. Model Dev., 7, 1247–1250, https://doi.org/10.5194/gmd-7-1247-2014, 2014.

4. Defronzo - 2009 - From the triumvirate to the ominous octet A new paradigm for the treatment of type 2 diabetes mellitus

5. Geladi, Kowalski - 1986 - PARTIAL LEAST-SQUARES REGRESSION A TUTORIAL

6. Kaur, H. and Kumari, V. (2020), "Predictive modelling and analytics for diabetes using a machine

learning approach", *Applied Computing and Informatics*, Vol. ahead-of-print No. ahead-of-print. https://doi.org/10.1016/j.aci.2018.12.004

7. Muñoz, J. and Felicísimo, Á.M. (2004), Comparison of statistical methods commonly used in predictive modelling. Journal of Vegetation Science, 15: 285-292. https://doi.org/10.1111/j.1654-1103.2004.tb02263.x

8. Mellitus, Diabetes. "Diagnosis and classification of diabetes mellitus." *Diabetes care* 28.S37 (2005): S5-S10.

9. Paul Z Zimmet, Dianna J Magliano, William H Herman, Jonathan E Shaw, Diabetes: a 21st century challenge, The Lancet Diabetes & Endocrinology, Volume 2, Issue 1, 2014, Pages 56-64, ISSN 2213-8587, https://doi.org/10.1016/S2213-8587(13)70112-8. (https://www.sciencedirect.com/science/article/pii/S2213858713701128)

10. Sparacino, G.; Facchinetti, A.; Cobelli, C. "Smart" Continuous Glucose Monitoring Sensors: On-Line Signal Processing Issues. *Sensors* **2010**, *10*, 6751-6772. https://doi.org/10.3390/s100706751

# Assessing the Performance of Building Mechanical Systems in an Office Building

Urwa Irfan,[1a] Afshin Faramarzi,[1] Akram Syed Ali,[1] Christopher Riley,[1] Brianna Galvan,[1] Brent Stephens,[1] and Mohammad Heidarinejad[1b]

[1] *Department of Civil, Architectural, and Environmental Engineering, Illinois Institute of Technology, Chicago, IL 60616, USA*
[a]uirfan@hawk.iit.edu [b]muh182@iit.edu

## I. ABSTRACT

The purpose of this research is to evaluate the performance of building mechanical systems in an office. The mechanical systems include eleven variable air volume (VAV) units that provide outdoor air to the office spaces and induction units that provide heating and cooling to the office spaces. This study presents the data collection, sensor installation, and analyses of the ventilation, heating, and cooling provided to the spaces. Differential pressure transducers, temperature sensors, and heat flux sensors were installed on-site to monitor these systems at every one-minute and five-minute interval. The process of analyzing datasets from these sensors is automated and used to calculate ventilation, heating, and cooling under current building automation sequences of operation. The results of this study will aid our understanding of the impacts of different building mechanical systems, occupancy patterns, time of the day on the ventilation, heating, and cooling use for the selected building.

## II. INTRODUCTION

This study aims to develop a reliable method of evaluating and analyzing the mechanical systems of an office building. The space studied for this project is divided into eleven thermal zones. Each zone is served by a Variable Air Volume (VAV box) connected to a number of ceiling diffusers to provide for space conditioning and outdoor air requirements. In addition, induction units installed around the perimeter next to the windows around the South and West facades provide heating and cooling to the space.

## III. METHODS

The VAV differential pressure, temperature, and relative humidity are monitored using Onset data loggers and gateways. The differential pressure is monitored using Veris sensors connected to Onset MX 1104 data loggers fitted in custom-made boxes. The temperature and relative humidity for one ceiling diffuser connected to each VAV box are monitored using the same data loggers.
Ten Fluxteq heat flux sensors are currently in operation: six are installed inside induction units across three rooms, three are installed at windows across two rooms, and one is installed outside the cover of an induction unit.

## IV. ANALYSIS

The rate of heat transfer at windows or induction units is calculated by multiplying the measured area with the heat flux recorded by the Fluxteq sensors. The volumetric flow rate of the air in the VAV boxes, Q is calculated using data from the differential pressure sensors as follows:

$$V = 4005 \times \sqrt{dp} \quad (1)$$

$$Q = V \times A \quad (2)$$

where V = velocity of air, foot per minute (fpm)
dp = differential pressure, inches of water (in w.c.)
A = cross-sectional area of the VAV box, $ft^2$

The datasets collected for differential pressure, temperature, relative humidity, heat flux, and the calculated airflow and heating/cooling loads are plotted using Python scripts. Various types of graphs are used: scatter plots, heat maps, and box plots. As an example, the hourly rate of heat transfer at an induction unit in a private office room over a period of 26 days is shown in Figure 1. A negative value for heat transfer signifies cooling. The larger magnitude of heat transfer during the day illustrates the higher usage of the induction unit for space conditioning in those times; outside of working hours, the output at the induction unit changes little.

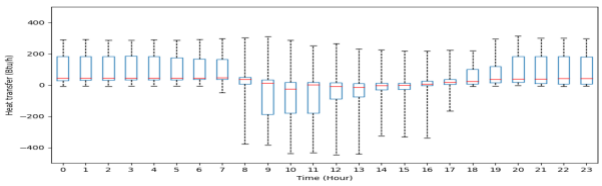

Figure 1: Hourly heat transfer at an induction unit

The temperature and relative humidity measured in one month at a diffuser connected to VAV box no. 10, which is

located in a lounge area, are represented in Figures 2, 3, and 4. The initial measurements do not fluctuate much as the space was unoccupied around this time. For the latter part, the hourly temperature in Figure 3 shows how the temperature of the air supplied to the space falls during the day when occupancy is highest, to accommodate for the greater heat gain due to occupants and equipment usage. Similarly, Figure 4 illustrates how the RH rises during occupied hours.

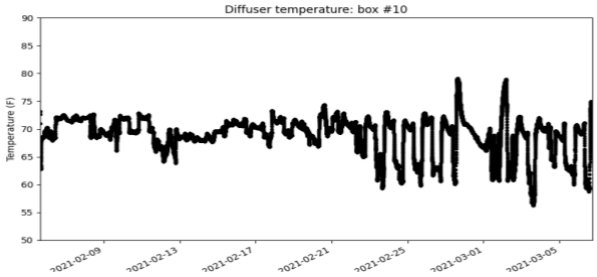


Figure 2: Diffuser temperature in a lounge area

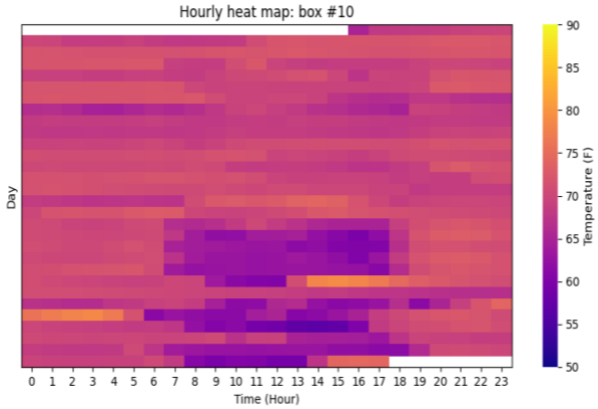


Figure 3: Hourly temperature of air supplied to a lounge area

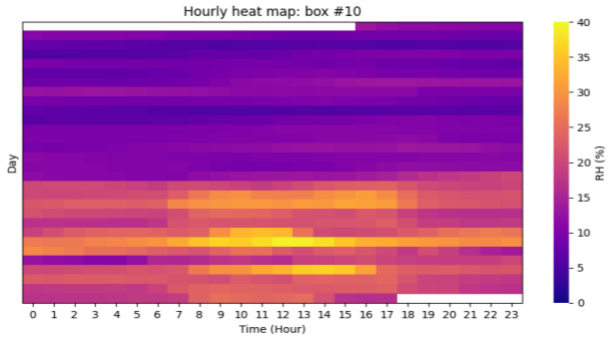


Figure 4: Hourly relative humidity of air supplied to a lounge area

## V. CONCLUSION

The preliminary data shows how factors such as occupancy and time of day influence space loads as well as airflow requirements. Greater occupancy increases the load and thus the facets of air supply; the variation in outside temperatures affects loads throughout the day, impacting heating and cooling device usage. Further analysis will yield a better understanding of the effect of such elements on the operation of building mechanical systems and can be used to monitor as well as improve on specific building facilities in the future.

# Intraoperative Assessment of Surgical Margins in Cancer Resection Surgery via the Sub-Diffuse Optical Tomography s-DOT

Sophia R. Nelson[a], Brooke C. Villinski[a], Allyson Trang[a], Jennifer M. Vorjohan[a], Cody Rounds[a], Max J.H. Witjes, MD, DDS, PhD[b], and Kenneth M. Tichauer, PhD[a]

[a]Illinois Institute of Technology 3255 S Dearborn St, Chicago IL, USA 60616
[b]Department of Oral and Maxillofacial Surgery, University of Groningen, 9712 CP Gronigen, The Netherlands

**ABSTRACT:**

**In Head and Neck Squamous Cell Carcinomas (HNSCC), positive margins after surgical resection dominate the clinical outcome of patients. Between 15-30 percent of all HNSCC surgeries result in a positive margin (>5 mm) that requires postoperative chemo-radiation, radiotherapy, and/or revision surgeries. To minimize local recurrence, margin assessment is typically performed through surgical pathology departments; however, this technique often takes more than 24 hours to process and only a small fraction of the total surgical margin is evaluated. A second, intraoperative approach used by surgeons to minimize local recurrence is frozen section analysis (FSA), which is time intensive and suffers heavily from sampling errors. To effect change, we have hypothesized a sub-diffuse optical tomography modality that can identify the differences in depth sensitivity of the fluorescence, Cetuximab-IRDye800CW conjugate (ICON), by the fluorescent photons collected from sub-diffused media as a function of the photon exit angle from the excited tissue. Based on promising preliminary simulations using Monte Carlo MATLAB, closed vs. open aperture fluorescence imaging in biological tissue demonstrated an enhanced true depth of fluorescence resolution up to 6 mm, well beyond the insufficient 5 mm mark. By identifying the deep margins from the fluorescent peaks within 5 minutes, we hope to improve complete oncological surgery by providing surgeons an exact region of interest on the specimen where the tumor is closest to the edge, so they may continue surgery on the spot to minimize the probability of cancer being left behind.**

Head and Neck Squamous Cell Carcinomas (HNSCC) make up 90 percent of all head and neck cancers, with over 600,000 new cases per year worldwide [1]. HNSCC originates in the areas of the lip/oral cavity, nasopharynx, oropharynx, hypopharynx, and the larynx with the main at risk population being long term smoking and alcohol users [1]. It is due to these intricate anatomical areas in which surgical resection is the primary curative treatment and, therefore, has the highest incomplete resection rates of all cancer types at 15-30 percent [7].

After surgical resection of the primary tumor, the margins are accurately assessed by post-operative pathology, which may take days to verify if the tumor has a margin of 5 mm of healthy tissue surrounding it. In the mean time, the patient is sewn up and sent home. Currently, the only intraoperative assessment of margins relies on frozen sectional analysis (FSA), which heavily suffers from sampling errors and is a time intensive technique that can last up to 30 minutes [3, 12]. It is for these reasons, that both FSA and pathology are undesirable tools due their subjective evaluation methods and the struggle for surgeons to identify suspicious regions that should be sent to histopathologic assessment. Additionally, the completeness of the surgery must also consider the quality of life the patient will face (e.g vital, functional, and cosmetic reconstruction). It is estimated that more than 15 percent of HNSCC patient have inadequate margins after being sent home from their operation [9]. Failing to intraoperatively recognize these positive margins results in a loco-regional recurrence that may necessitate additional therapy such as radiation, chemotherapy, and recurrent surgeries [4]. There is much debate regarding characterizing an inadequate margin, the current method of measurement for a positive close margin is cancer between 1 to 5 mm of the margin as shown in Figure 1 [4]. However, to evaluate these margins the resected tumor is divided into an epithelial/mucosal surface and a deep surface (surgical margin exposed after surgery), which account for approximately 90 percent of the inadequate margins because of the lack of visual feedback [12].

Mitigation of inadequate margins holds great importance to the outcome of the patient and their overall quality of life. Therefore, to address these challenges (with specific

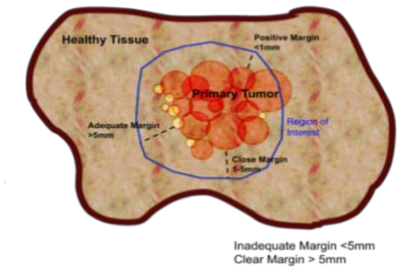


**Figure 1** The margins are highlighted in this image as close(1-5 mm), positive(<1 mm), and clear(>5 mm) from the amount of healthy tissue surrounding the tumor to the region of interest. To have adequate margins, clear margins need to be met, in which there should be 5mm of healthy tissue surrounding the tumors edge.

focus on deep margins) we have proposed a novel intraoperative margin assessment device termed, the Sub-diffused Optical Tomography (s-DOT), that will rapidly and accurately identify the positive (<1 mm) and close (1-5 mm) margins on whole resected specimens. To accompany the intraoperative s-DOT device, fluorescent labeled antibodies will be used to identify the closest surgical margin on the specimen by assessing the relative fluorescence intensity peaks. By promising results shown by Monte Carlo MATLAB simulations, we hope to improve the rates of incomplete surgery in real time to minimize the probability of leaving any cancer behind.

**Materials and Methods**

The augmented Monte Carlo software on MATLAB (MATLAB 2018b Student License) was used to model the simulation of light transport in HNSCC tissue by the general methods for fluorescence simulations and diffuse optical tomography (DOT). The Monte Carlo (MC) developed by Jacques et al [6] was utilized to mimic the light propagation in scattering tissue with homogeneous optical properties. Assuming Fresnel reflections at tissue/air interfaces, the code utilizes the size of the medium, the absorption coefficient of the medium set to $\mu_a$ 0.4 $cm^{-1}$ the scattering coefficient $\mu_s$ set to 125 $cm^{-1}$ and the anisotropy of scattering (g) set to 0.9 $cm^{-1}$ [6]. The anisotropy of scattering represents the probability distribution of scattering angles [1]. The refractive angle is then calculated between two regions within the tissue or at the surface have mismatch refractive indices [1]. To stimulate the fluorescence emission resulting in the fluorescence quantum yield, the MC parameters utilizes the probability of an absorbed photon packet and converts it to a fluorescent photon at a specific wavelength. The photon "packets" are photons in MC literature [11] defining the photons travel inside a tissue mode. It considers the initial weight as it enters the model and the transmission through or reflection across a boundary governed by Snell's law and Fresnel's equations [13].

Snell's Law : $n_1 \sin\theta_1 = n_2 \sin\theta_2$

After each step the photon packet weight is reduced according to the absorption probability [10] and this continues step by step until the photons exit the tissue or are completed absorbed. However, as this is transformed to fluorescence photons, the emission of this photon is now isotropic due to the nature of fluorescence [1].

To stimulate the fluorescence emission, the MC simulation allows for a simulation light propagation, where set at an excitation wavelength of 680 nm with respect to the fluorescence, will be discussed in the next section. A fluorescent photon will be generated per excitation. Then, the MC simulation is utilized to stimulate the emission wavelength from a tissue model related to the absorption and scattering properties of the HNSCC tissue model, in addition to the fluorescence quantum yield and lifetime. The path of the photon packet was recorded to a detected fractional density map of incident light transported $D(x_i,y_j,z_k)$ created by Dr. K.Tichauer and his team [11].

**Fluorescent Imaging Agent**

During all phases of functional testing, the s-DOT will be imaging Indocyanine Green (ICG) fluorescent dye (Tokyo Chemical Industry Co, Chuo City, Tokyo). Although the s-DOT will be imaging ICG fluorescence during the functionality tests, the fluorescent dye used during the s-DOT intraoperative application will be the Cetuximab-IRDye800CW conjugate (ICON) agent in collaboration with Dr. M. Witjes. The ICON agent has shown enhanced tumor to healthy tissue contrast due to the addition of fluorescent labeled antibodies specific to the endothelial growth factor receptors (EGFR), which are over expressed in 90 percent of HNSCC [5]. The use of the ICON agent will be very valuable in amplifying the tumor contrast during surgery. However, the ICG fluorescent imaging agent will be used for testing due to its lower cost and similar excitation and emission wavelengths to the ICON fluorescent agent. The ICON agent's excitation wavelength is 780 nm and its emission wavelength is 820 nm [2]. On the other hand, ICG dye's excitation wavelength is 775 nm and its emission wavelength is 796 nm [2]. Due to the similar excitation and emission wavelengths, ICG will be a suitable stand in for the ICON dye during the s-DOT functionality tests.

**Phantom Fabrication**

For the second phase of testing, optical phantoms were created from resin (Castin' Craft, Fields Landing, CA), titanium dioxide (DuPontTM Ti-PureR, DuPont Titanium Technologies, Wilmington, DE), India ink (Winsor & Newton, London), and dimethyl sulfoxide (DMSO) (Fisher

BioReagents, Thermo Fisher Scientific, Waltham, MA). India ink was used as the absorbing agent and titanium dioxide was used as the scattering agent. Various concentrations of India ink and titanium dioxide were created with DMSO as the solvent. The concentrations of each material that provide the optical properties of HNSCC tumors will be found by measuring the optical properties of the various sets of phantoms and comparing the results to the target values. The target optical properties of HNSCC tumors are, 125 $cm^{-1}$ as the scattering coefficient $\mu_s$, 0.4 $cm^{-1}$ as the absorption coefficient $\mu_a$, and 0.9 $cm^{-1}$ as the scattering anisotropy (g). Although the optimal concentrations of titanium dioxide and India ink have not been found yet, the optical property characterization experiment further explained are being done now to determine those concentrations.

After deciding the concentrations of India ink and titanium dioxide that best mimic the optical properties of HNSSC, silicone molds were created with pins at varying depths from 2 mm to 5 mm. These pins created holes at different depths for the ICG fluorescence to be loaded into the phantom and measured with the s-DOT device.

**Phantom Optical Property Characterization**

To characterize the optical properties of the resin, titanium dioxide, and India ink phantoms, 2 cm cubed phantoms and resin smears of the various concentrations were constructed. The resin smears were created to be 100 microns thin on a 12 well plate. To verify the thickness of the smear, the well's diameter was measured and the ideal volume of resin to be smeared on the bottom of the well was calculated to be 28.95 μL.

After creating the resin smear in the well plate and the cubed phantoms, an imaging system and photon counter system were used to characterize the phantom's optical property values. The imaging system measured the initial light ($I_0$), the distance (x), and the final light (I) for each resin smear sample. Then, use Beer Lambert's Law to calculate the total reflection of light ($\mu_T$).

$$I = I_0 * \exp(\mu_T x)$$

$$\mu_T = \mu_a + \mu_s$$

Due to the small thickness of the resin smear (100 microns), the diffusivity assumption can be used to assume that the light will only be scattered once while traveling through the resin smear.

Next, the absorption coefficient ($\mu_a$) and the reduced scattering coefficient ($\mu'_s$) are measured using a photon counter. The photon counter measures the amount of photons hitting the detector every 4 picoseconds. Then, a MATLAB code using Beer Lambert's Law and Green's Function was used to curve fit an equation measuring the optical properties to the number of photons vs time.

$$\phi(r,t) = \left[\frac{c}{(4\Pi Dct)^{3/2}}\right] \exp[-\frac{-r^2}{4Dct} - \mu_a ct]$$

**Equation 2** Green's Function

The resulting output optical properties will be the absorption coefficient ($\mu_a$), scattering coefficient ($\mu_s$), reduced scattering coefficient ($\mu'_s$) and the scattering anisotropy (g). Through testing various concentrations of titanium dioxide and India ink, the concentrations of these materials to mimic the absorption coefficient ($\mu_a$) of 0.4 $cm^{-1}$ the scattering coefficient ($\mu_s$) of 125 $cm^{-1}$ and the scattering anisotropy of 0.9 $cm^{-1}$ will be found.

**Device Testing**

After constructing the s-DOT, the device will undergo various phases of testing. The s-DOT will undergo three phases of functional testing involving multiple types of optical phantoms and live tissue. The three phases are as follows: testing with commercially manufactured phantoms, testing with phantoms created to mimic HNSCC tumors, and testing with live tissue.

In the first phase of testing, the s-DOT will be tested using commercially manufactured optical phantoms (INO Biomimic Optical Phantoms). A capillary tube filled with ICG dye will be placed at varying depths on six different phantoms. The tested depths will be from 0.1 mm to 5 mm in 0.5 mm increments. Each depth will be tested three times to ensure device precision.

In the second phase of testing, the s-DOT will be tested using the optical phantoms created from resin, titanium dioxide, and India ink. Four depths of a fluorescent marker, from 2 mm to 5 mm in 1 mm increments, will be tested with the system, with each depth tested three times. In addition to testing those four depths, the s-DOT will also run tests on phantoms with multiple fluorescent holes at differing depths to measure the device's sensitivity and accuracy to multiple signals.

Finally, in the third phase of testing, the s-DOT will be tested on live animal tissue stained with ICG fluorescent dye. The dye will be injected into the animals nasopharynx and oral cavity tissue at various depths and amounts. Each tissue will be imaged three times. For each phase of testing, the s-DOT results will be compared to the true depth value of the fluorescent marker and an analysis on the difference between the values will be done.

**Results**

MC MATLAB simulations are a way of creating ideal results of the s-DOT to develop the image processing and analysis to create the depth map results of the s-DOT. Two different simulations are run to model two images the s-DOT will produce. The first is an open-aperture image--an open field image, which is modeled by a beam that is an isotropically emitting point source. The second is a narrow-aperture image, modeled by a pencil beam. The ratio of the narrow aperture to the open aperture will provide a way of determining quantitative depth values from fluorescent imaging. Simulated results from the s-DOT are shown in Figure 2.

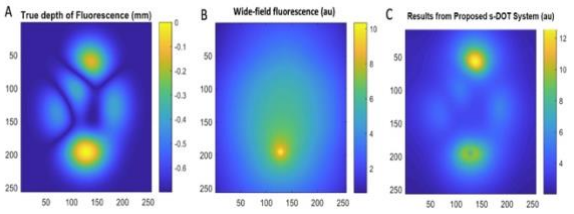


**Figure 2** Simulated demonstration of improvements possible with s-DOT for observing wider insufficient margins. A) Simulation "truth" of fluorescence at depth up to 5 mm (margins less than 5 mm wide are considered insufficient). B) Standard fluorescence imaging of the fluorescence as seen from the surface of the field of view defined by A. C) Image resulting from ratioing narrow and open aperture fluorescence images, which is the first component of s-DOT.}

The ratiometric approach of both apertures will counteract any effects from model data mismatch and the effects of any varying optical properties within the resected tissue. Therefore, the ratio value will be directly related to depth values, which can be provided to surgeons intraoperatively.

## Imaging Depth of Fluorescence

When looking at highly optically 3D scattering tissues, the depth of the fluorescence may be limited by the heterogeneity of optical properties and the shape of the tissue. To combat this MC Simulations showed that fluorescence wavelength ratioing can overcome tissue surfaces effects and mitigate sensitivity to optical properties in fluorescence tomography and spatial frequency-domain imaging.

The relationship between the depth that fluorescence is detected in a resected tissue and the ratiometric values of the open and close aperture values is currently being investigated. To display the relationship between the two, MC simulations were run on ellipsoid shaped resected tissues of varying depths. The ratio values were plotted against the depth values of various shape samples. For example, the ratio and depth scatter plot for the 5mm deep ellipsoid is shown in Figure 3, along with a best cure fit to the data.

In Figure 3, the blue dots represent the depth (x-axis, in cm) and ratio value (y-axis, in au) for all pixels in the aperture images simulated. The red line is the best fit curve for the data. Figure 4 shows the fit curves of the varying depth ellipsoids.

The results from Figure 4 clearly show there is a relationship between ratio values and depth values, and that this relationship is related but different for varying shapes of detected fluorescence. Future work will be conducted in limited angle tomography reconstruction along side the relationship between ratio and depth to produce depth margins via an interactive display for surgeons during surgery.

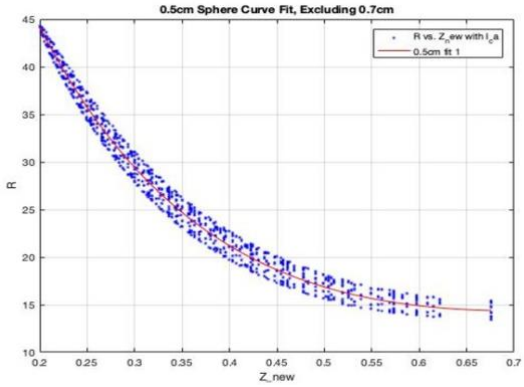


**Figure 3.** Scatterplot of Ratio vs Depth 5mm Sphere Sample.

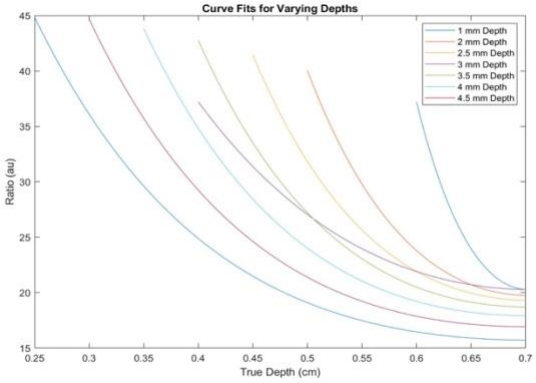


**Figure 4.** Fit Curves for Domes with Radii 1mm to 5 mm, in 0.5 mm increments.

## Discussion

The promising technology behind the s-DOT system will be favorable for hospitals to adopt, due to its superior depth sensitivity and its seamless transition into the workflow of oncologic surgical operations. The s-DOT presents a unique method that has not been utilized in other target fluorescent imaging modalities, in which the difference of

open and closed apertures presents an accurate depth sensitivity that can be
relayed to surgeons in real time for expedited and successful resections of whole tumors of HNSCC. The s-DOT also presents itself as an ex-vivo target imaging device, so it does not cause additional harm to the patient during surgery. The goal of the project is to improve the rate of complete cancer surgery to improve the identification of inadequate margins from positive (<1 mm) to close (1-5 mm) depths. Although the s-DOT cannot prevent the initial surgery needed for HNSCC patients yet, it has the capability to assist the surgeon in performing a less radical surgery for lower morbidity, and to go back in after identification of inadequate margins. This statement has been hypothesized from the current success of the MC MATLAB simulation results. The results suggest that the surgeon can identify inadequate margins with the s-DOT during the patient's initial surgery, thus decreasing the probability of a recurrent and detrimental HNSCC tumor. Overall, the use of the s-DOT during HNSCC surgeries will lead to a comfortable living style for the patients.

**Acknowledgments**
The research presented is being financially supported by the Illinois Institute of Technology Biomedical Engineering department, the Pritzker Institute of Biomedical Science and Engineering, and the National Science Foundation. Additionally, gratitude is expressed to Dr. Jennifer Kang-Mieler, Mr. Jeremy Alexis, and members of the The Head and Neck Cancer Alliance Foundation.

**References**
1. Caigang Zhu, Q. L. Review of Monte Carlo modeling of light transport in tissues. *Journal of Biomedical Optics* **18**, (2013).

2. Day, K. E. *et al.* Fluoresence-Guided Surgery. *Frontiers in Oncology* **7**, (20132017).

3 .Dik, E. A. *et al.* Resection of early oral squamous cell carcinoma with positive or close margins: Relevance of adjuvant treatment in relation to local recurrence: Margins of 3mm as safe as 5mm. *Oral Oncology* **50**, 611–615 (2014).

4. Eldeeb, H. The Effect of the Surgical Margins on the Outcome of Patients with Head and Neck Squamous Cell Carcinoma: Single Institution Experience. *Cancer Biology & Medicine* **9**, (2012).

5. J R Grandis, D. J. T. Elevated levels of transforming growth factor alpha and epidermal growth factor receptor messenger RNA are early markers of carcinogenesis in head and neck cancer. *Cancer Research* **53**, 3579–3584 (1993).

6. Jacques, S. L. A subroutine written in C language that can be called to run a Monte Carlo simulation.https://omlc.org/software/mc/mcsub/index.html.

7. Keulen, S. van. The Sentinel Margin: Intraoperative Ex Vivo Specimen Mapping Using Relative Fluorescence Intensity. *American Association for Cancer Research* **25**, (2019).

8. MD, S. M. Head and Neck Cancer: Changing Epidemiology, Diagnosis, and Treatment. https://doi.org/10.4065/83.4.489.

9. Orosco, R. K. Positive Surgical Margins in the 10 Most Common Solid Cancers. *Nature* **8**, (2018).

10. Philip, R., Penzkofer, A., Bäumler, W., Szeimies, R. M. & Abels, C. Absorption and fluorescence spectroscopic investigation of indocyanine green. *Journal of Photochemistry and Photobiology A: Chemistry* **96**, 137–148 (1996).

11. Sinha, L. *et al.* Comparison of time- and angular-domain scatter rejection in mesoscopic optical projection tomography: a simulation study. *Biomed. Opt. Express* **10**, 747–760 (2019).

12. Woolgar, J. A. & Triantafyllou, A. A histopathological appraisal of surgical margins in oral and oropharyngeal cancer resection specimens. *Oral Oncology* **41**, 1034–1043 (2005).
13. Fresnel equations.
https://en.wikipedia.org/wiki/Fresnel_equations.

# An agent-dependent enhanced optical projection tomography-guided system for lymph- node images reconstruction to optimize cancer detection

Hang Nguyen[*,1]

[*] Department of Biomedical Engineering, Illinois Institute of Technology, Chicago, IL 60616, USA

## I.ABSTRACT

The purpose of this work is to provide a system that regenerates images in a short amount of time while minimizing any existent noise in the model. An agent-dependent enhanced optical projection tomography-guided (ADEPT-GUI) system, utilized filtered back-projection (FBP), is created to perform the iterative reconstruction of lymph node images.

## II.INTRODUCTION

Cancer continues to be one of the leading causes of death worldwide. As of 2020, 1,806,590 new cancer cases and 606,520 cancer deaths are recorded in the United States1. As a result, it is critical to develop techniques/technologies to assist surgeons in making fast and accurate decisions of whether to do more removal of tumor-draining lymph nodes while operating cancer surgeries. The agent-dependent enhanced optical projection tomography (ADEPT) system is a technology combining advancements in two areas. First is the optical projection imaging. The second is the "paired-agent" molecular imaging2. These attained images are transferred to the ADEPT-GUI system subsequently to reconstruct images. Physicians can then quickly check the tumor-draining lymph nodes and conclude whether to continue the operation.

## III.METHODS

### 3.1 Filtered back-projection (FBP)

FBP is a common analytical reconstruction method that helps regenerate an object's image while decreasing embedded noises. The process is comprised of two parts, the filtered phase and the back-projection phase. Back-projection is the act of smearing different obtained 2D images at their taken angles. The images are then filtered to sharpen the results. Lastly, the sinogram will be inversed back through the built-in MATLAB iradon() function. The reconstruction operation is completed.

### 3.2 Maximum-likelihood expectation-maximization algorithm (MLEM)

MLEM is the algorithm frequently used in reconstructing images. Usually, there is an initial estimated image to start off the reconstruction. However, the computation is inherently slow. Therefore, our system has integrated FBP as the initial point of the MLEM technique to accelerate the reconstructing procedure. This combination enhances both the speed of the system and the quality of the images.

Figure 1: 3D reconstruction of a lymph node using the ADEPT system

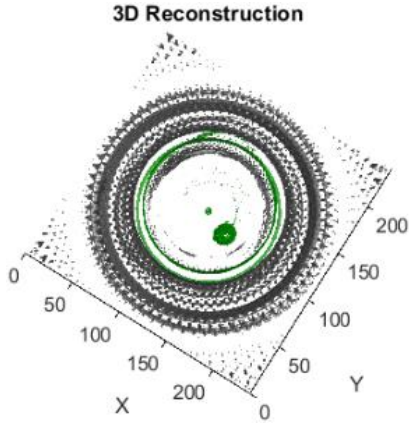


powerful multivariate algorithm that builds efficient models for predicting the future values by maximizing the covariance between the past and future data.

## IV.RESULTS

The ADEPT-GUI's ability to reconstruct a clear and sharp image of a lymph node contained in a tumor is seen in Fig 1. Although FBP is an excellent tool for image reconstructions, it is not clear enough for physicians to determine whether there is an artifact or a tumor. MLEM, on the other hand, has improved the image's quality so that the surgeons can make reliable decisions.

## V.CONCLUSION

Compared to the MLEM technique, adding FBP into the procedure strengthens the system's ability. The ADEPT-GUI system shows a strong image reconstruction capacity and will be developed to optimize cancer detection.

## VII. ACKNOWLEDGEMENTS

I worked in Dr. Ken Tichauer's lab, and the ADEPT system was designed and presented in the dissertation of Dr. Veronica Torres. Thank you, Dr. Tichauer, Dr. Torres, Mr. Rounds, and everyone in the lab for the opportunity and the assistance. This work was done sponsored under the RES-MATCH program by the Pritzker Institute of Biomedical Science and Engineering at Illinois Institute of Technology.

## VIII. REFERENCES

1. Siegel, RL; Miller, KD; Jemal, A. Cancer statistics. CA Cancer J Clin.; 69(1):7-34. doi:10.3322/caac.21551, (2019)

2. Torres, VC; Li, C; Brankov, JB; Tichauer, KM. Model-based system matrix for iterative reconstruction in sub-diffuse angular-domain fluorescence optical projection tomography. Biomed. Opt. Express 12, 1248-1262, (2

# (Quasi-)Monte Carlo Importance Sampling with QMCPy

**Aleksei G. Sorokin[1], Fred J. Hickernell[1], Sou-Cheng T. Choi[1,2], Michael J. McCourt[3], and Jagadeeswaran Rathinavel[1,4]**

[1]Department of Applied Mathematics, Illinois Institute of Technology, RE 220, 10 W. 32nd St., Chicago, IL 60616.; [2]Kamakura Corporation, 2222 Kalakaua Ave, Suite 1400, Honolulu, HI 96815.; [3]SigOpt, an Intel company, 100 Bush St., Suite 1100, San Francisco, CA 94104.; [4]Wi-Tronix LLC, 631 E Boughton Rd, Suite 240, Bolingbrook, IL 60440

**(Quasi-)Monte Carlo, (Q)MC, methods are a class of powerful numerical integration algorithms that have been proven to scale well to high dimensions. Various techniques exist to decrease the computational cost of (Q)MC methods. This article focuses on importance sampling, a technique that performs variable transformations to make the integral easier for (Q)MC approximation. The build up to composed importance sampling is paralleled by code from our QMCPy package that implements these concepts.**

Quasi-Monte Carlo | Importance Sampling | Numerical Software

Monte Carlo methods have become science's sharpest tool for high dimensional numerical integration. In low dimensions, using Gaussian quadrature, Simpson's rule, or similar numerical methods will provide fast, accurate approximation. However, as the dimension of the problem grows, these methods quickly become computationally intractable. By introducing randomness, Monte Carlo methods are able to approximate high dimensional integrals much more efficiently than the aforementioned techniques.

The central idea of Monte Carlo integration is to view an integral as the expectation of a function of a random variable with a *well-defined* probability distribution. Samples may then be drawn from that probability distribution, and the sample average of the corresponding function evaluations is the Monte Carlo integral estimate. The form of the integral that is amenable to Monte Carlo integration may require applying a change of variables to the original integral.

Monte Carlo methods can be improved with two central ideas: smarter sampling and rewriting the integrand. While standard Monte Carlo (MC) methods sample the probability distribution at independent nodes, Quasi-Monte Carlo (QMC) methods carefully coordinate sampling locations to achieve significantly faster convergence to the true mean. QMC methods can be straightforward to adapt to your standard MC problem, often requiring little more than replacing independent samples with low-discrepancy sequences.

Often times, the integrand can be rewritten to mitigate sharp peaks and valleys while preserving the value of the integral. These smoothing transforms make the integrand easier for (Q)MC methods to approximate. Control variates and importance sampling are among the most effective rewriting methods, although the choice of good control variate functions and importance sampling measures is currently more of an art than a science.

In this article, we focus on importance sampling and an extension to support multiple measures in a framework we call composed importance sampling. We have implemented this framework into QMCPy (1), our community developed

## Significance Statement

This work discusses the mathematics and implementation of importance sampling for (Quasi-)Monte Carlo methods. We extend the standard development to accommodate multiple measures in a composed importance sampling framework. This framework is demonstrated using our implementation in QMCPy, a community driven Quasi-Monte Carlo software.

Quasi-Monte Carlo Library in Python 3. Python was chosen to help make QMCPy easily accessible to the community and extendable by decades of research in (Q)MC. Throughout this work, we use QMCPy to demonstrate the benefits of importance sampling through a running example from Keister (2). Those interested in following the development of QMCPy should visit qmcpy.org.

The remainder of this article is organized as follows. We first present the (Q)MC problem and differentiate between MC and QMC methods. We then generalize the (Q)MC problem to incorporate importance sampling and extend this notion to composed importance sampling. We end by summarizing developments, discussing future research, and linking to additional resources for the QMCPy package.

## (Quasi-)Monte Carlo Methods

The model problem for (Q)MC takes the form of

$$\mu = \int_{\mathcal{T}} g(\boldsymbol{t})\lambda(\boldsymbol{t})\,\mathrm{d}\boldsymbol{t}, \qquad [1]$$

where $g : \mathcal{T} \to \mathbb{R}$ is the *original integrand* and $\lambda : \mathcal{T} \to \mathbb{R}^+$ is a non-negative weight function which we call the *true measure*. Often times the true measure is a probability distribution, but we are not restricted to this setting. For instance, the Lebesgue measure can be used by setting $\lambda(\boldsymbol{t}) = 1$.

In order to perform (Q)MC simulation, we rewrite Eq. [1] as the $d$ dimensional integrand

$$\mu = \int_{[0,1]^d} f(\boldsymbol{x})\,\mathrm{d}\boldsymbol{x}, \qquad [2]$$

where the *transformed integrand* is

$$f(\boldsymbol{x}) = g(\boldsymbol{\Psi}(\boldsymbol{x}))\lambda(\boldsymbol{\Psi}(\boldsymbol{x}))|\boldsymbol{\Psi}'(\boldsymbol{x})|. \qquad [3]$$

The change of variables is captured in $\boldsymbol{\Psi} : [0,1]^d \to \mathcal{T}$, the *transform*, and is central to importance sampling. We denote the Jacobian determinant of this transform by $|\boldsymbol{\Psi}'(\boldsymbol{x})|$. Eq. [2] can be viewed as taking the expectation of $f(\boldsymbol{X})$ when $\boldsymbol{X} \sim \mathcal{U}[0,1]^d$.

(Q)MC methods approximate the true mean $\mu$ by the sample mean of $f$ evaluated at sampling nodes $\boldsymbol{X}_0, \boldsymbol{X}_1, \ldots, \boldsymbol{X}_n \sim \mathcal{U}[0,1]^d$. We denote the $n$-sample mean by $\hat{\mu}_n$ so that

$$\hat{\mu}_n = \frac{1}{n}\sum_{i=0}^{n-1} f(\boldsymbol{X}_i) \approx \int_{[0,1]^d} f(\boldsymbol{x})\,\mathrm{d}\boldsymbol{x} = \mu.$$

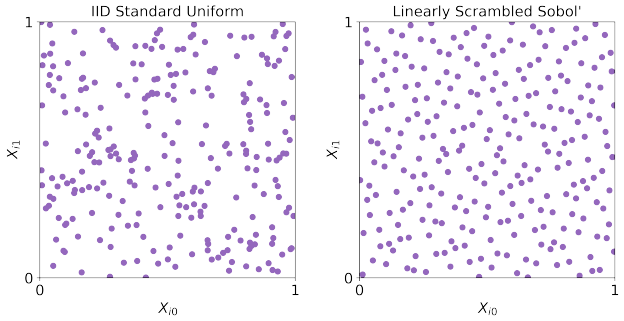


**Fig. 1.** IID points contrasted with LD Sobol' points, both mimicking $\mathcal{U}[0,1]^2$. Note how the LD sequence covers the domain more evenly than the IID points.

Standard MC methods select $\boldsymbol{X}_0, \boldsymbol{X}_1, \boldsymbol{X}_2, \ldots$ to be independent and identically distributed (IID). Recall that the multivariate probability distribution of $n$ IID points is the product of the marginals: $F_n(\boldsymbol{x}_0, \ldots, \boldsymbol{x}_{n-1}) = \prod_{i=0}^{n-1} F(\boldsymbol{x}_i)$. If $\boldsymbol{X}$ is a standard uniform random variable, then $F(\boldsymbol{x}) = x_1 \cdots x_d$ for $\boldsymbol{x} := (x_1, \ldots, x_d) \in [0,1]^d$.

QMC methods carefully select sampling nodes $\{\boldsymbol{X}_i\}_{i=0}^{n-1}$ so that their empirical distribution mimics $F$ better than the empirical distribution of IID points. The discrepancy is a measure of the difference between an empirical distribution and a target distribution. Therefore, the sampling nodes used by QMC methods are called *low-discrepancy* (LD) node sets. Common examples of LD node sets are digital sequences, integration lattices, and Halton points. Figure 1 contrasts IID and LD node sets that mimic $\mathcal{U}[0,1]^2$. Notice how the IID points leave gaps and clusters while the LD sequence covers the domain more uniformly. This better uniformity, or lower discrepancy, enables QMC integral approximation to converge significantly faster than standard MC methods.

## Importance Sampling

When true measure $\lambda$ corresponds to a probability density, we can often select a transform $\boldsymbol{\Psi}$ so that $\lambda(\boldsymbol{\Psi}(\boldsymbol{x}))|\boldsymbol{\Psi}'(\boldsymbol{x})| = 1$, i.e. the weight and Jacobian cancel. In this case, Eq. [3] simplifies to $f = g \circ \boldsymbol{\Psi}$, which is relatively easy to evaluate. However, it may be necessary or advantageous to choose $\boldsymbol{\Psi}$ so the weight and Jacobian do not cancel. For instance, no canceling transform exists when $\lambda$ corresponds to a Lebesgue measure on $\mathbb{R}^d$. As we will show later, selecting $\boldsymbol{\Psi}$ so $\lambda(\boldsymbol{\Psi}(\boldsymbol{x}))|\boldsymbol{\Psi}'(\boldsymbol{x})| \neq 1$ can often speed up a (Q)MC approximation even if a canceling transform does exist.

Importance sampling tries to select a transform $\boldsymbol{\Psi}$ to better sample the original integrand in places of higher variation. In doing so, the transformed integrand has lower variation and is therefore easier for (Q)MC methods to approximate. Specifically, anytime $\lambda(\boldsymbol{\Psi}(\boldsymbol{x}))|\boldsymbol{\Psi}'(\boldsymbol{x})| \neq 1$, we are performing importance sampling. In this case, we say $\boldsymbol{\Psi}(\boldsymbol{X})$ is stochastically equivalent to a random variable with density $\tilde{\lambda}$ when $\boldsymbol{X} \sim U[0,1]^d$. This implies $\tilde{\lambda}(\boldsymbol{\Psi}(\boldsymbol{x}))|\boldsymbol{\Psi}'(\boldsymbol{x})| = 1$ for some $\tilde{\lambda} : \mathcal{T} \to \mathbb{R}^+$ so that

$$f(\boldsymbol{x}) = g(\boldsymbol{\Psi}(\boldsymbol{x}))\, \frac{\lambda(\boldsymbol{\Psi}(\boldsymbol{x}))}{\tilde{\lambda}(\boldsymbol{\Psi}(\boldsymbol{x}))}. \qquad [4]$$

The choice of $\boldsymbol{\Psi}$, or equivalently $\tilde{\lambda}$, is currently a manual task that often requires a good deal of problem-specific knowledge.

**The Keister Integrand.** Suppose we want to approximate the following integrand from Keister

$$\mu = \int_{\mathbb{R}^d} \cos(\|\boldsymbol{t}\|) \exp(-\|\boldsymbol{t}\|^2) \mathrm{d}\boldsymbol{t}. \qquad [5]$$

Notice that we may split the integrand into original function $g$ and true measure $\lambda$ so that

$$\mu = \int_{\mathbb{R}^d} \underbrace{\pi^{d/2} \cos(\|\boldsymbol{t}\|)}_{g(\boldsymbol{t})} \underbrace{\pi^{-d/2} \exp(-\|\boldsymbol{t}\|^2)}_{\lambda(\boldsymbol{t})} \mathrm{d}\boldsymbol{t}, \qquad [6]$$

and $\lambda$ is the probability density of a multivariate Gaussian with mean $\mathbf{0}$ and covariance $\mathsf{I}/2$. We denote the density of this true measure by $\lambda(\boldsymbol{t}) = \mathcal{N}(\boldsymbol{t}|\mathbf{0}, \mathsf{I}/2)$.

To approximate this integral, we use QMCPy, a community-develop QMC package for Python. QMCPy includes the Keister integrand as just defined. To set up the (Q)MC problem without importance sampling, we only need to define a LD sequence. In this case, we choose the LD Sobol' sequence (see Figure 1) in order to perform QMC quadrature.

First, we import QMCPy via:

```
>>> import qmcpy as qp
```

Then, we initialize a 3-dimensional Sobol' sequence and Keister integrand:

**Listing 1.** Standard Keister Construction

```
>>> d = 3
>>> sobol = qp.Sobol(d,seed=11)
>>> K_std = qp.Keister(sobol)
```

The transform defaults to $\boldsymbol{\Psi}(\boldsymbol{x}) = \boldsymbol{\Phi}^{-1}(\boldsymbol{x})/\sqrt{2}$, where $\boldsymbol{\Phi}^{-1}$ is the element-wise inverse CDF of a standard Gaussian. This transform was chosen so that $\lambda(\boldsymbol{\Psi}(\boldsymbol{x}))|\boldsymbol{\Psi}'(\boldsymbol{x})| = 1$, and we recover $f = g \circ \boldsymbol{\Psi}$. Therefore, our standard, or default, Keister function is *not* using importance sampling.

To evaluate the integrand, we first generate samples from the Sobol' sequence. These samples are then input to the transformed integrand, $f$, which was automatically constructed for us by QMCPy.

```
>>> x = sobol.gen_samples(2**4)
>>> y = K_std.f(x)
```

Figure 2 shows the standard Keister integrand in one-dimension evaluated at the first $2^4$ points of a scrambled Sobol' sequence.

We may now run a QMC quadrature algorithm to approximate the integrand to within absolute tolerance $\epsilon =$ 5e-6.

**Listing 2.** Stopping Criterion Evaluation

```
>>> sc = qp.CubQMCSobolG(
...       integrand = K_std,
...       abs_tol = 5e-6)
>>> sol,data = sc.integrate()
```

In this case the *stopping criterion* algorithm, which determines the number of samples necessary to achieve the desired tolerance, is based

on the decay of the integrand's Fourier Walsh coefficients. The outputs of calling `integrate()` on the `qp.CubQMCSobolG` (3) stopping criterion are a numerical solution and data object that houses integration information. Table 1 collects the number of samples and run time from this data object.

We now turn our attention to importance sampling the Keister integrand. For this example, we choose transform $\boldsymbol{\Psi}(\boldsymbol{x}) = \sqrt{3}\boldsymbol{\Phi}^{-1}$ so that $\tilde{\lambda}(\boldsymbol{t}) = \mathcal{N}(\boldsymbol{t}|\mathbf{0}, 3\mathsf{I})$ and $\tilde{\lambda}(\boldsymbol{\Psi}(\boldsymbol{x}))|\boldsymbol{\Psi}'(\boldsymbol{x})| = 1$. Therefore, our transformed Keister integrand becomes

$$f(\boldsymbol{x}) = \pi^{d/2}\cos(\|\boldsymbol{\Psi}(\boldsymbol{x})\|)\,\frac{\mathcal{N}(\boldsymbol{\Psi}(\boldsymbol{x})|\mathbf{0}, \mathsf{I}/2)}{\mathcal{N}(\boldsymbol{\Psi}(\boldsymbol{x})|\mathbf{0}, 3\mathsf{I})}.$$

In QMCPy, we first define our importance sampling measure, in this case $\mathcal{N}(\mathbf{0}, 3\mathsf{I})$, and then use it to construct our Keister integrand with an importance `sampler`.

```
>>> transform = qp.Gaussian(
...     sampler = sobol,
...     mean = 0,
...     covariance = 3)
>>> K_gauss = qp.Keister(transform)
```

Note how we construct the `Keister` integrand using the `Gaussian` importance sampling measure rather than the `sobol` generator as done in Listing 1. A one-dimensional version of this importance sampling integrand is plotted in Figure 2 as `Gauss Keister IS`. While the one and three dimensional Keister examples give similar savings for this example, it is not always the case that copying parameters to different dimensions will result in similar success.

QMC integration of the above Keister function with importance sampling is done in an analogous manner to Listing 2. Table 1 compares the required time and samples against the non-importance sampled Keister. Notice how the savings in samples is greater than the savings in time since the importance sampling integrand requires an additional Jacobian computation at each sample.

## Composed Importance Sampling

We now generalize importance sampling to allow multiple sub-transforms. Let $\boldsymbol{\Psi}_0(\boldsymbol{x}) = \boldsymbol{x}$ and denote the composition of the first $\ell$ (non-identity) sub-transforms by $\hat{\boldsymbol{\Psi}}_\ell = (\boldsymbol{\Psi}_\ell \circ \boldsymbol{\Psi}_{\ell-1} \circ \cdots \circ \boldsymbol{\Psi}_0)$. Therefore, the complete $L$ sub-transform composition is $\boldsymbol{\Psi} = \hat{\boldsymbol{\Psi}}_L$. The sub-transforms must be compatible with the discrete distribution and true measure, meaning $\boldsymbol{\Psi}_\ell : [0,1]^d \to [0,1]^d$ for $\ell = 1, \dots L-1$ and $\boldsymbol{\Psi}_L : [0,1]^d \to \mathcal{T}$. Define $\lambda_l$ to be the density of $\boldsymbol{\Psi}_\ell(\boldsymbol{X}_\ell)$ for $\boldsymbol{X}_\ell \sim \mathcal{U}[0,1]^d$ so that $\lambda_\ell(\boldsymbol{\Psi}_\ell(\boldsymbol{x}))|\boldsymbol{\Psi}_\ell'(\boldsymbol{x})| = 1$. The chain rule then implies that

$$\begin{aligned} f(\boldsymbol{x}) &= g(\hat{\boldsymbol{\Psi}}_L(\boldsymbol{x}))\,\lambda(\hat{\boldsymbol{\Psi}}_L(\boldsymbol{x}))\prod_{\ell=1}^{L}|\boldsymbol{\Psi}_\ell'(\hat{\boldsymbol{\Psi}}_{\ell-1}(\boldsymbol{x}))| \\ &= g(\hat{\boldsymbol{\Psi}}_L(\boldsymbol{x}))\,\frac{\lambda(\hat{\boldsymbol{\Psi}}_L(\boldsymbol{x}))}{\prod_{\ell=1}^{L}\lambda_\ell(\hat{\boldsymbol{\Psi}}_\ell(\boldsymbol{x}))}. \end{aligned}$$

***The Keister Integrand.*** Let us now return to the Keister integrand which is defined in Eq. [6] with original integrand $g(\boldsymbol{t}) = \pi^{d/2}\cos(\|\boldsymbol{t}\|)$ and true measure $\lambda(\boldsymbol{t}) = \mathcal{N}(\boldsymbol{t}|\mathbf{0}, \mathsf{I}/2)$. Suppose we are interested in importance sampling by a composed Gaussian-Kumaraswamy distribution. The Kumaraswamy distribution (4), denoted $\mathcal{K}(\boldsymbol{a}, \boldsymbol{b})$, may be sampled via an inverse CDF transform $\boldsymbol{\Psi}_K : [0,1]^d \to [0,1]^d$, and the Gaussian distribution, denoted $\mathcal{N}(\boldsymbol{\mu}, \Sigma = \mathsf{A}\mathsf{A}^T)$, may be sampled via transform $\boldsymbol{\Psi}_G : [0,1]^d \to \mathbb{R}^d$ defined as $\boldsymbol{\Psi}_G(\boldsymbol{x}) = \mathsf{A}\boldsymbol{\Phi}^{-1} + \boldsymbol{\mu}$. Again, $\boldsymbol{\Phi}^{-1}$ is the element-wise inverse CDF transform of a standard normal. Due to the nature of these transforms, we have $\lambda_K(\boldsymbol{t}) = \mathcal{K}(\boldsymbol{t}|\boldsymbol{a}, \boldsymbol{b})$, $\lambda_G(\boldsymbol{t}) = \mathcal{N}(\boldsymbol{t}|\boldsymbol{\mu}, \Sigma)$, and $\lambda_K(\boldsymbol{\Psi}_K(\boldsymbol{x}))|\boldsymbol{\Psi}_K'(\boldsymbol{x})| = 1 = \lambda_G(\boldsymbol{\Psi}_G(\boldsymbol{x}))|\boldsymbol{\Psi}_G'(\boldsymbol{x})|$. Therefore, we define the complete transform as $\boldsymbol{\Psi} = \boldsymbol{\Psi}_G \circ \boldsymbol{\Psi}_K$ so that

$$f(\boldsymbol{x}) = \frac{\pi^{d/2}\cos(\|\boldsymbol{\Psi}(\boldsymbol{x})\|)\,\mathcal{N}(\boldsymbol{\Psi}(\boldsymbol{x})|\mathbf{0}, \mathsf{I}/2)}{\mathcal{K}(\boldsymbol{\Psi}_K(\boldsymbol{x})|\boldsymbol{a}, \boldsymbol{b})\,\mathcal{N}(\boldsymbol{\Psi}(\boldsymbol{x})|\boldsymbol{\mu}, \Sigma)}.$$

In QMCPy, we compose transforms through the nested construction of measure objects. The following code uses the `sobol` instance from Listing 1 to construct the first Kumaraswamy transform which is used to construct the second Gaussian transform. Note how the construction of

**Table 1.** Comparing the time (seconds) and samples necessary to integrate Keister functions to within absolute tolerance 5e-6. The percent usage of importance sampling (IS) integrands compared to the standard, non-importance sampling, integrand are also displayed. Using importance sampling significantly decreases the computational budget required for accurate approximation. The Sobol sequence and corresponding stopping criterion favor sample sizes that are powers of 2.

| | Time | Samples |
|---|---|---|
| Standard Keister | 3.8 | $2^{22}$ |
| Gauss Keister IS | 2.6 (70%) | $2^{21}$ (50%) |
| Gauss-Kuma Keister IS | 1.3 (35%) | $2^{20}$ (25%) |

QMCPy objects reflects the composition of sub-transforms used to define the complete transform. Finally, the Gaussian-Kumaraswamy measure is used to construct a Keister integrand which defines the original integrand and true measure.

```
>>> tf_K = qp.Kumaraswamy(
...       sampler = sobol,
...       a = .8,
...       b = .8)
>>> tf_G = qp.Gaussian(
...       sampler = tf_K)
>>> K_Gauss_Kuma = qp.Keister(tf_G)
```

Figure 2 plots a one-dimensional `Gauss-Kuma Keister IS` function against the Keister functions developed previously. Again, we may integrate the composed importance sampling measure using Listing 2. The results of this integration are displayed in Table 1. Both importance sampling examples deliver significant savings in time and samples compared to the standard, non-importance sampling, Keister integrand.

## Conclusion

In this work we have presented and exemplified importance sampling for (Quasi-)Monte Carlo methods. Specifically, we focused on developing the composed importance sampling framework and showing its potential to improve the efficiency of Quasi-Monte Carlo approximation. Throughout this work, the QMCPy package was used to easily setup and execute importance sampling in a flexible and intuitive framework.

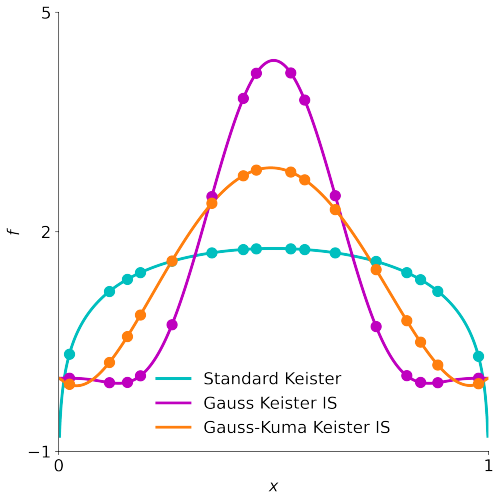


**Fig. 2.** The Keister integrand without importance sampling (`Standard Keister`), with Gaussian importance sampling (`Gaussian Keister IS`), and with composed Gaussian-Kumaraswamy importance sampling (`Gauss-Kuma Keister IS`). Each transformed integrand shows the sampling locations of the same 16 scrambled Sobol' points. The lower variation of importance sampling integrands makes their (Q)MC approximation more efficient.

**Future Work.** Control variates are another popular and powerful technique to rewrite the original integral. In the future, we plan to add support for control variates into QMCPy. We hope QMCPy's support for these performance enhancing techniques will allow (Q)MC researchers and practitioners to more easily access their benefits.

While importance sampling and control variates can provide substantial benefits to (Q)MC methods, the choice of an effective importance sampling measure or control variate function is currently a difficult and manual task. In the future we hope to develop algorithms to automatically select good importance sampling measures and control variate functionals, perhaps using machine learning. If successful, we would like to implement these methods into QMCPy to extend their benefits to a wider user base.

**QMCPy Resources.** To learn more about QMCPy for (Quasi-)Mote Carlo, we recommend our article for the MCQMC2020 proceedings (5) and the resources therein. Those interested in following the development of QMCPy are urged to visit qmcpy.org or view our GitHub repository at github.com/QMCSoftware/QMCSoftware.

**Acknowledgements.** We would like to thank SigOpt and National Science Foundation grant DMS-1522687 for their continued support of this project.

## References

1. Sou-Cheng T. Choi, Fred J. Hickernell, R. Jagadeeswaran, Michael J. McCourt, and Aleksei G. Sorokin. QMCPy: A Quasi-Monte Carlo Python library, 2020+. URL https://github.com/QMCSoftware/QMCSoftware.
2. B. D. Keister. Multidimensional quadrature algorithms. *Computers in Physics*, 10:119–122, 1996. .
3. Fred J. Hickernell and Lluís Antoni Jiménez Rugama. Reliable adaptive cubature using digital sequences, 2014.
4. P. Kumaraswamy. A generalized probability density function for double-bounded random processes. *Journal of Hydrology*, 46(1):79–88, 1980. ISSN 0022-1694. . URL https://www.sciencedirect.com/science/article/pii/0022169480900360.
5. Sou-Cheng T. Choi, Fred J. Hickernell, R. Jagadeeswaran, Michael J. McCourt, and Aleksei G. Sorokin. Quasi-monte carlo software, 2021.

# DNPC: A Dynamic Node-level Power Capping Library for Scientific Applications

**Sahil Sharma**[a,1], **Zhiling Lan**[a], **Xingfu Wu**[b], **and Valerie Taylor**[b]

[a] Department of Computer Science, Illinois Institute of Technology, Chicago, IL 60616 ; [b] Mathematics and Computer Science Division, Argonne National Laboratory, Lemont, IL 60439

**As the race to exa-scale computing accelerates, power consumption continues to be a critical challenge. While several technologies are available for power management, balancing energy efficiency and application performance during execution remains an important topic of research. In this study, we develop an open-source library called DNPC for dynamically controlling an application's package-level power consumption during execution. Given a specific performance degradation threshold, DNPC aims to minimize power consumption by following the application's power profile and adjusting the power cap accordingly. Further, DNPC is able to estimate the online performance of an application under capping, and predict its estimated performance degradation relative to an uncapped run. In this paper, we present an overview of the library, followed by a case study to illustrate the use of DNPC with an Exascale Computing Project proxy application on a production supercomputer at Argonne National Laboratory.**

High-Performance Computing | Power Management | Online Performance Monitoring

Current high-performance computing (HPC) systems require a large amount of electricity to operate system components. As HPC systems increase in scale and capability, the cost of supplying power to these systems will grow as well. In fact, it is estimated that the energy cost of a large-scale system during its lifetime can surpass the equipment itself (1). This introduces the urgent need for energy efficient computing through controlling power consumption. However, there is not one clear solution to achieve this result. The PowerStack initiative provides a holistic and extensible power management framework (2). It defines power management interfaces at three specific levels: cluster scheduler, job-level runtime systems, and node-level managers. The Global Extensible Open Power Manager (GEOPM) from Intel is a framework for exploring power and energy optimization. It provides an energy profiling and monitoring tool as well as multi-node power balancer to optimize power across nodes based on work imbalance. RAPL exposes a number of model-specific registers (MSRs) that can be used to monitor energy and set power limits on different parts of a chip (3). PoLiMEr provides C functions to leverage RAPL for application-level power monitoring and capping (4).

While the tools above provide useful monitoring or certain power management capabilities, little work has been done to investigate when and how much power capping should be applied during application execution. In particular, an open question is: *given a specific bound for application performance degradation, how can we dynamically adjust the power cap during execution so as to minimize power usage?* PoLiMEr includes functions to set and monitor power caps, but these must be set manually and are limited to functions visible within the application source code. This requires offline analysis of the application to know when and how much to set the power cap to. Additionally, every time an adjustment to the capping scheme is made, the application source code must be modified and recompiled. Gholkar et al. developed UPScavenger, a runtime system to save power by dynamically detecting phase changes and automatically tuning uncore frequency during application execution (5). UPScavenger targets uncore power saving and is not designed for package level power saving.

In this study, we aim to address this problem by developing *DNPC, a Dynamic Node-level Power manager and Capping library for high-performance computing.* A key challenge is to estimate online performance during application execution. Ramesh et al. (6) found that online performance is highly correlated with the figure of merit; however their work is limited to the applications for which a figure of merit is defined. Our work addresses this issue through fine-grained power profiling and active hardware counter analysis. DNPC directly incorporates PoLiMEr and PAPI (7). It includes several adaptive algorithms for runtime performance prediction and power capping. DNPC is also able to detect and follow patterns in the power curve, called power phases, without offline profiling. Another key feature is that DNPC can estimate the online performance of the application based on execution time relative to uncapped performance, and use this estimation to control the predicted amount of performance degradation from power capping. The library can utilize the detection of phases to set the appropriate package power cap to minimize power during execution. DNPC is easy to use: to use the library, a user only needs to insert a couple of lines of code into their application code.

## DNPC Overview

DNPC allows easy dynamic package power capping of single node applications written in C or C++. Currently, there are no plans to extend DNPC to monitor multiple nodes at once.

[1] To whom correspondence should be addressed. E-mail: ssharma18@hawk.iit.edu

```c
#include "dnpc.h"
int main(int argc, char *argv[])
{
    /* application code */
    MPI_Init(&argc, &argv);
    dnpc_init();
    /* application code */
    dnpc_finalize();
    MPI_Finalize();
    /* application code */
}
```

**Listing 1.** An example to illustrate the use of DNPC with an application

It works by combining the energy monitoring and hardware counter monitoring of PoLiMEr and PAPI, respectively. It employs one of any number of built-in or user-supplied algorithms during run-time to periodically and dynamically set a power cap.

**Algorithms.** While DNPC uses PoLiMEr and PAPI to monitor an application's behavior, its main benefit comes from using the data from these libraries every polling cycle as inputs to a run-time algorithm that outputs a power cap to set. Only one algorithm can be used for an application's execution. While the user can easily add their own algorithm, four different dynamic capping algorithms are already implemented within DNPC. More will be added as we continue investigating power management. Their designs are based on state machines in order to be easy to interpret and to have minimal overhead. These four algorithms are briefly explained here.

1. The first algorithm examines the current frequency reading to decide if power capping is needed, and looks at the change in instructions per cycle (IPC) to determine phase changes before adjusting the power cap.

2. The second algorithm builds upon the first by estimating the current online performance and adjusting the amount to set the cap based on that estimate and the degradation threshold.

3. The third algorithm is similar to the second, but exchanges the change in IPC for the change in the ratio of micro-operations to normal instructions to determine phase changes.

4. The last algorithm is an iteration of the third, switching the order in which the micro-operation ratio and current frequency are checked in determining phase changes and power capping candidates.

**Using DNPC.** DNPC is implemented in C and contains about 1000 lines of code. The core interface only consists of two functions: one to initialize the library, and the other to finalize it. Before modifying the application code, PoLiMEr, PAPI, and an implementation of MPI should be compiled and available on the system. PoLiMEr should be compiled with the `TIMER_OFF` flag, as signal-based timers will conflict with DNPC's internal timer. While DNPC is a user-level library, PoLiMEr internally uses RAPL for power capping, so the user should contact their system administrator for privileges to read/write certain MSRs as outlined in PoLiMEr's documentation. After the appropriate setup, the only modifications to the source code required are shown in Listing 1. After the application is run, it will output four files with the energy, performance, and counter data recorded.

The flexibility of DNPC comes in its configuration through environment variables. This allows different environment settings within a batch submission script to be set without having to recompile the library or the application. Some important environment variables that can be set are the dynamic capping algorithm, the performance degradation threshold, the polling interval, PAPI counters to collect, and more.

Adding a new power capping algorithm is simple as well. The only steps required are to first write a new function within the `dnpc.c` file, add the function to the `dnpc.h` file, and finally add it as case within the polling function's algorithm `switch` statement.

We plan to release the library as open source on GitHub after we extensively evaluate the library with more applications.

### Application Case Study

We now show a case study of applying DNPC to an application to illustrate the benefits of the library. The application is an Exa-scale Computing Project (ECP) proxy app (8) called MiniQMC. MiniQMC is a "mini" version of QMCPACK (9) designed to be used for benchmarks and optimization testing, and it is available freely on GitHub or from the ECP website. MiniQMC uses different quantum Monte Carlo algorithms in order to calculate the total energy of a quantum mechanical system. Different algorithms and kernels present opportunities within the power profile for power cap adjustments.

MiniQMC was configured with DNPC, MPI, 64 OpenMP threads, and a problem size of 128 atoms and 1536 electrons. We then performed the following experiment on a single node of the Cray XC40 supercomputer Theta at Argonne National Laboratory. Each Theta node is equipped with 192 GiB of DRAM, 16 GiB of MCDRAM, and an Intel KNL 7230 processor with 64 cores. On the same node, we first ran MiniQMC without any power capping, then again using dynamic power capping based on Algorithm 3 from DNPC. Each configuration had three trials taken, and the results of one of the trials for each is shown in Figure 1. In the evaluation, the median value from the trials was taken for each metric.

Looking at Figure 1b, it can be seen that the dynamic power cap curve follows the phases of the power curve and adapts accordingly. Also important to note is that the power cap curve becomes more conservative as time goes on due to the estimated performance approaching the degradation threshold of 5%. Three metrics are used in our evaluation:

1. **Execution Time**
   It is defined as how much time the application runs for.

2. **Total Energy**
   It is defined as the total amount of energy consumed by the package and the DRAM during the execution of the application with a dynamic package power cap.

3. **Rescued Energy**
   It is defined as the area between the power given by the

**(a)** MiniQMC Without Power Capping

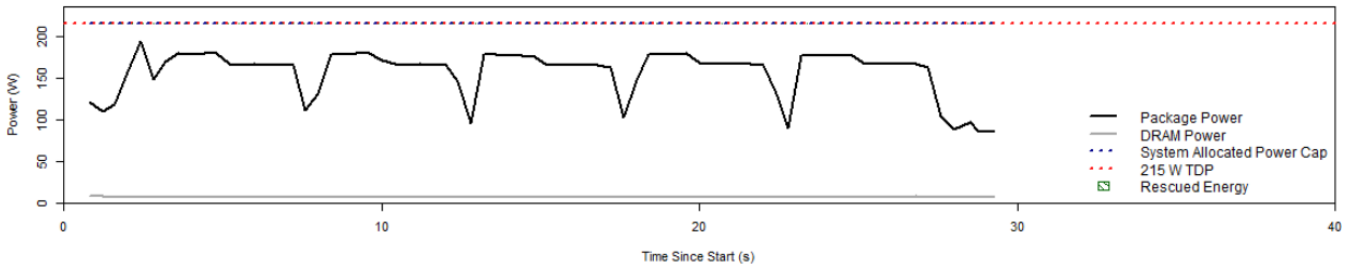


**(b)** MiniQMC With Dynamic Power Capping (Alg. 3), and Degradation Threshold of 5%

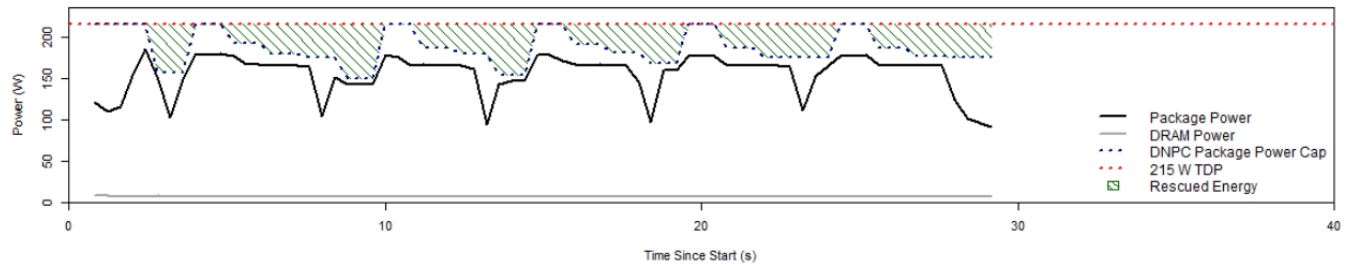


**Fig. 1.** Power profiles of executions of MiniQMC. (1a) Trial without power capping. (1b) Trial with dynamic power capping from DNPC. In 1a, we assume the system-level power manager has given the node a power cap set to the TDP of the processor. In 1b, where there is a dynamic power cap that is typically below TDP, the system-level power manager can reclaim the rescued energy and distribute to other jobs.

system-level power manager and the power cap set by DNPC. In our experiment, the Thermal Design Power (TDP) of 215 Watts is used as the default power cap given by the system-level power manager. This metric is similar to the stranded power metric used in the context of power grids (10).

The first two metrics are calculated using the median value of the dynamic power cap configuration normalized by the median value of the configuration without a power cap. The third metric is different in that it is normalized by the total energy from the configuration without a power cap rather than the rescued energy (since it is zero for the baseline configuration).

While not directly an evaluation metric, the accuracy between the (normalized) execution time predicted by DNPC and the actual execution time is important to consider. Predicting the total execution time at run-time, or online performance, is difficult as many factors can affect the runtime. DNPC simplifies this prediction by not predicting the actual time, but by predicting the estimated percent of performance degradation from using a power cap compared to not using one. It updates this prediction every polling cycle, and a user can supply a constraint that DNPC will try to stay under while power capping.

Looking at the results of MiniQMC under a dynamic power cap, there are two main takeaways. The first being that the dynamic package power cap may not always bring energy savings. The (normalized) total energy for MiniQMC under Algorithm 3 was 1.00, which means the total energy used under a dynamic power cap was the same as the typical case without one. In this case, the increased execution time from the power capping caused the total energy to be the same despite the lower average power usage. This could mean that this MiniQMC specifically is less receptive to power capping, or that this algorithm performs poorly in terms of energy savings. In either case, more tests on different applications will have to be taken in order to verify these findings. However, the rescued energy presents a great benefit from dynamic power capping. The baseline configuration of MiniQMC does not have a power cap, so we assume that the power cap seen by the power manager above the node to be the TDP of the processor. Therefore, the configuration without a power cap in this case has no rescued energy. The rescued energy for MiniQMC under Algorithm 3 was 0.19, or an amount of energy equivalent to 19% of the total energy used in the configuration without a dynamic power cap was reclaimed. Although the total energy used did not decrease, in a multi-node system the rescued energy could be allocated to other nodes.

The second takeaway being that DNPC can estimate the online performance with close accuracy. MiniQMC's (normalized) execution time under Algorithm 3 was 1.05, while its online estimation for that metric was 1.06. Further, since it was given a performance degradation threshold of 5%, this shows it was also able to enable the dynamic power cap while staying within that constraint.

**ACKNOWLEDGMENTS.** This work is supported in part by US National Science Foundation grants CCF-1618776 and CCF-1801856. We acknowledge Argonne Leadership Computing Facility for use of the Cray XC40 Theta machine.

**References**


1. Peter Kogge, S. Borkar, Dan Campbell, William Carlson, William Dally, Monty Denneau, Paul Franzon, William Harrod, Jon Hiller, Stephen Keckler, Dean Klein, and Robert Lucas. Exascale computing study: Technology challenges in achieving exascale systems. *Defense Advanced Research Projects Agency Information Processing Techniques Office (DARPA IPTO), Techinal Representative*, 15, 01 2008.
2. Christopher Cantalupo, Jonathan Eastep, Siddhartha Jana, Masaaki Kondo, Matthias Maiter, Aniruddha Marathe, Tapasya Patki, Barry Rountree, Ryuichi Sakamoto, Martin Schulz, and Carsten Trinitis. A strawman for an hpc powerstack. Technical report, 2018.
3. Howard David, Eugene Gorbatov, Ulf Hanebutte, Rahul Khanna, and Christian Le. Rapl: Memory power estimation and capping. In *ISLPED*, pages 189–194, 01 2010. .
4. Ivana Marincic, Venkatram Vishwanath, and Henry Hoffmann. Polimer: An energy monitoring and power limiting interface for hpc applications. In *Proceedings of the 5th International Workshop on Energy Efficient Supercomputing*, E2SC'17, New York, NY, USA, 2017. Association for Computing Machinery. ISBN 9781450351324. . URL https://doi.org/10.1145/3149412.3149419.
5. Neha Gholkar, Frank Mueller, and Barry Rountree. Uncore power scavenger: A runtime for uncore power conservation on hpc systems. In *Proceedings of the International Conference for High Performance Computing, Networking, Storage and Analysis*, SC '19, New York, NY, USA, 2019. Association for Computing Machinery. ISBN 9781450362290. . URL https://doi.org/10.1145/3295500.3356150.
6. S. Ramesh, S. Perarnau, S. Bhalachandra, A. D. Malony, and P. Beckman. Understanding the impact of dynamic power capping on application progress. In *2019 IEEE International Parallel and Distributed Processing Symposium (IPDPS)*, pages 793–804, 2019. .
7. Dan Terpstra, Heike Jagode, Haihang You, and Jack Dongarra. Collecting performance data with papi-c. In Matthias S. Müller, Michael M. Resch, Alexander Schulz, and Wolfgang E. Nagel, editors, *Tools for High Performance Computing 2009*, pages 157–173, Berlin, Heidelberg, 2010. Springer Berlin Heidelberg. ISBN 978-3-642-11261-4.
8. Ecp proxy apps suite, 2021. URL https://proxyapps.exascaleproject.org/ecp-proxy-apps-suite/.
9. Jeongnim Kim, Andrew D Baczewski, Todd D Beaudet, Anouar Benali, M Chandler Bennett, Mark A Berrill, Nick S Blunt, Edgar Josué Landinez Borda, Michele Casula, David M Ceperley, Simone Chiesa, Bryan K Clark, Raymond C Clay, Kris T Delaney, Mark Dewing, Kenneth P Esler, Hongxia Hao, Olle Heinonen, Paul R C Kent, Jaron T Krogel, Ilkka Kylänpää, Ying Wai Li, M Graham Lopez, Ye Luo, Fionn D Malone, Richard M Martin, Amrita Mathuriya, Jeremy McMinis, Cody A Melton, Lubos Mitas, Miguel A Morales, Eric Neuscamman, William D Parker, Sergio D Pineda Flores, Nichols A Romero, Brenda M Rubenstein, Jacqueline A R Shea, Hyeondeok Shin, Luke Shulenburger, Andreas F Tillack, Joshua P Townsend, Norm M Tubman, Brett Van Der Goetz, Jordan E Vincent, D ChangMo Yang, Yubo Yang, Shuai Zhang, and Luning Zhao. QMCPACK: an open sourceab initioquantum monte carlo package for the electronic structure of atoms, molecules and solids. *Journal of Physics: Condensed Matter*, 30(19):195901, apr 2018. . URL https://doi.org/10.1088/1361-648x/aab9c3.
10. K. Kim, F. Yang, V. M. Zavala, and A. A. Chien. Data centers as dispatchable loads to harness stranded power. *IEEE Transactions on Sustainable Energy*, 8(1):208–218, 2017. .

# Simulations of external multi-particle DLA on the plane and connections to the super-cooled Stefan problem

**Alex Negrón**[1] **and Sergey Nadtochiy**[1]

[1]Department of Applied Mathematics, Illinois Institute of Technology

**We consider the external multi-particle diffusion-limited aggregation (MDLA) process on the 2-dimensional integer grid. In this random growth process, particles are distributed uniformly at random on the grid and undergo a simple symmetric random walk with exclusion. They walk until they contact a collection of particles centered at the origin, at which point they attach. Iterating this process, a cluster forms. Since its inception, DLA models in the plane have resisted rigorous mathematical treatment. Whereas mathematicians have succeeded in establishing scaling limits for other stochastic growth models, this result for DLA processes remains elusive. Recent findings in (1) establish a connection between the 1-dimensional MDLA process and solutions to a partial differential equation known as the super-cooled Stefan problem in one space dimension (1SSP). By fully characterizing the solutions to 1SSP, scaling limits for the 1-dimensional MDLA process were proven. It is natural to conjecture that a similar connection holds between 2-dimensional MDLA and SSP in two space dimensions. To address this conjecture, we take a numerical approach. We simulate the 2-dimensional MDLA process by decreasing the grid mesh towards 0. By studying the regularity of the cluster's interior and the statistical properties of its boundary, we show that the 2-dimensional MDLA process does not converge to solutions of 2SSP. We discuss why this process fails and propose possible resolutions.**

Diffusion limited-aggregation | Super-cooled Stefan problem

Stochastic growth processes of the diffusion-limited aggregation (DLA) type have attracted great interest since their introduction by Witten and Sander in (11). In this classical DLA model, we start with a single seed point centered at the origin of $\mathbb{Z}^2$, and generate a second particle according to a chosen distribution away from the seed point, and allow this particle to take steps of unit size following a symmetric random walk. This particle walks until it visits a site adjacent to the seed, at which point the particle attaches to the cluster. A third particle is spawned on $\mathbb{Z}^2$ away from the cluster and follows a symmetric random walk until it contacts the cluster and attaches. We iterate this process until the cluster grows to some satisfactory size. Rosenstock and Marquardt expanded the original DLA model in (7) by letting the aggregate grow in $\mathbb{Z}^d$ by starting with the initial cluster as a point $\{0\}$, and attaching a neighboring site whenever a particle from a process evolving outside of the aggregate enters a site adjacent to the aggregate. Notably, in contrast to the classical DLA model, these particles evolve simultaneously. We refer to such a growth process as multi-particle DLA (MDLA). Much of the interest in DLA-type models focuses on the dendritic nature of the aggregates formed. These structures qualitatively agree with the shapes observed experimentally in crystallization, electrodeposition, and bacteria colony growth (8).

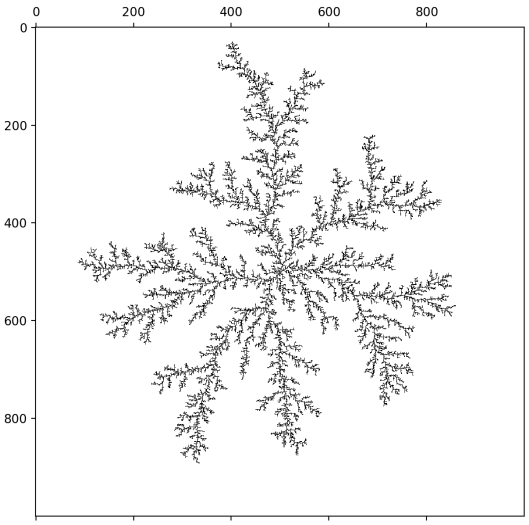


**Fig. 1.** Classical DLA cluster for $N = 1000$.

To illustrate the dendritic and fractal-like nature of the boundary of DLA aggregates, we have implemented a variant of the classical DLA model with several convenient optimizations made to reduce computational costs. Algorithm 1 is capable of producing a cluster on a $1000 \times 1000$ grid in four hours, running in Python.

Many numerical simulation studies of the aggregates resulting from DLA (6, 9, 10) have led to estimations of the fractal dimension of the aggregate as $\approx 1.7$ in two space dimensions (4, 5). Despite the interest in DLA processes, the mathematical theory of such processes in $\mathbb{Z}^d$ for $d \geq 2$ is poorly understood. Indeed, Sander describes the DLA process as a "devilishly difficult model to solve, even approximately" in (11). For the aggregate in (9), the only rigorous mathematical results we have is an upper bound on its radius upon the attachment of $n$ sites, and an almost sure convergence to infinity of the number of "holes" in the aggregate when $d = 2$ (3).

## Connection to the super-cooled Stefan problem

In one space dimension $d = 1$ progress towards a mathematically rigorous understanding of DLA has been made. In (2), it is shown that the path of the right endpoint of the aggregate converges to the free boundary $\Lambda$ in the *single-phase super-cooled Stefan problem* (1SSP) for the heat equation up to an

**Algorithm 1:** Classical DLA with optimization

**Input:** $N$, $r$, $R$
Initialize an $N \times N$ matrix $A$ of zeros. Denote the entry at the center of this matrix $A_{\frac{N}{2},\frac{N}{2}}$.
For the seed particle, set $A_{\frac{N}{2},\frac{N}{2}} = 1$
**while** *cluster radius* $< R$ **do**
  Spawn a particle $p$ uniformly at random on a circle of radius $r$ centered at $(N/2, N/2)$.
  **while** *$p$ is neither adjacent to a site in the cluster, adjacent to a site on the boundary of* $\Gamma$*, nor at a distance $R$ from the seed* **do**
    Step $p$ in a random direction: up/down/left/right with equal probability
    **if** *Distance between $p$ to seed* $> R$ **then**
      Remove $p$ and spawn a new one at radius $r$.
    **else if** *$p$ is adjacent to a cluster site* **then**
      Set corresponding `matrix` entry to 1
      **if** *the distance from $p$ to the seed is greater than $r$* **then**
        $r = r + 1$
  **end**
**end**
Print image of $A$, coloring all 1s black and all 0s white.

appropriate scaling of time. The classical 1SSP in one spatial dimension models the freezing of a supercooled liquid on the half-line strip $[0, \infty)$. The initial temperature of the liquid is lower than the temperature maintained at the liquid's surface, which lies below the freezing point of the liquid in question. The main result of (1) defines this problem as follows

$$\partial_t u = \frac{1}{2}\partial_{xx} u, \qquad \alpha\Lambda_t < x < \infty, \quad t \geq 0, \qquad [1]$$

$$u(t, \alpha\Lambda_t) = 0, \qquad t \geq 0, \qquad [2]$$

$$\partial_x u(t, \alpha\Lambda_t) = -2\alpha\dot{\Lambda}_t, \qquad t \geq 0, \qquad [3]$$

$$u(0, x) = -\alpha f(x), \qquad x \geq 0.[ \qquad [4]$$

where $f \geq 0$ and $\alpha > 0$. We interpret $t, x$, and $u = u(t, x)$ as time, position, and temperature, respectively. The freezing point is captured by $u = 0$, and the "freezing front" (i.e., the interface between solid and liquid phases) at time $t$ is located at position $x = \alpha\Lambda_t$. We assume $\alpha > 0$ is a given constant and $f$ is a known probability density function. Equation [4] implies the liquid is below or at its freezing point, and hence why we call this the *supercooled* Stefan problem. Equation [1] models the heat diffusion in the fluid phase. Equation [2] states that the phase change at the front is isothermal. Equation [3] is the *Stefan condition*, which balances the heat flux through the freezing front with the exothermic heat release as the liquid freezes. This set of equations describes the *one-phase* problem, meaning that it assumes the temperature in the solid is constant and equal to $u = 0$. A solution to the SSP is the pair $(u, \Lambda)$ such that Equations [1]-[4] are satisfied.

In this supercooled setting, despite living only in one dimension, the Stefan problem for the heat equation gives rise to singularities (in the sense that the velocity of the free boundary explodes in finite time). This corresponds to the "rapid freezing" of supercooled liquids observed experimentally. Still, for an appropriate notion of solutions for 1SSP (i.e., the "probabilistic solution"), global existence and uniqueness of such solutions have been recently shown in (1). The probabilistic reformulation of 1SSP corresponds to a 1-dimensional MDLA process described above.

Motivated by this connection between MDLA and 1SSP in one space dimension, we explore the possible connection between a suitable version of MDLA and 1SSP for the heat equation in two spatial dimensions. Our approach throughout is numerical. We simulate the two-dimensional MDLA process on integer grids with finer and finer mesh. We study whether the resulting clusters satisfy certain properties that (suitably defined probabilistic) solutions to 1SSP in two space dimensions ought to satisfy.

## An MDLA process suitable for 1SSP in two spatial dimensions

We now consider an appropriate formulation of the MDLA process with connections to 1SSP. With this model defined, we will empirically confirm theoeretical predictions about the properties of this model's large population limit. To introduce this MDLA process, we consider the assumptions made by the classical DLA model that are inconsistent with the physics underlying 1SSP:

1. The seed is a *single infinitesimal particle.*
2. The cluster growth process terminates once the cluster attains some satisfactory size.
3. Particles are released, randomly walk, and are attached *one at a time.*
4. Particles are "removed" when they drift too far from the cluster.

To amend these assumptions and formulate an algorithm modeling solutions to 1SSP in two space dimensions, we introduce the new set up as follows.

Denote the set of points belonging to the cluster as $\Lambda_t^N$ on the $N \times N$ grid $\Gamma^N$, and denote the seed $\Lambda_0$. To store this data, we use an $N \times N$ matrix $A$ to represent $\Gamma^N$. Any point $(x, y) \in \Gamma^N$ corresponds to the entry at row $y$, column $x$ in $A$. Entries $A_{y,x}$ corresponding to sites $(x, y)$ which belong to the cluster $\Lambda_t^N$ are filled with a value of 1, and all other entries a value of 0.

In the classical setting, $\Lambda_0$ is the singleton set consisting of one seed particle of negligible volume. In the Stefan setting, $\Lambda_0$ has a strictly positive volume and therefore consists of more than one particle. If $\Lambda_0$ contains $P$ particles, then we say $P = kN^2$ for some $k \in (0, 1)$. To see how the shape of $\Lambda_0$ influences the terminal shape of $\Lambda_t^N$, we study three different types of $\Lambda_0$ seed clusters: circle, square, and cross. Note that for a circular seed cluster, the radius $r$ of a circular seed is given by

$$r^2 = \frac{kN^2}{\pi}.$$

Instead of releasing particles and walking them one-by-one, we now release $M$ particles on $\Gamma^N/\Lambda_0$ at time $t = 0$ all at once. For each site $(x, y) \in \Gamma^N \setminus \Lambda_0$, we place a particle at $(x, y)$ with probability $p$. Each particle follows a symmetric nearest-neighbor random walk as they do in classical DLA, but here we enforce two additional properties on this random

walk. Firstly, we require the particles to follow a random walk with *exclusion*, by which we mean no two particles are permitted to occupy the same site at the same time. If a particle attempts to step into an occupied site, it stays put. Secondly, we require particles to follow a random walk with *reflection* at the boundary of $\Gamma^N$ : if a particle attempts to step outside $\Gamma^N$, it stays put. The cluster growth process terminates at time $t = TN^2$ or when all of the $M$ particles released at $t = 0$ have attached to $\Lambda_t^N$, whichever occurs first.

In the next section we numerically study the properties of the terminal cluster $\Lambda_{N^2T}^N$ as $N \to \infty$. To implement the model for increasing $N$, we fix integers $N_0 > 0$ and $N^* > N_0$. We run the model for each integer $N \in [N_0, N^*]$. This algorithm is shown in Algorithm 2.

**Algorithm 2:** Modified DLA, circular seed cluster.

**Input:** $N_0$, $N^*$, $T$, $p \in (0,1)$, $k \in (0,1)$
**for** $N \in [N_0, N^*]$ **do**
  Initialize an $N \times N$ matrix $A$ of zeros.
  For all entries $A_{i,j}$ of matrix $A$, if the Euclidean distance between $(j,i)$ and $(N/2, N/2)$ is less than $kN^2/\pi$, set $A_{i,j} = 1$.
  Let $B$ denote the set of all the sites $(j,i)$ for which $A_{i,j} = 0$ (this is the set $\Gamma^N \setminus \Lambda_0$.) For each $(j,i) \in B$, with probability $p$ set $A_{i,j} = 2$. Let $P$ be the set of all such sites. Denote $M = |P|$.
  Set $t = 0, m = 0$.
  **while** $t < TN^2$ *and* $m < M$ **do**
    **for** $p = (x,y) \in P$ **do**
      $p$ takes a step to $p^* = (x^*, y^*)$ according to the nearest-neighbor symmetric reflected random walk with exclusion. If this $p^*$ is unoccupied, $p$ steps to $p^*$.
      **if** $p^*$ *is adjacent to a site in* $\Lambda_t^N$ **then**
        Observe that it is possible for particles to be in positions adjacent to $p^*$ at the time of attachment. Denote $\tilde{P}^*$ the collection of particles connected to $p^*$. Once $p^*$ is attached to $\Lambda_t^N$, all the particles in $\tilde{P}^*$ must also be attached since they are instantaneously connected to $\Lambda_t^N$.
        To attach all of the particles connected to $p^*$, we use the `flood-fill` algorithm to identify which positions are connected to $p^*$ and store them in $\tilde{P}^*$.
        **for** $\tilde{p} = (\tilde{x}, \tilde{y}) \in \tilde{P}^* \cup \{p^*\}$ **do**
          Attach $\tilde{p}$ to $\Lambda_t^N$ by setting $A_{\tilde{y},\tilde{x}} = 1$ and $A_{y,x} = 0$.
        **end**
        $m = m + 1$
    **end**
    $t = t + 1$
  **end**
**end**

Each of the terminal clusters showed in Figure 2 were produced using Algorithm 2 for various seed shapes. These clusters were formed for $k = 0.01, T = 0.01$, and $p = 0.25$. We see that for each initial seed shape, the shape of the terminal clusters $\Lambda_{N^2T}^N$ is similar: fractal-like "branches" form on the seed. This

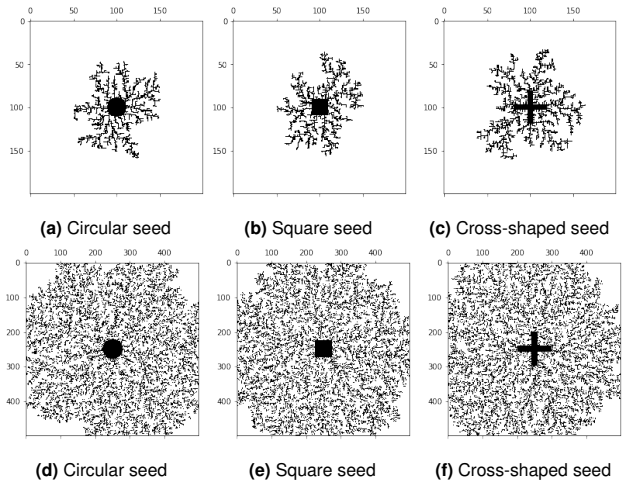

**(a)** Circular seed **(b)** Square seed **(c)** Cross-shaped seed

**(d)** Circular seed **(e)** Square seed **(f)** Cross-shaped seed

**Fig. 2.** Terminal clusters at $N = 200$ (top row) and $N = 500$ (bottom row).

type of cluster is what we would expect for the classical DLA model with a positive-volume seed. Note as well that there does not appear to be any obvious difference in the shape of $\Lambda_{N^2T}^N$ for different shapes of $\Lambda_0$. In particular, Figure 2f implies that the qualitative structure of the terminal clusters $\Lambda_{N^2T}^N$ does not depend on the convexity of the seed $\Lambda_0$.

## $\Lambda_{N^2T}^N$ as $N \to \infty$ : random or deterministic limit?

In the previous section we saw an indication that the shape of the terminal cluster $\Lambda_{N^2T}^N$ is invariant with respect to the shape of the seed $\Lambda_0$ (see Figure 2). In this section, we test whether the limit $\Lambda_T = \lim_{N\to\infty} \Lambda_{N^2T}^N$ is random or deterministic. The result in (1) proves the existence of this limit in the weak sense, but it is unclear whether this limit is random or deterministic. Ongoing research predicts the limit is random. To test this hypothesis numerically, we perform the following experiment.

Fix a number $S$ of Monte Carlo simulations and fix two reference points

$$x_c, x_s \in \Gamma^N \setminus \Lambda_0.$$

Reference point $x_c$ is positioned near the corner of $\Gamma^N$ at coordinate $(.95N, .95N)$, and reference point $x_s$ is positioned towards the side of of $\Gamma^N$ at coordinate $(.95N, .50N)$. Let $d(\cdot,\cdot)$ be the $L^1$ distance function. Fix a step size $z$. We run the cluster growth simulation $S$ times and for each $N = N_0, N_0 + z, N_0 + 2z, \ldots$ we plot the histogram of the distances from $x_s$ and $x_c$ to $\Lambda_{N^2T}^N$. Since the length of a cell's edge on $\Gamma^N$ is $1/N$, the "physical" distance from $x = x_c, x_s$ to $\Lambda_{N^2T}^N$ is calculated as

$$d(x, \Lambda_{N^2T}^N) = \frac{1}{N} \inf_{p \in \Lambda_{N^2T}^N} d(x,p).$$

Similarly, for each $N$ and for each sensor we also plot the distance sample mean

$$\hat{\mu}_d = \frac{1}{S} \sum_{i=1}^{S} d(x, \Lambda_{N^2T}^N),$$

and sample variance

$$\hat{\sigma}_d^2 = \frac{1}{S-1} \sum_{i=1}^{S} \left( d(x, \Lambda_{N^2T}^N) - \hat{\mu}_d \right)^2$$

as functions of $N$.

If $\hat{\sigma}_d^2$ appears to converge to 0 for both sensors, or equivalently if the histograms appear to converge to a Dirac mass, then we can conclude that the limit of $\Lambda^N_{N^2T}$ is deterministic. Otherwise the limit is random.

**Experiment results for a circular seed cluster.** Our experiment uses $S = 10$ simulations and $N$ ranges from $N_0 = 100$ through $N^* = 500$ with a step size of $z = 10$. We set $k = 0.01, T = 0.01$, and $p = 0.25$. Figure 3 shows the results of the experiment for the sensor $x_s$ and Figure 4 shows the results for sensor $x_c$.

For both sensors, the histograms of the distance samples do not suggest convergence to a Dirac mass. Whereas the variance plot for sensor $x_s$ appears to converge to 0 as $N$ increases, the variance plot for sensor $x_c$ does not appear to converge to zero. Therefore the results of this experiment indicate that the limit of $\Lambda^N_{N^2T}$ as $N \to \infty$ is random.

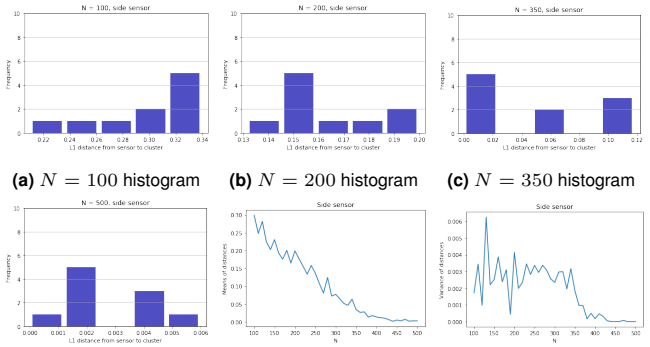


**(a)** $N = 100$ histogram **(b)** $N = 200$ histogram **(c)** $N = 350$ histogram

**(d)** $N = 500$ histogram **(e)** Sample means **(f)** Sample variances

**Fig. 3.** Side sensor $x_s$: distance histograms, sample mean and variance plots.

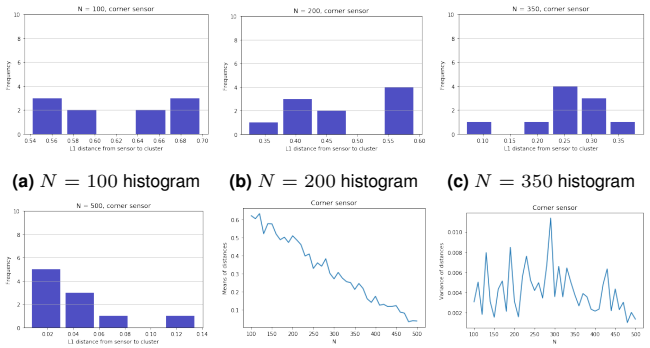


**(a)** $N = 100$ histogram **(b)** $N = 200$ histogram **(c)** $N = 350$ histogram

**(d)** $N = 500$ histogram **(e)** Sample means **(f)** Sample variances

**Fig. 4.** Corner sensor $x_c$: distance histograms, sample mean and variance plots.

The difference of the results for each sensor deserves attention. The sample mean plots show that the distance from $x_s$ to the cluster goes to zero much quicker than it does for $x_c$. This is evidenced in Figure 2. In the bottom row, the images indicate that the cluster spreads to the side of the grid before it spreads into the corner. There is a sense in which it is "more difficult" for the cluster to grow into the corner of the grid than it is for the cluster to grow to the side.

## Properties of $\Lambda_T = \lim_{N\to\infty} \Lambda^N_{N^2T}$

If $\Lambda_T = \lim_{N\to\infty} \Lambda^N_{N^2T}$ is a classical solution to the super-cooled Stefan problem in two dimensions, there are certain properties we expect $\Lambda_T$ to have. These properties are outlined below:

a.) Since particles aggregate to the cluster randomly, situations may occur when a small "hole" is created in the cluster and is never filled with a particle. For $\Lambda_T$ to solve the super-cooled Stefan problem in dimension two in the classical sense, the total limiting volume of these holes should be negligible. In dimension one, such holes are impossible. However, new results indicate that in dimension two, the total limiting volume of these holes may not be negligible.

b.) The length of the boundary of $\Lambda^N_{N^2T}$ does not explode as $N \to \infty$. Likewise, the volume of the cells comprising this boundary does not explode.

In the consideration of this boundary, we introduce two different notions of the boundary. Denote with $\partial\Lambda^N_{N^2T}$ the usual topological boundary. We also consider $\overline{\partial}\Lambda^N_{N^2T}$, the "external" boundary of $\Lambda^N_{N^2T}$. The external boundary is defined as

$$\overline{\partial}\Lambda^N_{N^2T} = \partial\Lambda^N_{N^2T} \setminus \partial H^N_{N^2T},$$

where $H^N_{N^2T}$ is the set of holes in the cluster $\Lambda^N_{N^2T}$. For example, the external boundary is the boundary of the cluster in Figure 4 excluding the ten edges lining the holes.

c.) Since the boundary of the grid $\Gamma^N$ and the seed $\Lambda_0$ are symmetric, we expect the limiting cluster $\Lambda_T$ to also be symmetric.

In this section we numerically test each of these properties to determine whether $\Lambda_T$ forms a solution to the super-cooled Stefan problem.

We can test (a) and (b) together with the same procedure, stemming from a simple observation. The following figure represents the matrix $A$ from Algorithm 2 where the 1s indicate particles belonging to $\Lambda^N_{N^2T}$, and blank spaces are 0s.

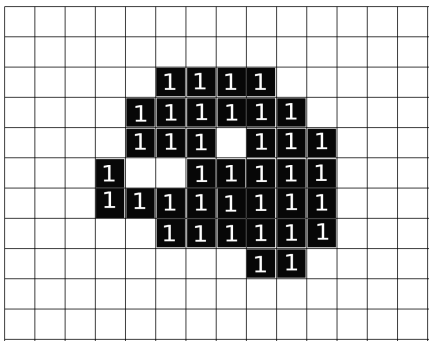

**Fig. 5.** Example of a cluster with holes of different size.

Note that $\partial\Lambda^N_{N^2T}$ is comprised of the edges on the exterior of the cluster and the edges lining the interior holes. To compute the length of this boundary, we must count the number of these edges. Let $E^N$ denote the value of this count. Let $E_{ij}$ be

the of edges of the cell associated to entry $A_{ij}$ which contribute to $\partial\Lambda^N_{N^2T}$. We can compute $E_{ij}$ using

$$E_{ij} = 4 - \sum(\text{adjacent entries}),$$

where the adjacent entries are the entries representing cells above, below, to the right, and to the left. For example, consider the bottom-right-most cluster cell. This cell has neighbors of value 1 above and to the left, and neighbors of value 0 below and to the right. Thus it contributes $E_{ij} = 2$ edges to $\partial\Lambda^N_{N^2T}$, verified by the picture. It is clear that

$$|\partial\Lambda^N_{N^2T}| = E^N = \sum_{i,j} E_{ij}.$$

Note that $|\overline{\partial}\Lambda^N_{N^2T}| \leq |\partial\Lambda^N_{N^2T}|$, where equality holds when there are no holes in $\Lambda^N_{N^2T}$ and the inequality is strict when there are holes. To count the edges that contribute only to $\overline{\partial}\Lambda^N_{N^2T}$, we need to modify the procedure above.

We begin by "filling" all the holes with a well-chosen value. Everywhere in matrix $A$ where entries correspond to holes in $\Lambda^N_{N^2T}$, we fill these entries with $-1$. Then for each entry $A_{ij}$, we compute $E_{ij}$ similarly as above, but here we take the absolute value of each adjacent entry:

$$\overline{E}_{ij} = 4 - \sum |\text{adjacent entries}|$$

so that

$$|\overline{\partial}\Lambda^N_{N^2T}| = \overline{E}^N = \sum_{i,j} \overline{E}_{ij}.$$

The normalized values $L^N_{\partial\Lambda} = E^N/N$ and $\overline{L}^N_{\partial\Lambda} = \overline{E}^N/N$ give the lengths of the boundary and external boundary, respectively.

To fill the holes, we utilize the so-called "flood-fill" algorithm. The flood-fill algorithm is used to determine the area connected to a given node in a multi-dimensional array. An example of its application is the "bucket" fill tool in digital painting programs used to fill connected areas of a similar coloring with a different color. In our setting, the flood fill algorithm fills connected areas in matrix $A$ which have similar values. We choose entry $A_{0,0} = 0$ as the initial input to the flood-fill algorithm. The algorithm changes this value to $A_{0,0} = -1$. It then checks the values of neighboring entries $A_{1,0}$ and $A_{0,1}$. If these entries are equal to 0, it changes them to $-1$. The process repeats for each $A_{1,0}$ and $A_{0,1}$ and so on until the entire area of entries connected to $A_{0,0}$ initially having value 0, now have value $-1$.

To illustrate the application of flood-fill, observe that one application of flood-fill to Figure 4 changes all cells with value 0 exterior to the cluster to $-1$. Then, we set all remaining entries of $A$ with value 0 to $-1$. These entries of value 0 that were not changed by flood-fill are the holes themselves, as they are not connected to $A_{0,0}$. Now that all the holes have value $-1$, what remains is to change the values of $-1$ exterior to the cluster back to 0. To do this, we apply flood-fill again to entry $A_{0,0} = -1$, this time specifying that the algorithm change all values of $-1$ to 0. The result is a matrix $A^*$ whose entries representing holes in the cluster $\Lambda^N_{N^2T}$ have been filled with $-1$.

We also want to compute the volume of cells on $\partial\Lambda^N_{N^2T}$. To do this, we need a count of how many cells live on the boundary $\partial\Lambda^N_{N^2T}$, and then we make an appropriate normalization for the physical volume. For each entry $A_{ij}$ in matrix $A$, we check the following conditions. If at least one of them holds then entry $A_{ij}$ lives on the boundary of $\Lambda^N_{N^2T}$ :

1. $A_{i+1,j} = 1$ and $A_{i-1,j} = 0$,
2. $A_{i-1,j} = 1$ and $A_{i+1,j} = 0$,
3. $A_{i,j+1} = 1$ and $A_{i,j-1} = 0$,
4. $A_{i,j-1} = 1$ and $A_{i,j+1} = 0$.

The first condition says that the position below $A_{ij}$ is a cluster particle and the position above $A_{ij}$ is an empty cell, the second condition is the converse, and the third and fourth conditions are analogous but for positions left and right of $A_{ij}$. It is is clear that if any one of these hold, $A_{ij}$ must be on the boundary of $\Lambda^N_{N^2T}$. To compute the physical volume of these boundary cells, if $B^N$ denotes the number of cells on the boundary $\partial\Lambda^N_{N^2T}$ then the volume of the boundary is

$$V^N_{\partial\Lambda} = \frac{1}{N^2} B^N.$$

In the course of filling holes, we may also keep count of how many holes are filled. In this way, we determine the number of holes $H^N$ in $\Lambda^N_{N^2T}$. To compute the physical volume of these holes, we take

$$V^N_{\text{holes}} = \frac{1}{N^2} H^N.$$

To test for the symmetry of $\Lambda_T$, for each $N$ we take the 90 degree counterclockwise rotation of $\Lambda^N_{N^2T}$, then compute the volume of the particles in the symmetric difference between $\Lambda^N_{N^2T}$ and its rotated counterpart. If this volume converges to 0 as a function of $N$, we conclude that $\Lambda_T$ is symmetric. More explicitly, denote $\text{rot}(\Lambda^N_{N^2T})$ the $+90$ degree rotation of $\Lambda^N_{N^2T}$. For each $N$, count the number of particles in the symmetric difference

$$D^N = |\Lambda^N_{N^2T} \triangle \text{rot}(\Lambda^N_{N^2T})|,$$

so that the volume of the particles in this symmetric difference is given by

$$V^N_{\text{diff}} = \frac{1}{N^2} D^N.$$

Testing (a), (b), and (c) amounts to plotting $L^N_{\partial\Lambda}, \overline{L}^N_{\partial\Lambda}, V^N_{\partial\Lambda}$, $V^N_{\text{holes}}$, and $V^N_{\text{diff}}$ as functions of $N$. The results of these tests with the same parameters as the experiment in Section 3.1 are shown in Figure 6. Figure 6-(a) and (b) demonstrate that the length of the boundary of $\Lambda_T$ explodes as a function of $N$. Figure 6-(d) indicates that the holes constitute a non-negligible volume in the limiting cluster $\Lambda_T$. The spiking of the graphs in (b) and (d) is due to how particles are attached in Algorithm 2. When a particle enters a position adjacent to the cluster, if there are particles connected to this adjacent site, then all the particles attach instantly. This result in large "pockets" of holes forming in the cluster, producing sharp up-spikes in hole volume and a corresponding down-spikes in the external boundary length. Nevertheless, it is clear that the experiment confirms theoretical conclusions that the holes in the two dimensional cluster growth process constitute a non-negligible volume. Likewise, Figure 5-(e) suggests the volume of particles in $\Lambda^N_{N^2T} \triangle \text{rot}(\Lambda^N_{N^2T})$ is strictly positive as $N \to \infty$. This means that the symmetry of the seed cluster $\Lambda_0$ is not preserved in the cluster growth process as $N$ increases. In particular,

these results imply that *the MDLA model considered here does not converge to solutions of 1SSP in two space dimensions.*

Note that Figure 6 also includes a plot of first exit times. These are the times $t \in [0, TN^2]$ for which the cluster first contacts the boundary of $\Gamma^N$. The decreasing trend of these exit times suggests that the cluster fills $\Gamma^N$ instantaneously in the limit as $N \to \infty$.

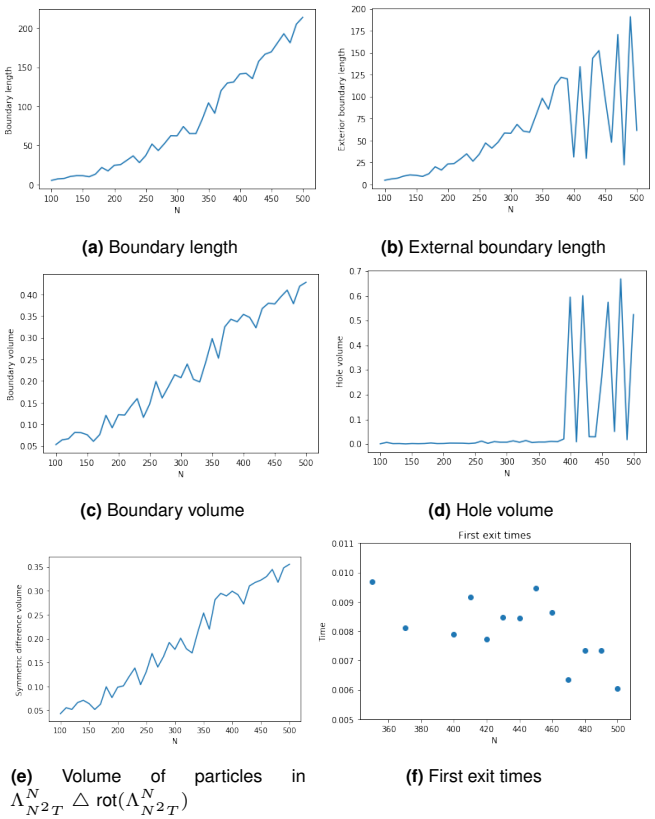


**(a)** Boundary length **(b)** External boundary length

**(c)** Boundary volume **(d)** Hole volume

**(e)** Volume of particles in $\Lambda^N_{N^2T} \triangle \text{rot}(\Lambda^N_{N^2T})$ **(f)** First exit times

**Fig. 6.** Test results for properties (a), (b), and (c).

## Conclusion

Our statistical analysis of 2-dimensional MDLA terminal aggregates shows that the MDLA process defined herein does not converge to probabilistic solutions of 1SSP in two space dimensions. In particular, the presence of a non-negligible hole volume in terminal aggregates grown on grids with a fine mesh and that these terminal aggregates do not appear to converge to deterministic structures disqualify $\lim_{N\to\infty} \Lambda^N_{N^2T}$ as a probabilistic solution to 1SSP in two space dimensions. An unexpected consequence of this work is an observation obtained from Figure 6(f). This plot indicates that the terminal cluster first exit times go to 0 as $N \to \infty$. In other words, we conjecture that terminal clusters spread to the boundary of $\Gamma^N$ instantaneously in the limit as $N \to \infty$.

Although MDLA clusters do not appear to converge to solutions of 1SSP in two space dimensions, it is possible that modifications may be made to the MDLA process studied here such that the terminal clusters do not have the numerous undesirable properties identified in our simulations. In particular, if it is possible to introduce a feature to the MDLA process that results in a more regular and less fractal-like terminal cluster boundary, and if it is possible to limit the possibility of interior hole formation, such a process may produce limiting clusters that do indeed converge to solutions.

## References


1. F. Delarue, S. Nadtochiy, and M. Shkolnikov, *Global solutions to the supercooled stefan problem with blow-ups: regularity and uniqueness*, arXiv preprint arXiv:1902.05174, (2019).
2. A. Dembo and L.-C. Tsai, *Criticality of a randomly-driven front*, Archive for Rational Mechanics and Analysis, 233 (2019), pp. 643–699.
3. D. M. Eberz-Wagner, *Discrete growth models*, arXiv preprint math/9908030, (1999).
4. M. B. Hastings and L. S. Levitov, *Laplacian growth as one-dimensional turbulence*, Physica D: Nonlinear Phenomena, 116 (1998), pp. 244–252.
5. P. Meakin, *Formation of fractal clusters and networks by irreversible diffusion-limited aggregation*, Physical Review Letters, 51 (1983), p. 1119.
6. ———, *Multiparticle diffusion-limited aggregation with strip geometry*, Physica A: Statistical Mechanics and its Applications, 153 (1988), pp. 1–19.
7. H. B. Rosenstock and C. L. Marquardt, *Cluster formation in two-dimensional random walks: application to photolysis of silver halides*, Physical Review B, 22 (1980), p. 5797.
8. L. M. Sander, *Diffusion-limited aggregation: a kinetic critical phenomenon?*, Contemporary Physics, 41 (2000), pp. 203–218.
9. R. F. Voss, *Multiparticle diffusive fractal aggregation*, Physical Review B, 30 (1984), p. 334.
10. ———, *Multiparticle fractal aggregation*, Journal of Statistical Physics, 36 (1984), pp. 861–872.
11. T. Witten Jr and L. M. Sander, *Diffusion-limited aggregation, a kinetic critical phenomenon*, Physical review letters, 47 (1981), p. 1400.

# A Gröbner Basis Database

**Jelena Mojsilović**[1]

[1]Department of Applied Mathematics, Illinois Institute of Technology

**In response to the increased interest in machine learning to solve mathematical problems combined with the complexity inherent in computing Gröbner bases, we create a Gröbner basis database. Through this database we aim to provide a platform where researchers and practitioners can: obtain accurate and verified data on Gröbner bases, submit interesting and important examples of Gröbner bases, and obtain curated datasets for benchmarking, learning, and other common problems in the research community. Given the nascent stage of the database, new features are likely to be added on as it grows.**

Gröbner bases are an approach to answering the *ideal membership problem* arising from computational algebraic geometry. Before we explain what this is, let us first define an ideal. An ideal, $I$, is a subset $I \subset k[x_1, ..., x_n]$ that satisfies:

1. $0 \in I$
2. If $f, g \in I$, then $f + g \in I$.
3. If $f \in I$ and $h \in k[x_1, ..., x_n]$, then $hf \in I$.

Thus, an ideal $I$ is an infinite collection of polynomials and the ideal membership problem is to determine whether a polynomial $f$ lies in an ideal $I$. An analogous problem in linear algebra would be determining if a vector, $v$, lies in a subspace $V$. The solution to the linear algebra problem is also analogous to the solution of the ideal membership problem. The standard method in linear algebra is to find a basis for $V$ and attempt to find if $H_V x = v$ has a solution $x$, where $H_V$ is the matrix whose columns consist of the basis. The approach in computational algebraic geometry begins with finding a finite basis for the ideal. The Hilbert Basis Theorem tells us that every ideal $I \subset k[x_1, ..., x_n]$ has a finite basis. We denote this as $I = \langle f_1, ..., f_s \rangle$, . That is, every polynomial $g \in I$ can be expressed as: $g = h_1 f_1 + h_2 f_2 + ... + h_s f_s$ for some set $\{h_1, ..., h_s\} \subset k[x_1, ..., x_n]$.

A problem arises from this definition: If we are given a polynomial, $f$, how do we determine whether $f \in I$? This is synonymous with the ideal membership problem.

## The Division Algorithm

The division algorithm provides a partial solution to the ideal membership problem, regardless of the basis.

Fix a monomial order $>$. Let $F = (f_1, ..., f_n)$ be an ordered s-tuple of polynomials in $k[x_1, ..., x_n]$. Then every $f \in k[x_1, ..., x_n]$ can be expressed as $f = a_1 f_1 + ... + a_s f_s + r$ where $a_i, r \in k[x_1, ..., x_n]$.

Combining the division algorithm with the ideal membership problem, we see that a polynomial $f \in I$ if $r = 0$. However, the division algorithm does not specify in which order the divisors must be utilized. This allows the remainder upon division to differ depending on the ordering of divisors. The example in Figure 1 is a demonstration of this, determining whether $f = xy^3 + y + 1 \in \langle xy^2 + 1, x + y \rangle$.


**Fig. 1.** The division algorithm dividing $xy^3 + y + 1$ by the set $\{x + y, xy^2 + 1\}$, utilizing two orderings on the divisors $(xy^2 + 1, x + y)$ and $(x + y, xy^2 + 1)$, yields two different remainders.

This property is problematic because the ordering of divisors does not provide a unique remainder. We want a basis that retains the property that the ordering of divisors does not change the remainder. We must ask: is there a better basis for $I$ such that the remainder, $r$, is uniquely determined? A Gröbner basis is such a basis.

## Gröbner Bases

A Gröbner basis is a generating set of an ideal in a polynomial ring, $k[x_1, ..., x_n]$, over a field, k. More formally letting LT denote the leading term of a polynomial, this basis is defined as follows.

**Definition 1** Under a specific term order, a finite subset $G = \{g_1, ..., g_t\}$ of an ideal $I$ is said to be a **Gröbner basis** if $\langle LT(g_1), .., LT(g_t) \rangle = \langle LT(I) \rangle$.

A consequence of this definition is that every non-zero ideal has a Gröbner basis. The following two properties of a Gröbner basis allow for it to be the generating set for $I$ that we are looking for.

**Theorem 1** *Let $G = \{g_1, ..., g_t\}$ be a Gröbner basis for an ideal $I \subset k[x_1, ..., x_n]$ and let $f \in k[x_1, ..., x_n]$. Then there is a unique remainder, $r \in k[x_1, ..., x_n]$ with the following two properties.*

1. *No term of $r$ is divisible by any of $LT(g_1), ..., LT(g_t)$.*
2. *There is $g \in I$ such that $f = g + r$.*

*In particular, $r$ is the remainder on division of $f$ by $G$ no matter how the elements of $G$ are listed when using the division algorithm.*

For this reason, Gröbner bases solve the problem of finding a solution to a multivariate, non-linear system of polynomials.

**Computation and Application of Gröbner Bases .** Gröbner bases are a cornerstone of computation with polynomials and have a wide variety of applications such as robotics, engineering, statistics, and biology. Gröbner bases provide a solution to an EXSPACE hard ideal membership problem, which can be reduced to the word equivalence problem [2].

**A Gröbner Basis Database.** Given the complexity of Gröbner bases combined with an increase in interest using machine learning to solve mathematical problems, a Gröbner basis database would provide the research community with a robust set of Gröbner basis data. The goal of the database is two-fold: to generate a set for potential future learning, and to provide a way for researchers to cross reference to see if their physical problem is equivalent to some other known problem.

## Methods

To create the database, we use MySQL in order to form a table of rows and columns. Each column is one of seventeen fields: starting generating set, reduced Gröbner basis, field, term order, number of variables, size of the reduced GB, max total degree, min total degree, max multi-degree, min multi-degree, minimum number of generators, code, name, description, submission by, verified by, and submission date. These fields are chosen because they are well-defined properties of Gröbner bases.

The database is connected to a website, Groebner Basis Database, where users can find a search function to query the database, pre-made datasets for machine learning, benchmarking problems, and programming, as well as a submissions page in order to submit their own Gröbner basis data. In addition to inputting our own Gröbner basis data, we encourage others to submit data so that we can have a robust dataset. Our database can be found at: http://math.iit.edu/~groebnerdatabase/index.html.

**Fields of the Database.** All of the mathematical definitions below are taken from [1] before the list begins.

- Starting Generating Set: We organize our database by the starting generating set because it defines the polynomial system from which we will construct a (reduced) Gröbner basis.
- Reduced Gröbner Basis: A **reduced Gröbner basis** for a polynomial ideal $I$ is a Gröbner basis $G$ for $I$ such that:
  - LC(p)= 1 for all $p \in G$, where $LC(p)$ denotes the leading constant of the polynomial $p$.
  - For all $p \in G$, no monomial of p lies in $\langle LT(G - \{p\}\rangle$.

  We choose to include the reduced Gröbner basis because it is unique given a monomial ordering. Thus for any two ideals, in order to verify if they have the same basis given a monomial order, in fact, to determine whether they are the same ideal, a reduced Gröbner basis must be found.
- Field: The field of coefficients overwhich a Gröbner basis is calculated must be specified by definition.
- Term Order: A **term order** on $k = [x_1, ..., x_n]$ is any relation on $Z^n_{\geq 0}$, or equivalently, any relation on the set of monomials $x^\alpha$ satisfying:
  - $>$ is a total (linear) ordering on $Z^n_{\geq 0}$;
  - if $\alpha > \beta$ and $\gamma \in Z^n_{\geq 0}$, then $\alpha + \gamma > \beta + \gamma$;
  - $>$ is a well-ordering on $Z^n_{\geq 0}$. In other words, every nonempty subset of $Z^n_{\geq 0}$ has a smallest element under $>$.

  A term order is necessary in order to compute a Gröbner basis by definition, thus it must be included as a field in our database. For every term order, we standardize the variables. For example, for a system given in $(x, y, z)$ we convert the system to $x_1, x_2, x_3$. This is done in order to prevent double entries in the database of the type that have the same initial generating set and same reduced Gröbner basis.
- Size of the Reduced Gröbner Basis: The size of the reduced Gröbner basis does change depending on term order. This information could distinguish the same ideal double-entered into the database whose Gröbner bases are calculated under different term orders.
- Maximum Total Degree: For a given monomial order, the maximum of the degrees of the polynomials in the Gröbner basis, where the **degree** of a polynomial $p$ whose leading term is $LT(p) = c_\alpha x_1^{\alpha_1} \dots x_n^{\alpha_n}$ is defined to be $deg(p) = \alpha_1 + \dots + \alpha_n$, is $maxdeg(g_1), ..., deg(g_t)$.
- Minimum Total Degree: For a given monomial order, the minimum of the degrees of the polynomials in the Gröbner basis, where the **degree** of a polynomial $p$ whose leading term is $LT(p) = c_\alpha x_1^{\alpha_1} \dots x_n^{\alpha_n}$ is defined to be $deg(p) = \alpha_1 + \dots + \alpha_n$, is $mindeg(g_1), ..., deg(g_t)$.
- Maximum Multidegree: For a given monomial order, the maximum of the multidegrees of the polynomials in the Gröbner basis, where the **multidegree** of a polynomial $p$ whose leading term is $LT(p) = c_\alpha x_1^{\alpha_1} \dots x_n^{\alpha_n}$ is defined to be the vector $deg(p) = (\alpha_1, \dots, \alpha_n)$, is the vector $MaxMdeg = (max\{\alpha_{11}, \dots, \alpha_{1t}\}, \dots, max\{\alpha_{n1}, \dots, \alpha_{nt}\})$
- Minimum Multidegree: For a given monomial order, the minimum of the multidegrees of the polynomials in the Gröbner basis, where the **multidegree** of a polynomial $p$ whose leading term is $LT(p) = c_\alpha x_1^{\alpha_1} \dots x_n^{\alpha_n}$ is defined to be the vector deg$(p) = (\alpha_1, \dots, \alpha_n)$, is the vector $MinMdeg = (min\{\alpha_{11}, \dots, \alpha_{1t}\}, \dots, min\{\alpha_{n1}, \dots, \alpha_{nt}\})$
- Minimum Number of Generators: We include the minimum number of generators because it specifies the size of the input system of polynomials.
- Code: For the time being this is not an active field. However, this field will become a source for users to find code for widely used programs, such as Macaulay2 or Sage, in order to perform calculations for a given entry in the database.
- Name: Name is an optional field which is included in order to provide the names of ideals which are more commonly known by some name.
- Verified By: The verified by field will allow the user to know that the data of an entry in the database has been checked for correctness.

**Current Method.** The small examples we have included for the start of the database were calculated in Macaulay2. Macaulay2 is open-source software devoted to supporting research in computational algebraic geometry and commutative algebra. Given the complexity of the problem, the future method of computation may differ.

## Discussion

This database is a long-term project that will require editing and maintenance over time. We hope this database will serve as a useful tool for the research community. As such, we encourage input from those who will use it in an effort to improve this database.

A major challenge in creating this database was determining what properties of Gröbner bases would be useful to the research community and if these properties should be included. Thus, we have to determine what the ideal database would be and what can be made realistically. We acknowledge that our database will not contain all properties of a Gröbner basis that may be used for research, but our database will contain those properties of a Gröbner basis that will be most often sought after by the research community.

## Conclusion

We have set the foundation of our database with a basic outline of what we want the database to contain. This database should be viewed as a major work in progress that will change over time. For our purposes, we hope to use the dataset we generate through this database in future work in machine learning on Gröbner bases.

**Future Work.** In the future we plan to work on handling user-generated datasets, creating an automated method of transferring uploads to the database, and user submission of data that is too complex for the automated database entry process. User generated datasets may contain missing information and most likely will require some calculations in order to fill null entries. The current method of adding entries into the database requires physical entry from a submission. This is inefficient and time costly. In the future, it would be more efficient to create an automated process so as to allow more time for handling more complex entries. Complex entries may take a large amount of time to handle, so these entries must be filtered out of the automation process. However, this does not solve the issue of how the data for these entries will be verified and/or calculated.

**ACKNOWLEDGMENTS.** This database is a joint work with Travis Koehring, Sonja Petrović, Despina Stasi, and Sara Jamshidi Zelenberg. We would like to thank the Applied Mathematics Department at the Illinois Institute of Technology for hosting our database. We would also like to thank Upendra Ghandi for his help and support in the creation of our database and website this past summer.

## References

[1] David A. Cox , John Little , Donal O'Shea, Ideals, Varieties, and Algorithms: An Introduction to Computational Algebraic Geometry and Commutative Algebra, Springer Publishing Company, Incorporated, 2015

[2] Earnst W. Mayer, Some Complexity Results for Polynomial Ideals, Journal of Complexity 13, 303-325, 1997

# The Immune System's Battle Against SARS-CoV-2

Maanav Agrawal, Caroline Mazur-Sarocka, Mahum Sheikh, Lillian Tang

Author Contacts: agrawalmaanav03@gmail.com, mazursarocka@gmail.com, msheikh254@gmail.com, lilliantang2003@gmail.com

*All Authors Contributed Equally

## I. ABSTRACT

The widespread public health and safety implications of the spread of SARS-CoV-2, a viral respiratory disease, have been witnessed worldwide. The immune system is an integral component in both the recovery progression and the severity of illness in individuals who contract coronavirus. Complications in the immune system due to SARS-CoV-2 have led to the development of Multisystem Inflammatory Syndrome in Children (MIS-C), which has shown to be a rare, but serious disease. MIS-C is a condition causing severe inflammation in children after exposure to COVID-19, with symptoms including vomiting, skin rash, and redness. In this paper, we consider the components of the coronavirus immune response on the progression of illness severity and the development of MIS-C.

## II. INTRODUCTION

The novel coronavirus 2019 (COVID 19) outbreak initially began in Wuhan, China in December of 2019. Due to phylogenetic similarities to severe acute respiratory bat viruses, bats have been connected to SARS-CoV-2 (COVID-19) as the primary reservoir host. Further investigations using molecular and phylogenetic analyses have determined a correlation between pangolin-CoV-2020 and SARS-CoV- 2. Although SARS-CoV-2 did not directly emerge from pangolin-CoV-2020, a genetic relationship has been linked between the pangolin virus and the coronavirus impacting the human population[1]. Through this conclusion and the indication of bats as the reservoir host which are similarly linked to pangolins, the intermediate host of SARS-CoV-2 has been hypothesized as the pangolin from which humans contracted the virus (Figure 1).

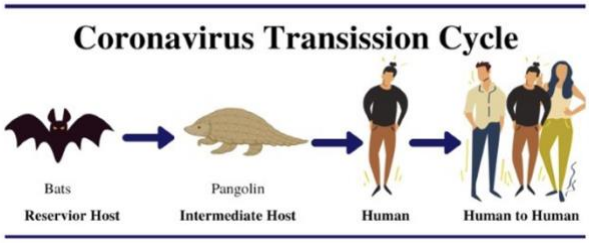


Based upon the phylogenetic correlations found between SARS-CoV-2, pangolin-CoV-2020, and similar SARS bat viruses, the hypothesized Coronavirus Transmission Cycle is pictured above.

Those infected with COVID-19 have presented a wide range in severity and associated symptoms, beginning two to fourteen days after initial viral exposure. Symptoms of lesser severity include: fever or chills, cough, shortness of breath or difficulty breathing, fatigue,
muscle or body aches, headache, new loss of taste or smell, sore throat, congestion or runny nose, nausea or vomiting, or diarrhea. Symptoms warranting immediate medical attention include: trouble breathing, persistent pain or pressure in the chest, new confusion, inability to wake or stay awake, or blue-tinted lips or face.[2] These symptoms vary among patients in regards to the effectiveness of their holistic immune response.

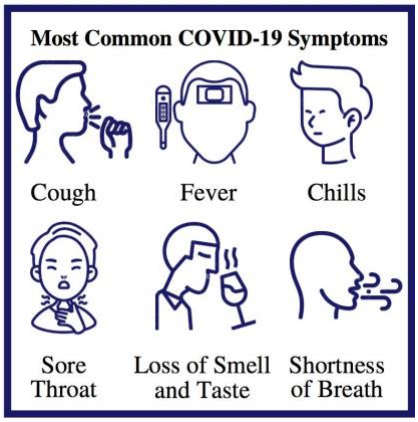


Even with emergency containment efforts after initial reports of human cases, the virus spread throughout

metropolitan areas of China and eventually cases emerged across the globe. The current rate of infection has continued to drastically increase in the United States, while substantially lessening in other countries such as New Zealand. As of November 21, 2020, the total number of US cases has surpassed 11.8 million and the cumulative number of deaths has risen to 253,600[3]. The positive rate of daily increase in cases indicates that the public health threat posed by COVID-19 continues to persist and will likely remain in the near future.

## III. INNATE VS ADAPTIVE IMMUNE SYSTEM

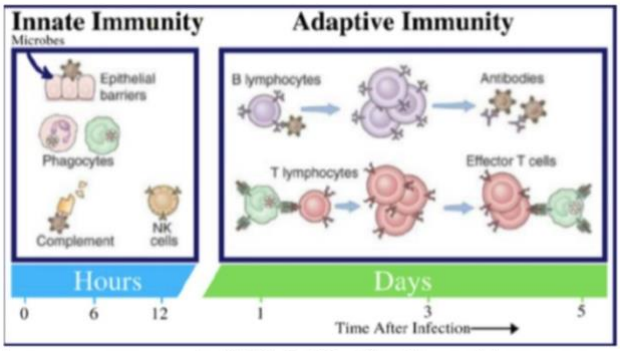


Immune responses to SARS-CoV-2 utilize the rapid response provided by innate immunity. The differences between the innate and adaptive immune responses are vastly evident as adaptive immunity mainly enables protection against antigens with B cells and T cells (both white blood cells). Whereas, the innate response is mainly for the incoming pathogen that appears on the surface of the skin or travels in depth into the airways. In those cases, phagocytes like monocytes, macrophages, neutrophils, and mast cells depicted above attack SARS-CoV-2 as "special" white blood cells. The similarity between these two responses lies with the natural killer cell which helps fight off the virus within the first few hours.

Individuals infected with SARS-CoV-2 have two types of immune systems to combat the disease and make up a possible recovery: the innate and adaptive immune response. The immune system's main role is to prevent or limit the spread of any sort of pathogenic germs or infectious substances detected on the skin, in the tissues of the body, or in bodily fluids.

The innate (general) immune system focuses directly on germs entering the body and is responsible for their elimination within 0-96 hours upon first contact. It is activated by the chemical properties of foreign antigens and includes cellular responses from macrophages, neutrophils, eosinophils, basophils, dendritic cells, and mast cells. It mainly offers protection through skin and mucous membranes as it provides a shield against antigens along with certain enzymes, defense cells, and killer white blood

attributed to T helper cells that "memorize" pathogenic antigens from previous infections. The T white blood cells activate the B lymphocytes, which produce abundant amounts of necessary antibodies that neutralize bacteria and viruses through the activation of certain enzymes[4].

The localization of both components of the immune system are vital as each location serves a purpose in initiating the immune system; protection is spread across the skin which is placed as the first line of defense against foreign substances or germs. Bone marrow contains stem cells, which develop into immune cells for the immune system to begin fighting the pathogens. The blood stream circulates these produced immune cells waiting for them to be recruited by the cytokines to attack the pathogens. The thymus is where T lymphocytes mature before fighting viruses. The lymphatic system and spleen acts as a communication hub between bloodstream and tissues, and immune cells activate and respond when pathogens are recognized[4]. The mucosal tissue is the main entry point for pathogens with immune hubs storing white blood cells. All these areas in which the immune system's components rest strengthens the effectiveness of the immune system response as different parts of the response come into action depending on where the foreign pathogens reach.

SARS-CoV-2 imposes a dysregulated immune response known as cytokine storm or cytokine-release syndrome in patients infected with SARS-CoV-2. The cytokine-release syndrome develops into severe acute respiratory

| Cytokines | Role | Symptoms |
|---|---|---|
| IL-1 | Regulates immune and inflammatory responses to infections | Inflammation, respiratory failure |
| IL-6 | Produced in response to tissue damage and infections | Inflammatory response, respiratory failure |
| IL-12 | Downregulates allergic inflammation when released | Generates specific cytotoxic CD8+ T cells |
| IFN-γ | Stimulates natural killer cells and neutrophils, activates macrophages, mediates antiviral and antibacterial immunity, enhances antigens | Risk factor for lung fibrosis |
| TNF-α | Produced by macrophages during acute inflammation and is responsible for a range of signaling events within cells during an infection | Potential factor of toxic epidermal necrolysis |

distress syndrome that pro-inflammatory cytokines, including IL-1α, IL-1β, IFN-α, IL-17A and IL-12 p70, inflict on the airway tract[5]. The presence of these cytokines has been reported in all patients infected with COVID-19. Furthermore, other cytokines including IFN-λ, thrombopoietin, IL-21, IL-23 and IL-33, were up-regulated in patients with severe symptoms of COVID-19. Moreover, these severe cases also reported molecules associated with defense response to viral infection released

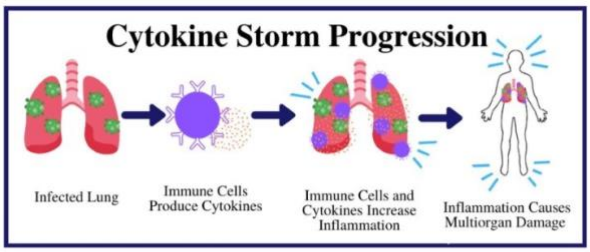


Caption: After SARS-CoV-2 infects the lungs, immune cells produce cytokines to try and restore homeostasis in the body. When the immune system doesn't respond properly, an accumulation of immune cells and cytokines results in the infection site. As these immune cells and cytokines continue to be produced, they become widespread throughout the body, causing inflammation and lung injury, eventually leading to multi-organ failure.

by a type of activated CD4 T-cell called a TH1 cell. Patients with severe disease from SARS-CoV-2 were associated with the activation of a protein complex called the inflammasome which results in an immune response that causes inflammation. IL-1Ra, a protein that normally inhibits excessive inflammasome function, was seen in these patients and this up-regulated molecule dampens the immune response making SARS-CoV-2 stronger than the immune system[5].

**IV. Healthy Versus Dysfunctional Immune Response**

A healthy adaptive immune response to SARS-CoV-2 would typically help decrease the viral load and cause minimal damage that eventually leads to recovery. Part of this process involves the production of pro-inflammatory cytokines by several immune cells including innate macrophages, dendritic cells, natural killer cells, and T and B lymphocytes that then recruits monocytes, macrophages, and T cells from the surrounding blood to the site of infection.[6] Typically, the infected cells are cleared before the virus spreads and circulating antibodies neutralize the virus. The neutralized viruses are then recognized by alveolar macrophages and engulfed by apoptotic cells.

On the other hand, if an immune response to SARS-CoV-2 is dysfunctional, there are too many pro-inflammatory cytokines produced. This in turn causes an excessive accumulation of monocytes, macrophages, and T cells, in addition to the pro-inflammatory cytokines.[6] This exaggerated immune response is known as the cytokine storm where large amounts of inflammation lead to multi-organ damage and other complications that could result in death. The understanding of specific pro- inflammatory cytokines involved in the cytokine storm aids in finding strategies that will increase the survival rates of patients with SARS-CoV-2.

**V. Types of Proinflammatory Cytokines**

Interleukin-6 (IL-6) is a type of cytokine that plays a prominent role in the cytokine storm associated with SARS-CoV-2.[7] More specifically, IL-6 regulates the acute phase response in which the body increases inflammation in order to restore homeostasis after the entry of the SARS-CoV-2 pathogen that binds to the ACE-2 receptor. IL-6 also may be responsible for activating CD4+ T cells, or Helper T cells. While these cells help activate B cells and CD8+ T cells that help to directly kill infected cells, they also cause more pro-inflammatory cytokines to be produced, which continues to exacerbate the cytokine storm that becomes widespread in the body.

| | |
|---|---|
| Interleukin-6 (IL-6) | Neuropathic Pain, Tactile Aldonyia |
| Tumor Necrosis Factor-Alpha | Hyperalgesia & Increased Pain Sensitivity |
| Chemokines | Neuropathic Pain, Neuroinflammation |

Elevated levels of IL-6 are associated with a higher rate of mortality and is the most commonly reported elevated level of cytokine in patients with SARS-CoV-2. Tumor Necrosis Factors are another type of cytokine that causes an inflammatory immune response and is responsible for producing Interleukins which have been identified as major pro-inflammatory cytokines. Other subgroups of cytokines that induce inflammation include chemokines which are unique due to how selective they are when recruiting immune cells to the site of infection.[7] Increased levels of any of these cytokines could be indicative of severe disease being present in the patient that needs to be treated immediately. The figure above highlights the associated symptoms that accompany increased levels of the aforementioned cytokines that are present both during initial infection and even have been identified after the patient no longer is infected.[14] In order to target these pro-inflammatory cytokines, strategies are being implemented in order to inhibit cytokines from attaching onto cytokine receptors on the surfaces of cells. The immunosuppressive drug Tocilizumab shown in the figure below targets Interleukin-6 to reverse the harmful effects of the cytokine storm.

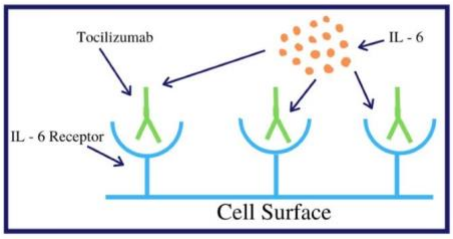


Caption: Tocilizumab, an immunosuppressive drug that has been approved by the FDA for use in severe COVID-19 pneumonia works by targeting Interleukin-6 (IL-6), a proinflammatory cytokine. Tocilizumab attaches to the IL-6 cytokine receptors on the surfaces of cells to stop the transduction pathway, preventing many of the harmful effects of the cytokine storm.

## VI. Multisystem Inflammatory Syndrome in Children

Multisystem Inflammatory Syndrome in children (MIS-C) is a condition in which causes severe inflammation on bodily parts including the heart, kidneys, digestive system,

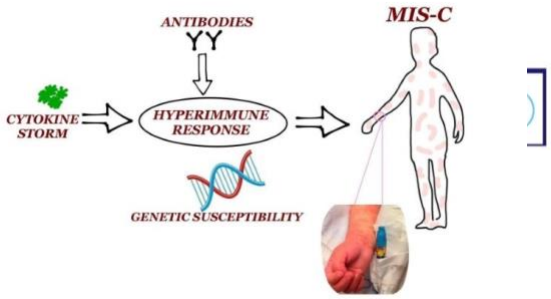


MIS-C occurs when there is a hyperimmune response, a high concentration of antibodies that are produced due to the presence of an antigen, in the body. As a result, in addition to the cytokine storm and the build-up of antibodies, it results in an inflammatory response that prompts severe reactions to the body. Inflammation of organs as well as failure of them acn result. Research is still being conducted in order to understand more about genetic susceptibility and how this correlates with the severity of MIS-C, as certain genetic factors may make individuals predisposed to this condition. ***Inspired by a graphic by the MDPI and patient photo from the American Academy of Pediatrics

brain, and other organs. It can target children who are two to fifteen years of age, and this syndrome has not been reported to affect babies. Symptoms of inflammation on such body parts include redness, swelling, heat, and pain. Children who undergo this rare condition have been exposed to COVID-19, as shown by antibody tests with positive results. These positive results demonstrate that the child's immune system[8] developed antibodies, blood proteins that counteract antigens, which were created in response to the COVID-19 virus. However, a child diagnosed with MIS-C does not always develop the symptoms of COVID-19; the exposure of the COVID-19 virus can result in patients being asymptomatic, in which they never develop symptoms at all. On the other hand, there have been cases in which children developed the symptoms for the COVID-19 virus[9] and have developed MIS-C.

## VII. Signs and Symptoms

The signs and symptoms of MIS-C include vomiting, skin rash, red eyes, redness or swelling in the hands or feet, fever, difficulty breathing, and severe stomach pain. After a child is exposed to COVID-19, the syndrome can develop within four weeks. If a child developed symptoms such as these, it is imperative to take immediate action and seek treatment.[10]

MIS-C has similar symptoms to Kawasaki Disease (KD), a disease in which it involves the inflammation of blood

vessels that causes artery aneurysms. KD specifically affects children who are younger than five years old, and the exact cause of it has not been determined yet. It may be linked to certain environmental exposure and genes, but scientists are continuing research on this syndrome. It is still unknown whether MIS-C and Kawasaki Disease are linked in any way, but further research is allowing scientists to develop new treatments for MIS-C due to the similar symptoms.[11]

## VIII. Treatment and Prevention

The treatment of MIS-C includes going to a pediatric hospital in which health professionals check for areas of inflammation in bodily organs by doing tests of the chest, heart, and abdomen. Anti- inflammatory drugs are used in order to help mitigate internal inflammation in vital organs and to reduce multi-organ failure. Although MIS-C is not contagious, children infected with COVID-19 may still transmit[12] SARS-CoV-2 to other susceptible individuals which could potentially lead to the development of MIS-C. As a result, it is important to enact proper guidelines to prevent the spread of COVID-19 so less cases of MIS-C may arise.

Certain prevention measures for MIS-C that have been outlined goes in tandem with COVID-19 prevention measures. Washing hands frequently, practicing social distancing, wearing masks, and avoiding people who are sick allows for the spread to slow down and for the disease to not infect as many individuals. Since COVID-19 and MIS-C are still new topics of discussion for researchers, there are many intricacies that are still unknown. However, by taking precautionary measures in order to avoid any harm, it creates foreseeable benefits.

## IX. Conclusion

In efforts to overcome this immensely riddling virus that overtakes the immune system, researchers and scientists have been working on developing any form of treatment or vaccine that they can. When such a virus is equipped with capabilities to mutate and can destroy existing antibodies or leading to Acute Respiratory Distress Syndrome (ARDS) in patients and MIS-C in young children, a vaccine is in dire need. Research and development is currently in progress in order to help with the treatment of COVID-19. Recently, a new drug by the name of Remdesivir has entered the market with a high price for hospitals. This drug, however, appears to work efficiently against SARS-CoV-2 by blocking the coronavirus's RNA polymerase using a nucleoside analogue of adenosine which is one of the main enzymes that SARS-CoV-2 needs to replicate its genetic material[13]. Dexamethasone which is a common corticosteroid medication that has been used for many years to treat various health conditions including autoimmune conditions. Hydroxychloroquine and chloroquine are two drugs that usually treat malaria, rheumatoid arthritis, and lupus, and Azithromycin which is an antibiotic commonly used to treat bacterial infections such as bronchitis and pneumonia and has been shown to have some in vitro activity against influenza A and Zika, but not Middle East Respiratory Syndrome, also known as MERS (another coronavirus). More treatments are in the works with immunology, with possibilities to use stem cell derived heart cells to treat the infection of heart cells, to support the immune system's battle against SARS-CoV-2


## Acknowledgments

We thank Dr. Oscar Juarez, Mr. Paul Nguyen, and Dr. Karina Tuz from the Illinois Institute of Technology for their support and guidance throughout this process


## Works Cited


1. Shereen, Muhammad Adnan et al. "COVID-19 infection: Origin, transmission, and characteristics of human coronaviruses." *Journal of advanced research* vol. 24 91-98. 16 Mar. 2020, doi:10.1016/j.jare.2020.03.005
2. Symptoms of Coronavirus. (n.d.). Retrieved August 30, 2020, from https://www.cdc.gov/coronavirus/2019-ncov/symptoms-testing/symptoms.html
3. CDC COVID Data Tracker. (n.d.). Retrieved August 30, 2020, from https://covid.cdc.gov/covid-data-tracker/?CDC_AA_refVal=https://www.cdc.gov/coronavirus/2019-ncov/cases-updates/cases-in-us.html
4. "The Innate and Adaptive Immune Systems." *InformedHealth.org [Internet].*, U.S. National Library of Medicine, 30 July 2020, www.ncbi.nlm.nih.gov/books/NBK279396/.
5. Perlman, Stanley. "COVID-19 Poses a Riddle for the Immune System." *Nature News*, Nature Publishing Group, 17 Aug. 2020, www.nature.com/articles/d41586-020-02379-1.
6. Ragab, D. et al. (2020, June 04). TheCOVID Cytokine Storm; What We Know So Far. Retrieved August 31, 2020, from

https://www.frontiersin.org/articles/10.3389/fimmu.2020.01446/full
7. Coperchini, F. et al. (2020, May 11). The cytokine storm in COVID-19: An overview of the involvement of the chemokine/chemokine-receptor system. Retrieved August 30, 2020, from https://www.sciencedirect.com/science/article/pii/S1359610120300927
8. "COVID-19 Linked to Inflammatory Syndrome in Children." *Mayo Clinic*, Mayo Foundation for Medical Education and Research, 12 June 2020, www.mayoclinic.org/diseases-conditions/coronavirus/in- depth/mis-c-in-children-covid-19/art-20486809.
9. Feldstein, Leora R., et al. "Multisystem Inflammatory Syndrome in U.S. Children and Adolescents: NEJM." *New England Journal of Medicine*, 23 July 2020, www.nejm.org/doi/full/10.1056/NEJMoa2021680.
10. Hameed, Shema, et al. "Spectrum of Imaging Findings on Chest Radiographs, US, CT, and MRI Images in Multisystem Inflammatory Syndrome in Children (MIS-C) Associated with COVID-19." *Radiology*, 25 June 2020, pubs.rsna.org/doi/full/10.1148/radiol.2020202543.
11. Ng, Khuen Foong, et al. "COVID-19 Multisystem Inflammatory Syndrome in Three Teenagers with Confirmed SARS-CoV-2 Infection." *Wiley Online Library*, John Wiley & Sons, Ltd, 6 July 2020, onlinelibrary.wiley.com/doi/full/10.1002/jmv.2620
12. Rowley, Anne H. "Understanding SARS-CoV-2-Related Multisystem Inflammatory Syndrome in Children."*Nature News*, Nature Publishing Group, 16 June 2020, www.nature.com/articles/s41577-020-0367-5.
13. Katherine Seley-Radtke Professor of Chemistry and Biochemistry and President-Elect of the International Society for Antiviral Research. "Remdesivir Explained – What Makes This Drug Work against Viruses?" The Conversation, 6 Sept. 2020, theconversation.com/remdesivir-explained-what-makes-this-drug-work-against-viruses-137751.
14. Zhang, Jun-Ming, and Jianxiong An. "Cytokines, Inflammation, and Pain." International Anesthesiology Clinics, U.S. National Library of Medicine, 30 Nov. 2009, www.ncbi.nlm.nih.gov/pmc/articles/PMC2785020/.

# HOW TO JOIN

URJ-IIT welcomes new members and contributors year-round. We seek out students who are passionate about research and academic writing. There are various opportunities for involvement to contribute to editing, design, outreach, and publications.

Visit **http://urj.library.iit.edu/index.php/urj** for more information.

# HOW TO SUBMIT

All submissions must be original research papers and abstracts compiled while in attendance at the Illinois Institute of Technology. URJ-IIT accepts papers from all disciplines and fields, including but not limited to architecture, physical sciences, social sciences, natural sciences, applied sciences, and humanities.

Visit **http://urj.library.iit.edu/index.php/urj/information/authors** for more information.

@urj.iit

@urjofiit

rb.gy/tf4k3q

URJ IIT